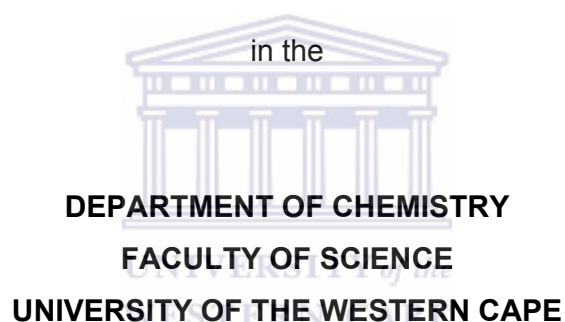


# **ONE-DIMENSIONAL NANOSTRUCTURED POLYMERIC MATERIALS FOR SOLAR CELL APPLICATIONS**

**SIPHO ENOS MAVUNDLA**

A thesis submitted in fulfillment  
of the requirements for the degree of

**Doctor of Philosophy**



**Supervisors:**

**Prof. Emmanuel I. Iwuoha,  
University of the Western Cape**

**And**

**Dr. Gerald F. Malgas,  
Council for Scientific and Industrial Research**

**DATE SUBMITTED: NOVEMBER 2010**

# ABSTRACT

---

This work entails the preparation of various polyanilines with different morphologies and their application in photovoltaic solar cells. Zinc oxide (ZnO) with one-dimensional and flower-like morphology was also prepared by microwave irradiation and used as electron acceptors in photovoltaics devices. The morphological, structural, spectroscopic and electrochemical characteristics of these materials were determined by scanning electron microscopy (SEM), X-Ray diffraction (XRD), Raman, Fourier-transformed infrared spectroscopy (FTIR), ultraviolet and visible spectroscopy (UV-Vis), photoluminescence(PL), thermal gravimetric analysis (TGA) and cyclic voltammetry (CV) experiments. Devices fabricated from these materials were characterized under simulated AM 1.5 at 800 mW. Most of the devices were bulk heterojunction with 1:1 (w/w) of donor/acceptor. Among various devices fabricated, a device from one-dimensional hexagonal structured poly(2, 5-dimethoxy aniline) was the best performer when used with one-dimensional ZnO as an acceptor. The good performance was attributed to the efficient electron transport due to high crystallinity and one-dimensional morphology of both ZnO and PDMA. This was confirmed by using ZnO with flower-like morphology as an acceptor and poly(2,5 dimethoxyaniline) (PDMA) with one-dimensional hexagonal structure as a donor, the efficiency of was about 100 000 less than when one-dimensional ZnO was used. Another device was also fabricated where one-dimensional PANI with worm-like morphology was used with ZnO. Again the one-dimensional ZnO device performed better with

efficiency of about 1000 times more than that of ZnO with flower-like morphology.



# DECLARATION

---

I declare that “**One-dimensional Nanostructured Polymeric Materials for Solar Cell Applications**” is my own work, that it has not been submitted for any degree or examination in any other university and that all the resources I have used or quoted have been indicated and acknowledged by means of complete references.



Sipho E Mavundla

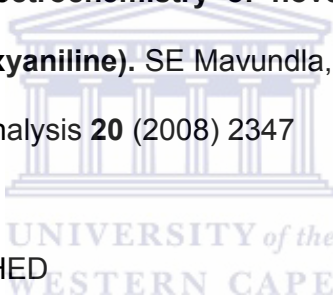
Signed:

# OUTPUTS FROM THIS THESIS

---

## PUBLISHED PAPERS

- **Physicochemical and morphological properties of poly (aniline-co-pyrrole).** SE Mavundla, GF Malgas, E Iwuoha and D Motaung  
Journal of Material Science **45** (2010) 3325–3330
- **Synthesis and electrochemistry of novel nanophase hexagonal poly (2,5-dimethoxyaniline).** SE Mavundla, GF Malgas, E Iwuoha and P Baker, *Electroanalysis* **20** (2008) 2347



## PAPERS TO BE PUBLISHED

- **Structural modulation of polyaniline and zinc oxide nanosystems for the application in solar cells.** SE Mavundla, GF Malgas, E Iwuoha and D Motaung.
- **Hybrid Solar Cells from Poly (2,5 dimethoxyaniline) Hexagonal Structures and Zinc Oxide.** SE Mavundla, GF Malgas, E Iwuoha and D Motaung.

# ACKNOWLEDGEMENTS

---

I would like to thank my supervisor at CSIR, Dr Gerald Malgas for his commitment in our work and his wise advises, especially the thesis structure. I would also like to thank my supervisor at UWC, Prof. Emmanuel Iwuoha for making me to see the importance of studying further, I have been with him for almost eight years. I have learned a lot from you Prof, thank you. I would not forget Prof. Leslie Petrik for giving me the opportunity to work with her and subsequently get a CSIR bursary for my M.Sc. I would like to thank Thomas Malwela and Dr. Sreejarani Pillai, of the National Centre for Nano-structured Materials for helping with FIB-SEM and SEM analysis respectively. I am also grateful to Siyasanga Mpelane and Dr. Lucky Skhwivhili for their assistance with microwave irradiation. Dr. Mlungisi Nkosi at iThemba Labs and Wilbert Mtinga at University of Pretoria are also thanked for their assistance in aluminum deposition. I would like to thank my colleagues both at CSIR and at UWC sensor lab for their support and encouragement. I am also indebted to Council for Scientific and Industrial Research (CSIR) and Department of Science and Technology (DST) for their financial contribution. Last but not the least; I would like to thank my family and friends for support and encouragement. I would also like to thank my ancestors; Mavundla, Mthiyane and Snakanaka for being there for me and for always giving directions. I would like to thank Almighty Shembe, for without him nothing is possible.

This work is dedicated to my late parents, **Mantombi maLanga Mavundla**  
(mother) and **Mpiyakhe ka Skeyi ka Mathahana Mavundla** (father)



# CONTENTS

ABSTRACT .....	II
DECLARATION .....	IV
OUTPUTS FROM THIS THESIS .....	V
ACKNOWLEDGEMENTS .....	VI
CHAPTER ONE .....	2
INTRODUCTION AND THESIS OUTLINE .....	2
1.1. Introduction .....	2
1.2. Thesis outlines and aims of the study .....	4
1.3. References: .....	6
CHAPTER TWO .....	9
THEORETICAL BACKGROUND .....	9
2.1. A brief History of Solar Cells .....	9
2.2. Inorganic Solar cell .....	10
2.3. Evolution of Organic Solar Cells .....	11
2.4. Conducting Polymers .....	12
2.4.1. Singlet Excitons .....	14
2.4.2. Polarons .....	15
2.4.3. Charge Transport and Morphology .....	15
2.4.4. Doping of Polymers .....	15
2.5. Synthesis of Conducting Polymers .....	17
2.5.1. Chemical Polymerization .....	18
2.5.2. Electrochemical Polymerization .....	19
2.6. Basic Operation Principle .....	20



2.6.1. Light Absorption and Exciton Generation .....	21
2.6.2. Charge Separation and Transport .....	23
2.6.3. Donor/Acceptor Interface .....	23
2.7. Device Architecture .....	25
2.7.1. Single Layer Devices .....	25
2.7.2. Bilayer Heterojunction Devices.....	25
2.7.3. Bulk Heterojunction Devices.....	26
2.7.4. Diffuse Bilayer Heterojunction Devices .....	26
2.8. PANI as Electron Donor Material for OSC devices .....	27
2.9. Electron Acceptor Materials .....	30
2.9.1. Fullerenes .....	30
2.9.2. Inorganic nanoparticles.....	30
2.10. References:.....	32
CHAPTER THREE.....	38
EXPERIMENTAL METHODS AND ANALYTICAL TECHNIQUES .....	38
3.1. Experimental methods .....	38
3.1.1. Spin Coating .....	38
3.1.2. Device Fabrication .....	39
3.2. Measurement of Properties.....	40
3.2.1. Conductivity Measurements .....	40
3.2.2. Photovoltaic (I-V) Device Characterization.....	41
3.2.2.1 Short Circuit Current.....	42
3.2.2.2 Open Circuit Voltage .....	42
3.2.2.3 Fill Factor.....	42
3.2.2.4 Air Mass .....	43

3.2.2.5 Power Efficiency.....	43
3.3. Analytical Techniques .....	44
3.3.1. Scanning Electron Microscopy (SEM) .....	44
3.3.1.1. Instrumental Set-up of a SEM .....	45
3.3.1.2. Resolution .....	46
3.3.2. Raman Spectroscopy .....	48
3.3.2.1. Instrumental Set-up of a Raman spectrophotometer.....	51
3.3.3. X-RAY DIFFRACTION .....	52
3.3.3.1. Instrumental Set-up of an X-ray Diffractometer .....	54
3.3.4. Cyclic Voltammetry (CV).....	56
3.3.4.1. Instrumental Set-up of a Cyclic Voltammogram.....	59
3.3.5. Ultraviolet and Visible Spectroscopy (UV-Vis) .....	60
3.2.5.1. Instrumental Set-up of a UV-vis Spectrophotometer .....	62
3.3.6. Photoluminescence(PL).....	64
3.3.6.1. Instrumental Set-up of a PL Spectrometer .....	66
3.4. References:.....	67
CHAPTER FOUR.....	70
SYNTHESIS AND CHARACTERIZATION OF NOVEL NANOPHASE HEXAGONAL POLY(2,5-dimethoxyaniline) .....	70
4.1. Introduction .....	70
4.2. Experimental Details .....	72
4.2.1. Materials .....	72
4.2.2. Synthesis of Polyaniline (PANI) and Poly(2,5-dimethoxyaniline) (PDMA) .....	72
4.2.3. Characterization.....	73
4.3. Results and Discussion.....	74
4.3.1. MORPHOLOGY.....	74

4.3.1.1. Mechanism for the Formation of the Hexagonal Nanostructures.....	76
4.3.2. Fourier Transform Infrared spectroscopy (FT-IR) .....	79
4.3.3. Ultraviolet Visible. (UV-Vis) .....	82
4.3.4. Thermo-Gravimetric Analysis (TGA) .....	83
4.3.5. Cyclic Voltammetry .....	85
4.4. Conclusion .....	89
4.5. References:.....	90
CHAPTER FIVE.....	94
PHYSICOCHEMICAL AND MORPHOLOGICAL PROPERTIES OF POLY (aniline-co-pyrrole).....	94
5.1. Introduction .....	94
5.2. Experimental Details .....	96
5.2.1. Materials .....	96
5.2.2. Synthesis of PANI, PPy, Poly (aniline-co-pyrrole), PDMA, and poly (2,5 dimethoxyaniline-co-pyrrole).....	96
5.2.3. CHARACTERIZATION .....	97
5.3. Results and Discussion .....	98
5.3.1. Ultraviolet Visible Spectral Analysis .....	98
5.3.2. Photoluminescence Analysis.....	100
5.3.3. X-Ray Diffraction Analysis .....	101
5.3.4. Scanning Electron Microscopy Analysis.....	103
5.3.5. Fourier Transform Infrared Spectroscopy (FT-IR).....	104
5.3.6. I-V Measurements .....	106
5.4. Conclusion .....	109

5.5. References:	110
CHAPTER SIX	117
Structural Modulation of Polyaniline and Zinc Oxide Nanosystems for Application in Solar Cell Devices	117
6.1. Introduction	117
6.2. Experimental	119
6.2.1. Materials	119
6.2.2. ZnO Synthesis	119
6.2.3. Synthesis of PANI and In-situ Synthesis of PANI- ZnO Composites	120
6.2.4 Fabrication of Devices	120
6.2.5. Characterization	121
6.3. Results	122
6.3.1. Scanning Electron Microscopy and Transmittance Electron Microscopy	122
6.3.2 UV-Vis	125
6.3.3. Raman Spectroscopy	126
6.3.4 X-Ray Diffraction	127
6.3.5 Solar Cell Performance and Conductivity	128
6.4. Conclusion	132
6.5. References:	133
CHAPTER SEVEN	138
HYBRID SOLAR CELLS FROM Poly(2,5 dimethoxyaniline) HEXAGONAL STRUCTURES AND ZINC OXIDE	138
7.1. Introduction	138

7.2. Experimental .....	140
7.2.1. Materials .....	140
7.2.2. Synthesis of ZnO Nanostructures.....	140
7.2.3. Fabrication of Devices .....	140
7.2.4. Characterization.....	141
7.3. Results and Discussion.....	142
7.3.1. Scanning Electron Microscopy .....	142
7.3.2. X-ray Diffraction .....	144
7.3.3. Photoluminescence .....	145
7.3.4. Solar Cell Characterization .....	147
7.4. Conclusion .....	151
7.5. References:.....	152
CHAPTER EIGHT .....	156
8.1. Overall Conclusions.....	156



# CHAPTER ONE

---

## INTRODUCTION AND THESIS OUTLINE

### 1.1. INTRODUCTION

Most of the global energy demand is currently produced from fossil fuels. These fossil fuels are not only limited, but also contribute towards environmental pollution and global warming. These energy shortages force us to look at renewable energy as an alternative energy source. Examples of renewable energies are wind power, hydroelectric generation, geothermal sources and solar power. Among renewable energies solar power is the most promising because it utilises the nearly inexhaustible energy that we obtain from the sun. Our planet receives  $\sim 1.2 \times 10^{17}$  W of solar power, while the rate of current worldwide energy consumption is  $\sim 10,000$  times smaller at  $\sim 1.3 \times 10^{13}$  W. The irradiation energy of the sun can be used to produce an electrical current using the photovoltaic (PV) effect by means of PV devices (solar cells). However, at present the cost of producing electricity by PV devices is high compared to that of electricity produced from fossil fuels. It is forecasted that PV devices will account for about 18% of the global energy production by the year 2060 [1]. For this to be realized, an inexpensive and repeatable process is required for the production of efficient and stable PV devices.

Organic photovoltaics (OPV) have a great technological potential as an alternative source for electrical energy. These organic materials are usually soluble in common organic solvents, making device production relatively easy. Thin films can be screen and “ink-jet” printed [2] spin-coated [3] or doctor bladed [4] from solution. Organic materials can be processed at low temperatures thereby reducing manufacturing costs, and they can also be fabricated into thin films onto plastic substrates. However, they currently lag behind their inorganic counterparts because of low energy conversion efficiencies, of approximately 1-6% [5, 6]. Although organic solar cells are not as efficient as their inorganic counterparts, there are other characteristics that make them attractive such as their flexibility, lightweight, low cost that allows for easy, large-scale processing from solution that may not require vacuum deposition or high temperatures [7].

There are several factors that influence the efficiency of (OPV), e.g., the structure of the polymer, the morphology of the film, the interfaces between the layers (organic/metal, organic/organic), the choice of electron acceptor and the ratio between this and the polymer, and the solvents used during preparation [8, 9]. Electron donor materials efficiently used are phthalocyanines, polythiophenes, and poly-phenylenevinylenes (PPV). Representative electron acceptors are perylenes, nanorods, fullerenes, and nanotubes [10-13].

A major disadvantage of OPV is the low power conversion efficiency compared with established inorganic-based PV devices. However, these two very different technologies are complementary in many ways. One of the

major reasons why OPVs have not realized its full potential is due to the lack of understanding of the structure-property relationship of the polymer/acceptor material. Other important factors that will put OPVs one step closer to commercialization, includes its processing onto large area modules and long-term stability of devices [14-17].

## 1.2. THESIS OUTLINES AND AIMS OF THE STUDY

In the last decade, solution processable organic conducting and semiconducting polymers have been extensively studied for use in organic solar cells due to their low-cost synthesis, low thermal budget and direct-writing printing techniques. However, various properties of conducting polymers such as the charge mobility and electrical conductivity need to be improved in order to achieve the performance level of solar cells based on its inorganic crystalline and amorphous counterparts.

The aim of this study is to synthesize highly crystalline one-dimensional structures and low band-gap polymers (Polyaniline, Poly (2,5 dimethoxyaniline), and Polypyrrole) for solar cell applications to enhance the efficiency of organic solar cells. Zinc oxide with flower and pencil-like morphologies will be synthesized and used as electron acceptor material in the fabrication of a photovoltaic device due to its tunable morphology.

The structure of the thesis will be as follows:

In chapter one a brief introduction on the energy scenario is given. *Chapter two* will give a brief background of solar cells and conducting polymers. It will also introduce the reader to the basic operation principles and



the characterization and some important components of solar cell are also discussed.

*Chapter three* will present details of the experimental setups and a brief description of analytical techniques used in this study.

In *Chapter four* the synthesis and characterization of PDMA and PANI hexagonal nanophase structures and a possible growth mechanism will be discussed.

*Chapter five* will report on the morphological evolution, optical and structural properties of polyaniline-polypyrrole copolymers prepared by a chemical oxidative copolymerization process.

In *Chapter six* polyaniline with worm-like morphology will be used as electron donor and ZnO with flower-like morphology are used as electron acceptors. The devices with different architectures are fabricated and tested for efficiency.

*Chapter seven* will look at the synthesis of ZnO nanostructures with pencil-like morphology and use them as electron acceptors. Also look at the performance of PDMA-PPY copolymers (synthesized in chapter 5), PANI and PDMA hexagonal structures synthesized in Chapter 4 in solar cells.

In *Chapter eight* the overall conclusion will be discussed.

### 1.3. REFERENCES:

- [1]. Shell, in "The Evolution of the World's Energy Systems", London (1996)
- [2]. Shaheen, S.; Radspinner, R.; Peyghambarian, N.; Jabbour, G.,  
Fabrication of bulk heterojunction plastic solar cells by screen printing.  
*Applied Physics Letters* **2001**, 79, (18), 2996-2998.
- [3]. Chen, L. C.; Godovsky, D.; Inganäs, O.; Hummelen, J. C.; Janssens,  
R. A. J.; Svensson, M.; Andersson, M. R., Polymer Photovoltaic  
Devices from Stratified Multilayers of Donor–Acceptor Blends.  
*Advanced Materials* **2000**, 12, (18), 1367-1370.
- [4]. Brabec, C. J.; Cravino, A.; Meissner, D.; Sariciftci, N. S.; Rispiens, M.  
T.; Sanchez, L.; Hummelen, J. C.; Fromherz, T., The influence of  
materials work function on the open circuit voltage of plastic solar cells.  
*Thin Solid Films* **2002**, 403-404, 368-372.
- [5]. Olson, D. C.; Pirus, J.; Collins, R. T.; Shaheen, S. E.; Ginley, D. S.,  
Hybrid photovoltaic devices of polymer and ZnO nanofiber composites.  
*Thin Solid Films* **2006**, 496, (1), 26-29.
- [6]. Kim, J. Y.; Lee, K.; Coates, N. E.; Moses, D.; Nguyen, T.-Q.; Dante, M.;  
Heeger, A. J., Efficient Tandem Polymer Solar Cells Fabricated by All-  
Solution Processing. *Science* **2007**, 317, (5835), 222-225.
- [7]. Brabec, C. J.; Sariciftci, N. S.; Hummelen, J. C., Plastic Solar Cells.  
*Advanced Functional Materials* **2001**, 11, (1), 15-26.
- [8]. Ishii, H.; Sugiyama, K.; Ito, E.; Seki, K., Energy Level Alignment and  
Interfacial Electronic Structures at Organic/Metal and Organic/Organic  
Interfaces. *Advanced Materials* **1999**, 11, (8), 605-625.

- [9]. Hoppe, H.; Sariciftci, N. S., Morphology of polymer/fullerene bulk heterojunction solar cells. *Journal of Materials Chemistry* **2006**, 16, (1), 45-61.
- [10]. Halls, J.J. M .; Pichler, K.; Friend, R.H.; Moratti, S.C.; Holmes, A. B., Exciton diffusion and dissociation in a poly(p-phenylenevinylene)/C60 heterojunction photovoltaic cell. *Applied Physics Letters* 1996, 68, (22), 3120-3122.
- [11]. Huynh, W. U.; Dittmer, J. J.; Alivisatos, A. P., Hybrid Nanorod-Polymer Solar Cells. *Science* **2002**, 295, (5564), 2425-2427.
- [12]. Wienk, M. M.; Kroon, J. M.; Verhees, W. J. H.; Knol, J.; Hummelen, J. C.; van Hal, P. A.; Janssen, R. A. J., Efficient Methano[70]fullerene/MDMO-PPV Bulk Heterojunction Photovoltaic Cells. *Angewandte Chemie International Edition* **2003**, 42, (29), 3371-3375.
- [13]. Kymakis, E.; Amaratunga, G.A.J., Single-wall carbon nanotube/conjugated polymer photovoltaic devices. *Applied Physics Letters* **2002**, 80, (1), 112-114.
- [14]. Krebs, F. C.; Alstrup, J.; Spanggaard, H.; Larsen, K.; Kold, E., Production of large-area polymer solar cells by industrial silk screen printing, lifetime considerations and lamination with polyethyleneterephthalate. *Solar Energy Materials and Solar Cells* **2004**, 83, (2-3), 293-300.
- [15]. Krebs, F. C.; Spanggaard, H.; Kjær, T.; Biancardo, M.; Alstrup, J., Large area plastic solar cell modules. *Materials Science and Engineering: B* **2007**, 138, (2), 106-111.

- [16]. Dennler, G.; Lungenschmied, C.; Neugebauer, H.; Sariciftci, N.S.; Labouret, A., Flexible, conjugated polymer-fullerene-based bulk-heterojunction solar cells: Basics, encapsulation, and integration. *Journal of Material Research* **2005**, 20, (12), 3224.
- [17]. Lungenschmied, C.; Dennler, G.; Neugebauer, H.; Sariciftci, S. N.; Glatthaar, M.; Meyer, T.; Meyer, A., Flexible, long-lived, large-area, organic solar cells. *Solar Energy Materials and Solar Cells* **2007**, 91, (5), 379-384.



# CHAPTER TWO

---

## THEORETICAL BACKGROUND

### 2.1. A BRIEF HISTORY OF SOLAR CELLS

The basic physical phenomenon through which a solar cell converts sunlight directly into electricity is called photovoltaic effect, which was discovered by Edmund Becquerel in 1839 [1]. Willoughby Smith [2] also discovered the photovoltaic effect in selenium in 1873 and three years later William G. Adams found that illuminating a junction between selenium and platinum also has a photovoltaic effect [2, 3]. These two discoveries were a foundation for the first selenium solar cell construction, which was built in 1877 and later described in details by Charles Fritts in 1883 [4].

The first inorganic solar cell was developed in Bell's Laboratories in 1954 with 4.5% efficiency, which was increase to 6% within a few months [5]. Since then, more studies were conducted to improve the solar cell performance. By 1960 the efficiency was at 14% which resulted in the commercialization of solar cells [3]. The research on solar cells was further facilitated by the oil crisis in 1970 which forced scientist to improve the performance of solar cells because of the uncertainty in oil [6]. The research was focused on developing device physics and process technology. Methods to reduce the production costs of thin film technologies using amorphous

silicon or microcrystalline silicon were also actively investigated. Over these years the silicon solar cells have reached 24% in the laboratory. Today silicon based solar cells account for about 99% of all photovoltaic cells [5]. At the moment, solar cells comprising an inorganic semiconductor such as mono- and multi-crystalline silicon have found markets for small scale devices such as solar panels on roofs, pocket calculators and water pumps, etc.[7].

## **2.2. INORGANIC SOLAR CELL**

The inorganic solar cells consist of a junction of p-type and n-type semiconductors sandwiched between metal electrodes for charge collection. The p side contains an excess of the positive charges (holes), and the n side contains an excess of the negative charges (electrons). In the region near the junction an electric field is formed and the electrons and holes, which are generated through light absorption in the bulk of silicon (Si), diffuse to this junction, where they are directed by the electric field towards the proper electrode. These semiconductors have band gaps primarily corresponding to near infrared radiation. The inorganic semiconductor materials used to make photovoltaic cells include crystalline, multicrystalline, amorphous, and microcrystalline Si, the III-IV compounds and alloys, CdTe, and the chalcopyrite compound, copper indium gallium diselenide (CIGS). The highest efficiency reported in Si so far in the laboratory is 24.7% [8].

### 2.3. EVOLUTION OF ORGANIC SOLAR CELLS

One of the early ideas to use organic materials for photovoltaics came from observation of nature where plants convert light into energy using chlorophyll through the process of photosynthesis. The observation of photoconductivity in solid anthracene in 1906 marked the start of the organic solar cell field. In the early 1960s it was discovered that many common dyes, such as methylene blue, had semi-conducting properties, later, these dyes were among the first organic materials to exhibit the photovoltaic (PV) effect [5]. Early organic solar cell devices consisted of either a liquid active layer of chlorophyll solutions or microcrystalline films of chlorophyll sandwiched between metal electrodes with offset work functions. The devices from these materials yielded very low efficiencies because of their poor conductivities [9]. The discovery of conducting polymers by MacDiarmid [10], in 1977 sparked more investigation into the electronic properties of these polymers with an emphasis on their conductive processes. It was discovered that, in some cases, their (polymers) electrical conductivity could be varied over eleven orders of magnitude by varying dopant concentrations. In the 1980s the first polymers (including poly(sulphurnitride) and polyacetylene) were investigated in PV cells [5]. Despite the more improvement in conducting polymers the efficiencies were still low below 0.1%. The major breakthrough came in 1986 when Tang [11] introduced the two layered organic solar cells, which increased the efficiency to 1%. Since then, organic solar cells have undergone a gradual evolution that has led to energy conversion efficiencies of more than 5%. Two main approaches have been explored in the effort to develop viable devices, e.g. the donor–acceptor bilayer commonly achieved by vacuum

deposition of molecular components, and the so-called bulk heterojunction discovered by Yu in 1995 [12], which is represented in the ideal case as a bi-continuous composite of donor and acceptor phases, thereby maximizing the all-important interfacial area between the donors and acceptors. A lot of the work being done today involves the use of a combination of donor and acceptor organic as well as inorganic materials in cells with different morphologies. The cells that use both organic and inorganic materials are called hybrid solar cells.

## **2.4. CONDUCTING POLYMERS**

Polymers or plastics have been known to be insulators until the last three decades when it was discovered that certain class of polymers called conjugated polymers, which contain many double bonds in their structure, are actually semi-conductors with unusual electrical properties [13]. This was discovered by three professors, MacDiarmid, Shirakawa and Heeger who later received the noble prize in 2000 [14]. In the 1970s a student of a Japanese professor Shirakawa, made a mistake by putting too much catalyst in the polymerisation of acetylene. This resulted in the formation of a silvery film instead of a black powder. They tried to modify the polyacetylene by oxidation with iodine vapour, which changed the optical properties of the material. It was found that the conductivity had increased by ten million times [14]. Since then the conductive polymers have been studied immensely for many industrial application such as lightweight batteries, electrochemical sensors, gas separating membranes, capacitors, electrochromic displays, solar cells, ion exchangers, conductive adhesive and composites, light emitting diodes and



corrosion inhibitors. The most common types of conjugated polymers are shown in Figure 2.1.

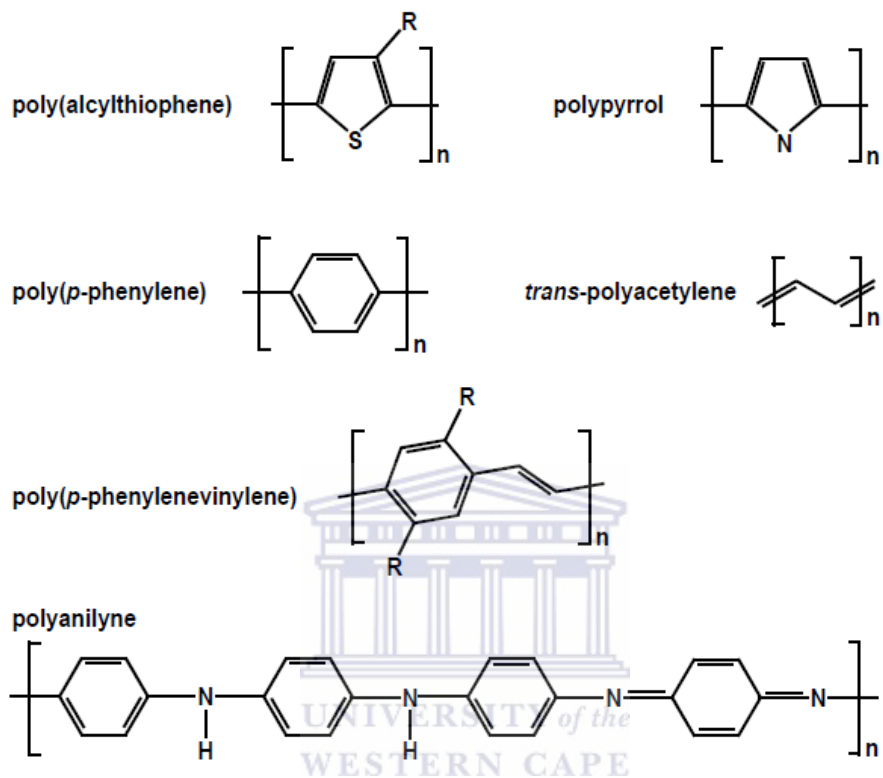


**Figure 2.1:** Example of some conjugated polymers.

The primary tasks of the conjugated polymer in organic solar cell are to absorb the light and to transport the positive charges to the ITO electrode [16]. Polyacetylene (shown in Figure 2.1) is the simplest conjugated polymer. Conjugated polymers are based on an alternation between single and double carbon-carbon bonds based on  $sp^2$ -hybridized carbon atoms and p-electrons. These p-electrons form a delocalized pi-system, which gives rise to the polymer's semi-conducting properties. Single bonds are known as  $\sigma$ -bonds and are associated with localized electrons, and double bonds contain a  $\sigma$ -bond and a  $\pi$ -bond. One of the important properties of conjugation is that the

$\pi$  ( $\pi$ ) electrons are more mobile than sigma ( $\sigma$ ) electrons; they can jump from site to site between carbon atoms with a low potential energy barrier as compared to the ionization potential [17]. Conjugated polymers derive their semiconducting properties by having delocalized p-electron bonding along the polymer chain. The  $\pi$  (bonding) and  $\pi^*$  (anti-bonding) orbitals form delocalized valence and conduction wave functions, which support mobile charge carriers [16]. Materials having a delocalized pi-bonding and pi anti-bonding ( $\pi$ — $\pi^*$ ) electron system can absorb sunlight, create photo-generated charge carriers, and transport these charge carriers [18]. The delocalized  $\pi$  electrons fill up to whole band and, the filled  $\pi$  band is called the highest occupied molecular orbital (HOMO) and the empty  $\pi^*$  band is called the lowest unoccupied molecular orbital (LUMO).

#### 2.4.1. SINGLET EXCITONS

After photon absorption, it is likely that the created electron hole pair forms a singlet exciton. This means that the electron and hole remain on the same polymer chain and are bound to each other by their electrostatic attraction. The energy levels of the singlet excitons are located within the HOMO-LUMO gap. The excitons can migrate within the film to lower energy sites. This process is referred to as exciton energy migration. The typical lifetime of singlet excitons is in the hundreds of picoseconds after which they can recombine radiatively or nonradiatively. The diffusion length is typically of the order of 10 nm [17, 19].

### **2.4.2. POLARONS**

Upon adding a charge to a polymer chain, the chain will deform to lower the energy of the carrier. This charge and deformation together constitute a polaron, hereafter denoted as P<sup>+</sup> or P<sup>-</sup> depending on the sign of the charge. The energy levels of a polaron are within the HOMO-LUMO gap. Polarons can drift along the conjugated chain. Once they reach the end of a conjugated segment, a hopping process to another conjugated chain can occur. Thus, in an applied electric field, a combination of drifting and hopping of polarons leads to charge transport through the film.

### **2.4.3. CHARGE TRANSPORT AND MORPHOLOGY**

Polaron theory and disorder formalism are two commonly used theories to describe charge transport in conjugated polymers. According to disorder formalism, the charge carriers are transported by a stochastic hopping process through a Gaussian manifold of localized states with superimposed electrical and positional disorder [20]. The polaron theory, on the other hand, suggested that it is the Marcus outer sphere electron transfer which dominates the charge transport. The charge carrier is self-trapped by significant molecular distortions which accompany the localization of charge on the molecule and the polaron can only migrate with its molecular distortions [21].

### **2.4.4. DOPING OF POLYMERS**

For a polymer to be conductive it must behave like a metal. In a metal, the atoms are imbedded in a "sea" of free electrons, and these electrons can

move as a group under the influence of an applied electric field. For that to happen the electrons must be disturbed by removing or inserting the electrons, this process is called doping. Doping is reversible with little or no degradation of the polymer backbone. During this process the polymer, which is an insulator or semiconductor, is converted to metallic polymer, which is conductive. Whether the polymer is doped chemically or electrochemically, the doping can be divided into two: *p*-doping (oxidation) and *n*-doping (reduction) *p*-type of doping is the partial oxidation of the polymer  $\pi$  backbone [15]. This was discovered by treating the polyacetylene with iodine (the oxidizing agent). In the *p*-type doping the electron is removed from the polymer backbone as described above. *n*-type doping is the partial reduction of the polymer  $\pi$  backbone. It was also discovered when polyacetylene was treated with reducing agent (liquid sodium). Like in the oxidation, the electron is inserted in the  $\pi$  backbone and the polymer becomes negatively charged. The negative ion will move along the polymer backbone with the help of solitons. A hole behaves as if it was an electron with a positive charge. Figure 2.2 show a schematic diagram of the movement of charges along the polymer backbone.

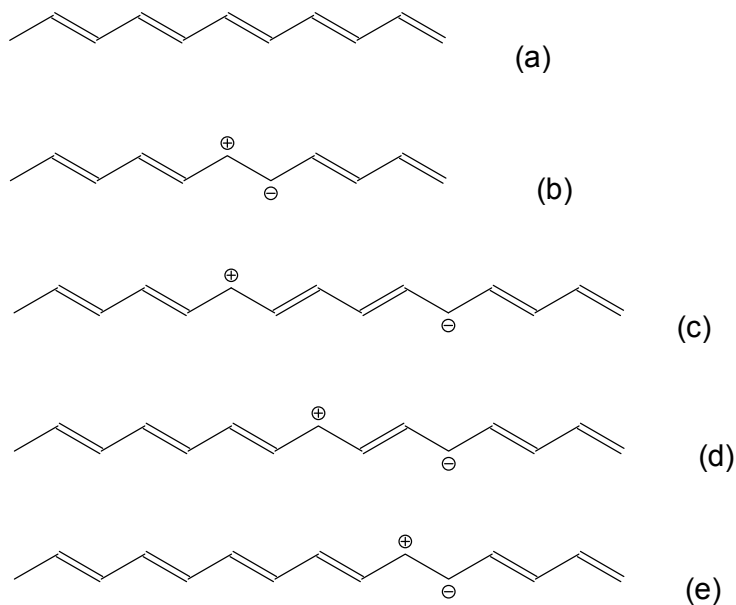


**Figure 2.2:** Schematic representation of movement of charge along the polymer backbone

## 2.5. SYNTHESIS OF CONDUCTING POLYMERS

Conductive polymers can be synthesized by any of the following techniques, e.g. electrochemical polymerization, chemical polymerization, photochemical polymerization, metathesis polymerization, concentrated emulsion polymerization, inclusion polymerization, solid-state polymerization, plasma polymerization, pyrolysis, soluble precursor polymer preparation and microwave initiation [22]. However, the two most important methods for obtaining or synthesizing conjugated polymers are by electrochemical and chemical polymerization.

### 2.5.1. CHEMICAL POLYMERIZATION

Oxidative chemical polymerization is one of the cheapest and widely used methods among chemical polymerization techniques for the preparation of conducting polymers. It is accomplished by exposing the monomer to a two-electron stoichiometric amount of oxidizing agent, resulting in the formation of the polymer in its doped and conducting state. Isolation of the neutral polymer is achieved by exposing the material to a strong reducing agent such as ammonia or hydrazine as shown in Figure 2.3. The mechanism of oxidative chemical polymerizations is thought to be very similar to that of electrochemical polymerizations. Heterocyclic monomers, such as thiophene and its derivatives, are typically polymerized in the presence of anhydrous  $\text{FeCl}_3$  [23] although other Lewis acids can also be used [24]. A tremendous advantage of chemical oxidative polymerizations is that, unlike unsubstituted heterocycles that form insoluble powders, properly substituted heterocyclic and other aromatic monomers like polyanilines form highly soluble polymers. These polymers can be analyzed by traditional analytical techniques to determine their primary structure. The nature of the polymerization conditions also allows for easy scale-up and production of large quantities of polymer.

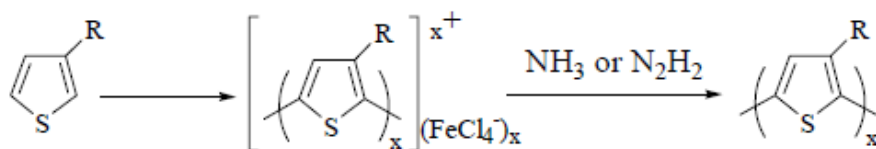


**Figure 2.3:** Lewis acid oxidative polymerization of an alkyl substituted thiophene.

## 2.5.2. ELECTROCHEMICAL POLYMERIZATION

Electropolymerization is a standard oxidative method for preparing electrically conducting conjugated polymers. The technique involves the oxidation of a monomer dissolved in a supporting electrolyte solution by applying an external potential to form reactive radical cations also known as the monomer oxidation potential as shown in (Figure 2.4). After the initial oxidation, two routes for polymer formation are possible. In the first pathway, a monomer radical cation can couple with a neutral monomer, and after a second oxidation and loss of two protons, forms a neutral dimer [25]. The second route involves the coupling of two radical cations followed by the loss of two protons to yield neutral dimer [26, 27]. Then the neutral dimer is oxidized and the process is repeated until an electroactive polymer film is deposited onto the conducting substrate. Because of the oxidative nature of electropolymerizations, the deposited polymer is typically in its oxidized state, thus necessitating the presence of a supporting electrolyte to compensate the positive charges along the polymer backbone.

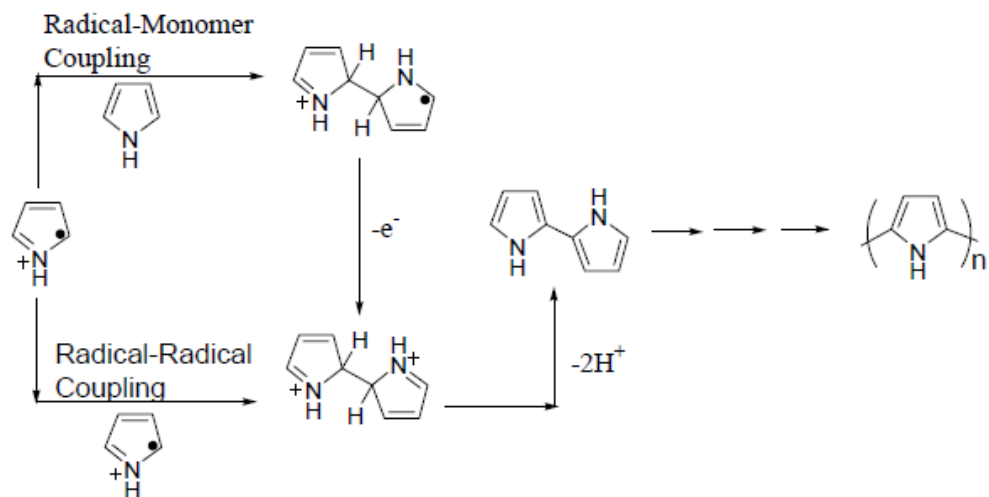


**Figure 2.4:** Proposed mechanism for the electrochemical polymerization of pyrrole.

## 2.6. BASIC OPERATION PRINCIPLE

The process of converting light into electric current in an organic photovoltaic cell is accomplished by four consecutive steps: (i) Photon/Light absorption: photons are absorbed by active organic materials leading to formation of an excitation state, the electron-hole pair, (exciton). (ii) Exciton diffusion: excitons move by diffusion process to a region where charge separation occurs. (iii) Exciton dissociation: separation of electron and hole pairs. This is possible at sharp potential at the donor-acceptor interface. (iv) Charge transport: the free charge carriers transport to the electrodes (holes to the anode and electrons to the cathode) with help of internal field [1, 28, 29]. This process is well illustrated in Figure 2.5.



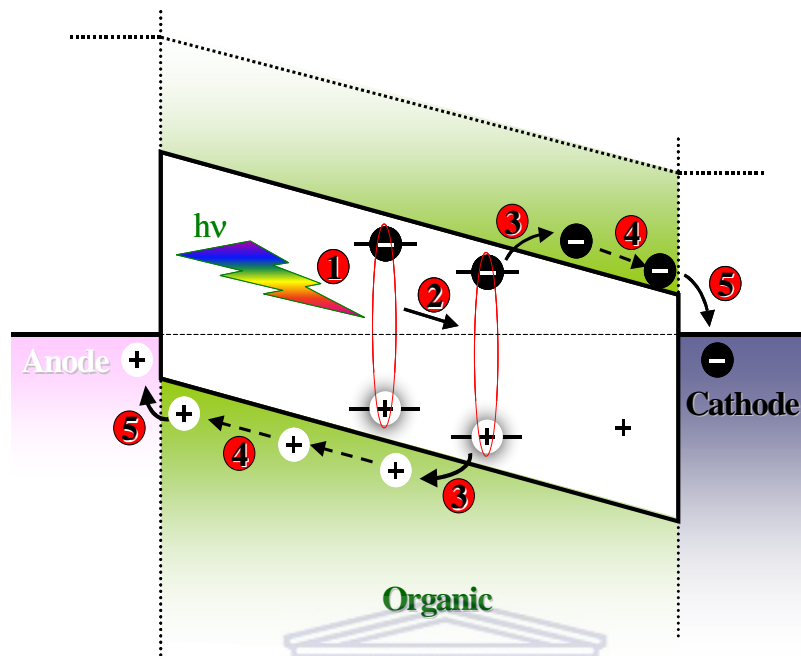


**Figure 2.5:** Schematic diagram of working principles of organic solar cells. (1) photon absorption, (2) exciton generation, (3) exciton dissociation, (4 and 5) charge transport.

### 2.6.1. LIGHT ABSORPTION AND EXCITON GENERATION

For an efficient collection of photons, the absorption spectrum of the “photo-active” organic layer should match the solar emission spectrum and the layer should be sufficiently thick to absorb all incident light. Due to the large band gap of organic materials, only a small portion of sunlight is absorbed by organic materials. A bandgap of 1.1 eV (1100 nm) is needed in order to absorb about 77% of sunlight whereas most organic materials have a bandgap  $> 2$  eV (600 nm), so this limits the absorption to less than 30% [1]. Figure 2.6 gives a clear indication on how wavelength is related to photon

harvesting. The sun irradiance (red) and number of photons (black) are plotted as a function of wavelength. The AM1.5 spectrum corresponds to the solar irradiance with the sun 45° above the horizon. The number of photons available for conversion into electrons can be represented by plotting photon flux as a function of wavelength since PVs convert 1 photon into one electron. It can be seen from Figure 2.6 that the optimum wavelength for photon harvesting is between 600 and 1000 nm.

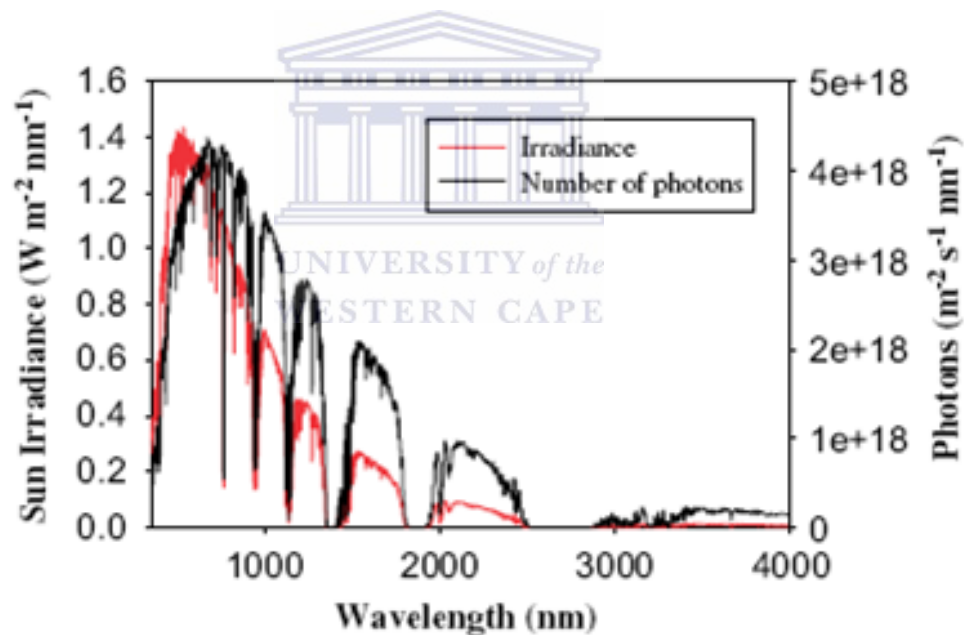


**Figure 2.6:** Sun irradiance (red) and number of photons (black) as a function of wavelength. The sun intensity spectrum is based on data from NREL808 [4].

Ideally, all “photo-excited” excitons should reach a dissociation site. Since such a site may be at the other end of the semiconductor, their diffusion length should be at least equal the required layer thickness (for sufficient absorption) otherwise they recombine and photons are wasted. Exciton diffusion ranges in polymers and pigments are typically around 10-20 nm [1, 28, 29].

### **2.6.2. CHARGE SEPARATION AND TRANSPORT**

“Photo-excitation” in organic solar cells does not lead directly to free charges, but to bound electron-hole pair (excitons). It is estimated that only about 10% of “photo-excitation” leads to free electrons. Charge separation usually occurs at an interface at electron donor (D)/electron acceptor (A). These materials (D and A) must have sufficient difference in electron affinity (EA) and ionization energy (IA) to have electrical field. The strong electrical field will break the excitons into electrons and holes. If the difference in IA and EA is not sufficient, the exciton may just hop onto the material with the lower band gap without splitting up its charges. Eventually it will recombine without contributing charges to the photocurrent [1, 29]. For efficient photovoltaic devices, the created charges need to be transported to the appropriate electrodes within their lifetime. The charge carriers need a driving force to reach the electrodes [1, 29].

### **2.6.3. DONOR/ACCEPTOR INTERFACE**

An essential process for polymeric solar cells after “photo-excitation” is charge separation. Since the electron and hole are bound together, a

mechanism must be found to efficiently separate electron and hole and to prevent recombination of the two. A possibility to achieve this charge separation is by introducing an electron acceptor that dissociates the exciton by transferring the electron from the polymer (therefore being the electron donor) to the electron acceptor material. Figure 2.8 shows a schematic diagram of the interface between two different semiconducting polymers that facilitate either charge transfer by splitting the exciton or energy transfer, where the whole exciton is transferred from the donor to the acceptor. In order for an electron transfer to be favourable, the electron affinity of the acceptor must be larger than the ionization potential of the donor and also that the electron transfer should happen quickly to compete with exciton decay mechanism which occur at a time scale of hundreds of picoseconds [30]. The charge separation occurs at the interface between donor and acceptor molecules, mediated by a large potential drop [31]. As a result, the polymer is left with a P<sup>+</sup> polaron that can drift through the film to the anode while the electron is in the acceptor material and can be transported to the cathode. After “photo-excitation” of an electron from the HOMO to the LUMO, the electron can jump from the LUMO of the donor (the material with the higher LUMO) to the LUMO of the acceptor if the potential difference between the ionisation potential of the donor and the electron affinity of the acceptor is larger than the exciton binding energy.

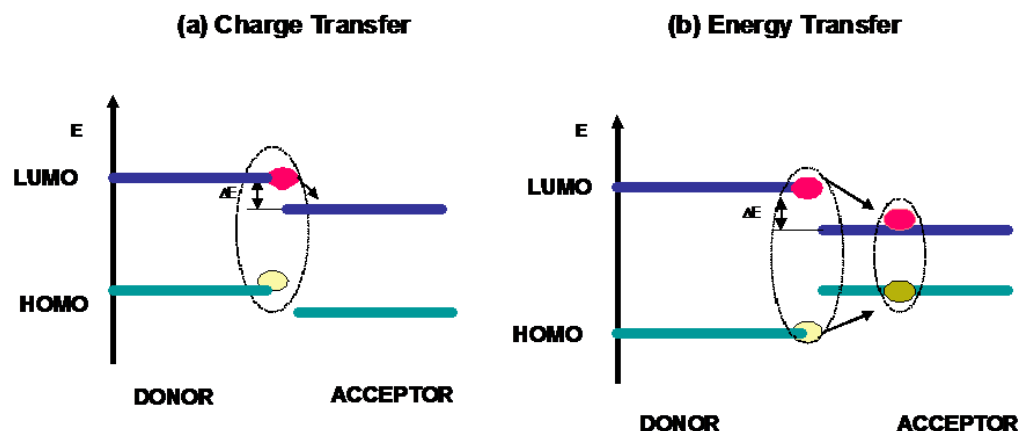


**Figure 2.7:** The interface between two different semiconducting polymers can facilitate either charge transfer by splitting the exciton or energy transfer, where the whole exciton is transferred from the donor to the acceptor

## 2.7. DEVICE ARCHITECTURE

### 2.7.1. SINGLE LAYER DEVICES

These are the first devices which were based on a layer of polymer sandwiched between two electrodes with different work function, low work metal (e.g. Al, Mg, Ca) and high work electrode (e.g. ITO, Au, Zn) [32]. It is the difference between these work functions that create the electric field which drives the charges to different electrodes. The “photo-active” region is much thinner since both charges travel through the same material [37]. This will result in high recombination because of the short exciton diffusion length in polymers leading to low efficiency.

### 2.7.2. BILAYER HETEROJUNCTION DEVICES

In a bilayer heterojunction donor (D) and acceptor (A) materials are stacked sequentially on top of each other and sandwiched between two

electrodes [18, 34]. Charge separation occurs at the interface between the two active materials, with the highest occupied molecular orbital (HOMO) and lowest unoccupied molecular orbital (LUMO) levels of the donor higher than those of the acceptor. After the excitons are dissociated the electron travels within the acceptor and the hole through the donor material [34]. Hence the recombinations are reduced.

### **2.7.3. BULK HETEROJUNCTION DEVICES**

Bulk heterojunction is where the D and A components are blended together in a bulk volume so that each donor–acceptor interface is within a distance less than the exciton diffusion length of each absorbing site [32]. The bulk heterojunction device is similar to the bilayer device with respect to the D-A concept, but it exhibits a largely increased interfacial area where charge separation occurs. The donor and acceptor phases have to form an interpenetrating and bicontinuous network in order for the separated charges to have a percolation path to the electrode. Although bulk heterojunction has a potential of high efficiency, they are more sensitive to nanoscale morphology in the blend [18, 32]. The highest efficiency reported so far for these devices is about 6.5%.

### **2.7.4. DIFFUSE BILAYER HETEROJUNCTION DEVICES**

This device structure is aiming to adapt the advantages of both bulk and bilayer concepts, an enlarged donor–acceptor interface and a spatially uninterrupted pathway for the opposite charge carriers to their corresponding electrodes. The diffuse interface is achieved in different ways: (i) If processed

from solution, two thin polymer films can be pressed together in a lamination procedure applying moderate pressure and elevated temperatures. (ii) Another way to achieve a diffuse interface is to spin coat the second layer from a solvent that partially dissolves the underlying polymer layer. (iii) Finally, also the controlled interdiffusion between an acceptor fullerene and a donor polymer by annealing of a bilayer [18, 32].

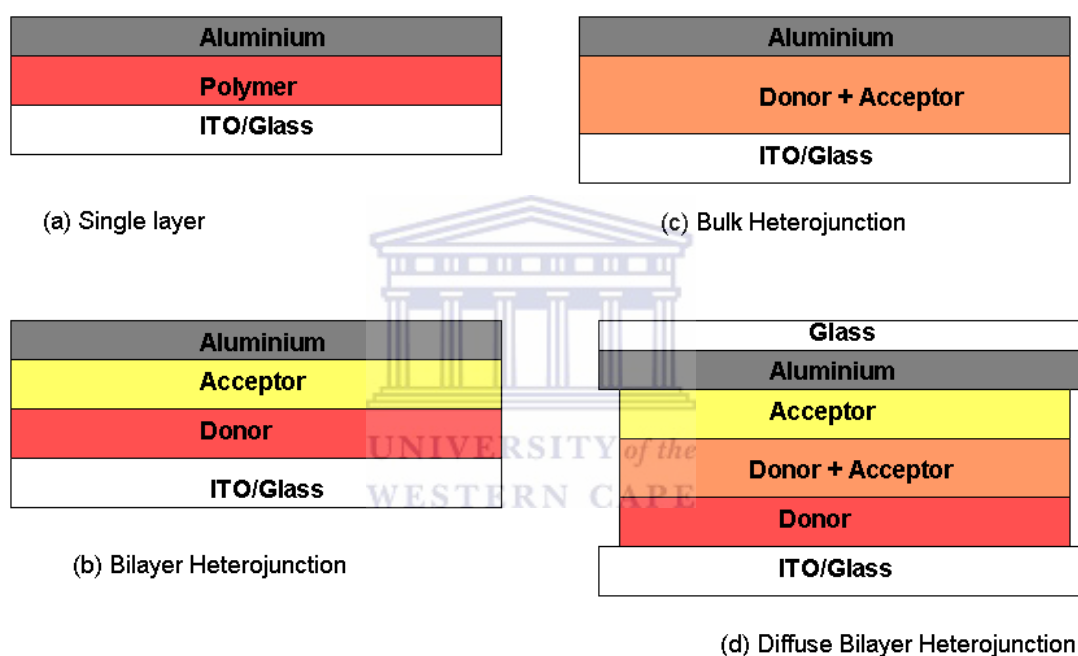


**Figure 2.8:** Different device architectures (a) Single layer, (b) Double layer, (c) Blended and (d) laminated device.

## 2.8. PANI AS ELECTRON DONOR MATERIAL FOR ORGANIC SOLAR CELL DEVICES

Among conducting polymers, polyaniline has attracted considerable attention due to its good chemical and environmental stability, high electrical conductivity, high redox reversibility, and ease of synthesis by chemical and

electrochemical techniques. It was first synthesized in 1862 [35] PANI is a typical phenylene-based polymer having –NH– group in a polymer chain linked either side with a phenylene ring. The protonation and deprotonation and various other physico-chemical properties of polyaniline are due to the presence of this -NH- group. PANI can be easily synthesized by chemically or electrochemically by oxidative polymerisation of aniline monomer in an acidic medium.

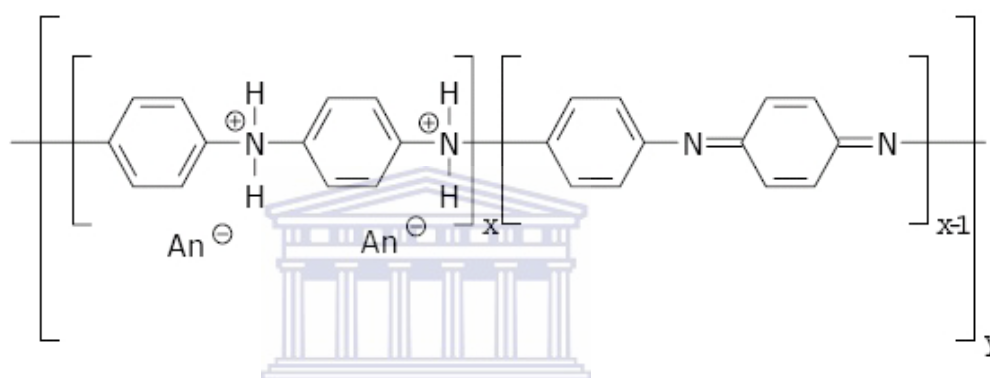


**Figure 2.9:** General structure of polyaniline. The completely reduced form (leucoemeraldine) can be obtained when  $(x-1) = 0$ . The completely oxidized form (pernigraniline) when  $(x-1) = 1$  and when  $(x-1) = 0.5$  it corresponds to emeraldine base.

The general structure of PANI with its three forms is shown in Figure 2.9. These forms are fully oxidized pernigraniline (PB), half-oxidized emeraldine base (EB), and fully reduced leucoemeraldine base (LB) [36]. Emeraldine is said to be the most stable form of PANI and it is the most conductive form when it is doped (emeraldine salt). PANI has many potential applications such as in nanowires, electronics, electrochromic devices, solar cells, and batteries [35-37], but all these applications are limited by the its



difficultly to process. Bulk PANI in itself is difficult to process; it does not dissolve in common solvent and it decomposes before melting. Many studies have been done in an effort to make PANI processable such as addition of side chain to the monomer aniline or doping with bulky dopants to make PANI soluble [38]. The problem with these bulky dopants was the solvent toxicity and difficult preparation. One way to overcome the problem of processability is to prepare its nanocomposites or nanotubes/rods. Polyaniline has been used in many cases for synthesis of nanocomposites and nanotubes/rods by using clay, transitional metals oxides such as titanium oxide ( $\text{TiO}_2$ ), vanadium oxide ( $\text{V}_2\text{O}_5$ ), zinc oxide and ( $\text{ZnO}$ ) [39, 40]. These nanocomposites can be prepared chemically or electrochemically. The potential of polyaniline transitional metals nanocomposites have introduced these materials into applications such as electronic devices, non-linear optical systems and photo electrochemical systems [41]. It is believed that the combination of n-type semiconductor of transitional metals and p-type of PANI is responsible for the improvement in the polyaniline photo current values due to the occurrence of excitons dissociation at the interface. PANI has been used as a hole injecting layer in Organic Light Emitting Diodes and it can also act as a barrier to oxygen and as a planarizing layer to inhibit electrical shorts and improve device lifetime, resulting in an improvement of the brightness and the efficiency of the Organic Light Emitting Diodes [42]. The incorporation of one-dimensional structure polyaniline as an interfacial layer in organic photovoltaics has been found to increase the power conventional efficiency by 26% [6].

## **2.9. ELECTRON ACCEPTOR MATERIALS**

As it was mentioned before, acceptor material is needed for the successful dissociation of excitons by transferring the electron from the polymer to the electron acceptor material. The acceptor material can be a conjugated polymers, fullerenes, inorganic nanocrystals or metal oxides.

### **2.9.1. FULLERENES**

Since the discovery of photo-induced charge transfer between conjugated polymers (as donors) and buckminsterfullerene  $C_{60}$  and its derivatives (as acceptor materials), several efficient photovoltaic systems based on the donor-acceptor principle using the combination of polymer and fullerenes have been fabricated [43]. It was found that  $C_{60}$  was not efficient as an acceptor due to its low solubility, branched  $C_{60}$  which are better in solubility were synthesized. For the acceptor materials in the polymer solar cells, [6,6]-phenyl-C-61-butyric acid methyl ester (PCBM) offers the advantages of good solubility in organic solvents (chloroform, chlorobenzene, dichlorobenzene, etc.), higher electron mobility, and higher electron affinity [44]. The highest efficiency to date is about 6.5% from PCBM and poly(3-hexylthiophene) (P3HT) devices.

### **2.9.2. INORGANIC NANOPARTICLES**

Although fullerenes provide the best performance, their price is still very high. One potential solution is the application of inorganic nanoparticles or nanostructures such as nanorods and nanowires as electron acceptors, to utilize the high electron mobility of the inorganic phase [45]. Various devices

have been fabricated using these metal oxides as acceptor materials. Up to so far 2.5% efficiency has been obtained where the donor was P3HT and acceptor being metal oxides.



## 2.10. REFERENCES:

- [1]. Bundgaard, E.; Krebs, F. C., Low band gap polymers for organic photovoltaics. *Solar Energy Materials and Solar Cells* **2007**, 91, (11), 954-985.
- [2]. Goetzberger, A.; Hebling, C.; Schock, H.-W., Photovoltaic materials, history, status and outlook. *Materials Science and Engineering: R: Reports* **2003**, 40, (1), 1-46.
- [3]. <http://www.mitsui.co.jp/en/business/challenge/solar/index.html>
- [4]. Ginger, D. S.; Greenham, N. C., Charge transport in semiconductor nanocrystals. *Synthetic Metals* **2001**, 124, (1), 117-120.
- [5]. Spanggaard, H.; Krebs, F. C., A brief history of the development of organic and polymeric photovoltaics. *Solar Energy Materials and Solar Cells* **2004**, 83, (2-3), 125-146.
- [6]. Bejbouji, H.; Vignau, L.; Miane, J. L.; Dang, M.-T.; Oualim, E. M.; Harmouchi, M.; Mouhsen, A., Polyaniline as a hole injection layer on organic photovoltaic cells. *Solar Energy Materials and Solar Cells* **2010**, 94, (2), 176-181.
- [7]. Reyes-Reyes, M.; Kim, K.; Dewald, J.; Lopez-Sandoval, R. N.; Avadhanula, A.; Curran, S.; Carroll, D. L., Meso-Structure Formation for Enhanced Organic Photovoltaic Cells. *Organic Letters* **2005**, 7, (26), 5749-5752.
- [8]. Miles, R. W.; Zoppi, G.; Forbes, I., Inorganic photovoltaic cells. *Materials Today* **2007**, 10, (11), 20-27.
- [9]. Gopal, A., **2007** Effects of Thickness, Morphology and Molecular Structure of Donor and Acceptor Layers in Thermally Interdiffused

Polymer Photovoltaics. *PhD Theses Virginia Polytechnic Institute and State University*.

- [10]. Xu, P.; Han, X. J.; Wang, C.; Zhang, B.; Wang, H. L., Morphology and physico-electrochemical properties of poly(aniline-co-pyrrole). *Synthetic Metals* **2009**, 159, (5-6), 430-434.
- [11]. Thompson, B. C.; Fréchet, J. M. J., Polymer–Fullerene Composite Solar Cells. *Angewandte Chemie International Edition* **2008**, 47, (1), 58-77.
- [12]. Yu, G.; Gao, J.; Hummelen, J. C.; Wudl, F.; Heeger, A. J., Polymer Photovoltaic Cells: Enhanced Efficiencies via a Network of Internal Donor-Acceptor Heterojunctions. *Science* **1995**, 270, (5243), 1789-1791.
- [13]. Raghavendra, S.; Khasim, S.; Revanasiddappa, M.; Ambika Prasad, M.; Kulkarni, A., Synthesis, characterization and low frequency a.c. conduction of polyaniline/fly ash composites. *Bulletin of Materials Science* **2003**, 26, (7), 733-739.
- [14]. Chiang, C. K.; Druy, M. A.; Gau, S. C.; Heeger, A. J.; Louis, E. J.; MacDiarmid, A. G.; Park, Y. W.; Shirakawa, H., Synthesis of highly conducting films of derivatives of polyacetylene, (CH)<sub>x</sub>. *Journal of the American Chemical Society* **1978**, 100, (3), 1013-1015.
- [15]. Mathebe, N. G. R.; Morrin, A.; Iwuoha, E. I., Electrochemistry and scanning electron microscopy of polyaniline/peroxidase-based biosensor. *Talanta* **2004**, 64, (1), 115-120.
- [16]. Brabec, C.J.; Dyakonov, V.; Parisi, J.; Sariciftci, N.S., **2003**. Organic Photovoltaics: Concepts and Realization. *Springer, Berlin*.

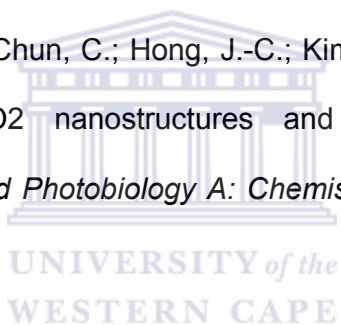
- [17]. Nunzi, J.-M., Organic photovoltaic materials and devices. *Comptes Rendus Physique* **2002**, 3, (4), 523-542.
- [18]. Gunes, S.; Neugebauer, H.; Sariciftci, N., Conjugated Polymer-Based Organic Solar Cells. *Chemical Reviews* **2007**, 107, (4), 1324-1338.
- [19]. Gupta, D.; Mukhopadhyay, S.; K. Narayan, S., Correlating reduced fill factor in polymer solar cells to contact effects. *Applied Physics Letters* **2008**, 92, (9) 93301-93303.
- [20]. Bäessler, H., Charge Transport in Disordered Organic Photoconductors a Monte Carlo Simulation Study. *physica status solidi (b)* **1993**, 175, (1), 15-56.
- [21]. Fishchuk, I. I.; Kadashchuk, A.; Bäessler, H.; Nešpůrek, S., Hopping polaron transport in disordered organic solids. *physica status solidi (c)* **2004**, 1, (1), 152-155.
- [22]. Kumar, D.; R. Sharma, C.; Advances in conductive polymers. *European Polymer Journal* **1998**, 34, 1053-1060.
- [23]. Sugimoto, R.-I.; Takeda, S.; H. Gu, B.; Yoshino, K., Preparation of soluble polythiophene derivatives utilizing transition metal halides as catalysts and their property. *Chemistry Express* **1986**, 1, (11), 635-638.
- [24]. Toshima, N.; Hara, S., Direct synthesis of conducting polymers from simple monomers. *Progress in Polymer Science* **1995**, 20, (1), 155-183.
- [25]. Asavapiriyant, S.; Chandler, G. K.; Gunawardena, G. A.; Pletcher, D., The electrodeposition of polypyrrole films from aqueous solutions. *Journal of Electroanalytical Chemistry* **1984**, 177, (1-2), 229-244.

- [26]. Genies, E. M.; Bidan, G.; Diaz, A. F., Spectroelectrochemical study of polypyrrole films. *Journal of Electroanalytical Chemistry* **1983**, 149, (1-2), 101-113.
- [27]. Pinzino, C.; Angelone, R.; Benvenuti, F.; Carlini, C.; Galletti, A. M. R.; Sbrana, G., Electron paramagnetic resonance studies on oxidative polymerization mechanism of furan derivatives. *Journal of Polymer Science Part B: Polymer Physics* **1998**, 36, (11), 1901-1910.
- [28]. Drees, M., **2003**. Polymer/Fullerene Photovoltaic Devices – Nanoscale Control of the Interface by Thermally-controlled Interdiffusion. *PhD Thesis, Virginia Polytechnic Institute and State University* .
- [29]. Zeng, T.W.; Lin, Y T; Chen, C.W.; Su, W.F., Charge separation and transport properties of photovoltaic devices based on MEHPPV/TiO<sub>2</sub> nanorods hybrid materials. *Proceedings of SPIE* **2006**, 6334, 6334R-1 - 63340R-6.
- [30]. Ginger, D.S.; Greenham, N.C., Charge transport in semiconductor nanocrystals. *Synthetic Metals* **2001**, 124, (1), 117-120.
- [31]. Kietzke, T., Recent Advances in Organic Solar Cells. *Advances in Opto Electronics* **2007**, Article ID 40285, 15 pages.
- [32]. Organic solar cells: An overview. *Journal Material Research* **2004**, 19, (7), 1924-1945.
- [33]. Bernede, J.C., Organic Photovoltaic Cells: History, Principles and Techniques. *Journal Chillian Chemical Society* **2008**, 53, (3) 1549-1564.
- [34]. Thompson, E.A., **2008**. Characterisation of Materials for Organic Photovoltaics. *PhD Thesis, University of St. Andrews*.

- [35]. Bekri-Abbes, I.; Srasra, E., Investigation of structure and conductivity properties of polyaniline synthesized by solid–solid reaction. *Journal of Polymer Research* **2010**, (1-7).
- [36]. Roy, B.; Gupta, M.; Bhowmik, L.; Ray, J., Synthesis and characterization of poly(2,5-dimethoxyaniline) and poly(aniline-Co-2,5-dimethoxyaniline): The processable conducting polymers. *Bulletin of Materials Science* **2001**, 24, (4), 389-396.
- [37]. Iwuoha, E.I.; Mavundla, S.E.; Somerset, V.S.; Petrik, L.F.; Klink, M.J.; Sekota, M.; Bakers, P., Electrochemical and Spectroscopic Properties of Fly Ash–Polyaniline Matrix Nanorod Composites. *Microchimica Acta* **2006**, 155, (3), 453-458.
- [38]. Cho, M.S.; Park, S.Y.; Hwang, J.Y.; Choi, H.J., Synthesis and electrical properties of polymer composites with polyaniline nanoparticles. *Materials Science and Engineering: C* **2004**, 24, (1-2), 15-18.
- [39]. Samoylov, A.V.; Mirsky, V.M.; Hao, Q.; Swart, C.; Shirshov, Y.M.; Wolfbeis, O.S., Nanometer-thick SPR sensor for gaseous HCl. *Sensors and Actuators B: Chemical* **2005**, 106, (1), 369-372.
- [40]. Khanna, P.K.; Lonkar, S.P.; Subbarao, V.V.V.S.; Jun, K.-W., Polyaniline-CdS nanocomposite from organometallic cadmium precursor. *Materials Chemistry and Physics* **2004**, 87, (1), 49-52.
- [41]. Schnitzler, D.C.; Meruvia, M.S.; Hummelgen, I.A.; Zarbin, A.J.G., Preparation and Characterization of Novel Hybrid Materials Formed from (Ti,Sn)O<sub>2</sub> Nanoparticles and Polyaniline. *Chemistry of Materials* **2003**, 15, (24), 4658-4665.



- [42]. Chang, M.-Y.; Wu, C.-S.; Chen, Y.-F.; Hsieh, B.-Z.; Huang, W.-Y.; Ho, K.-S.; Hsieh, T.-H.; Han, Y.-K., Polymer solar cells incorporating one-dimensional polyaniline nanotubes. *Organic Electronics* **2008**, 9, (6), 1136-1139.
- [43]. Kymakis, E.; Amaratunga, G.A.J., Carbon Nanotubes as Electron Acceptors in Polymeric Photovoltaics. *Review on Advanced Material Science* **2005**, 10, (4), 300-305.
- [44]. He, Y.; Chen, H.-Y.; Hou, J.; Li, Y., Indene-C<sub>60</sub> Bisadduct: A New Acceptor for High-Performance Polymer Solar Cells. *Journal of the American Chemical Society* **2010**, 132, (4), 1377-1382.
- [45]. Kim, S.-S.; Jo, J.; Chun, C.; Hong, J.-C.; Kim, D.-Y., Hybrid solar cells with ordered TiO<sub>2</sub> nanostructures and MEH-PPV. *Journal of Photochemistry and Photobiology A: Chemistry* **2007**, 188, (2-3), 364-370.



# CHAPTER THREE

---

## EXPERIMENTAL METHODS AND ANALYTICAL TECHNIQUES

### 3.1. EXPERIMENTAL METHODS

The experimental procedure for the synthesis of PANI, PDMA hexagonal nanostructures, poly (aniline-pyrrole), poly (2,5-dimethoxyaniline-pyrrole) copolymers, PANI with “worm-like” and ZnO “flower-like” structures in this study are discussed in chapters four, five, six and seven. These materials were characterized using different analytical techniques illustrated in the next section.

#### 3.1.1. SPIN COATING

Spin coating is a procedure used to apply uniform thin films to flat substrates. The solution is dropped and smeared onto the substrate which is then spun at speeds ranging from 1000 to 3000 rpm. As the solution is spun off the slide, the solvent evaporates, producing a uniform film. Thickness of spin-coated films may be varied in two ways. Different solution concentrations will produce films with different thicknesses; the greater the concentration, the thicker the film. Also, varying the spin speed will change the film thickness; the

lower the spin speed, the thicker the film. Poly(3,4-ethylenedioxythiophene) poly(styrenesulfonate) (PEDOT:PSS) was spin coated on the ITO substrate before the active layer was spin coated. This material will planarise the rough ITO, increase the work function and block electron acceptance.

### **3.1.2. DEVICE FABRICATION**

The ITO glass substrate was cleaned with methanol. PEDOT: PSS was spin coated on the cleaned ITO glass and dried on the hot plate at 100 °C for 20 min. The donor layer (PANI) was spin coated onto the PEDOT:PSS/ITO substrate and dried at 100 °C for 30 min. The acceptor layer was spin coated onto the PANI/PEDOT/ITO substrate and also dried at 100 °C for 1 h. On the other hand, about 200 nm of the aluminum film was deposited on the glass substrate. This Al/Glass was placed on top of Acceptor/Polymer/PEDOT:PSS/ITO layer and laminated together by pressing the substrates against each other and adding a small amount of adhesive to seal. The current density-voltage (I-V) measurements on the solar cell devices were performed using a Keithly Semiconductor Characterization System (SCS) by connecting the positive terminal to the anode (ITO) and a negative terminal to the cathode (aluminum). Figure 3.1 is a schematic diagram of a complete solar device structure that was used in this work.

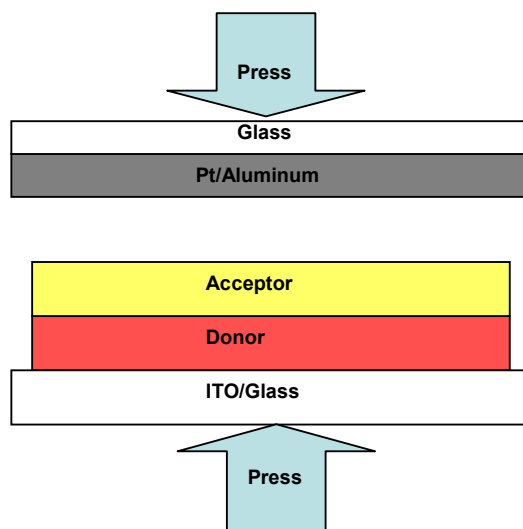


**Figure 3.1:** Schematic diagram of the device fabrication.

## 3.2. MEASUREMENT OF PROPERTIES

### 3.2.1. CONDUCTIVITY MEASUREMENTS

The conductivity measurements were carried out by a four-point probe technique recorded by a Keithley electrometer 2420 model. Samples were tested in a surface cell as well as in a sandwich cell form. Pellets were also used in the case of pure conducting polymers. The specific resistivity was calculated as,

$$\rho = \frac{RA}{t} \quad (3.1)$$

hence,

$$\sigma = \frac{1}{\rho} \quad (3.2)$$

where  $\rho$  is its resistivity,  $R$  is the sample resistance,  $A$  is the cross-sectional area,  $t$  is the thickness, and  $\sigma$  is the conductivity.

### 3.2.2. PHOTOVOLTAIC (I-V) DEVICE CHARACTERIZATION

When light shines on a solar cell, the current that is measured is called the photocurrent. The value of the photocurrent is dependent on many factors in addition to just the quality of the device. The quality of the device, the incident wavelength, intensity of the incident light and the area of the device being illuminated are some of factors that affect the photocurrent. A graph of current (I) versus voltage (V) in Figure 3.2 is a common way to illustrate the properties of solar cells. In the dark, the I–V curve passes through the origin – with no potential, no current flows. But when the device is illuminated (Figure 3.2(b)), the I–V curve shifts downward [1-3] as shown in Figure 3.2 below.

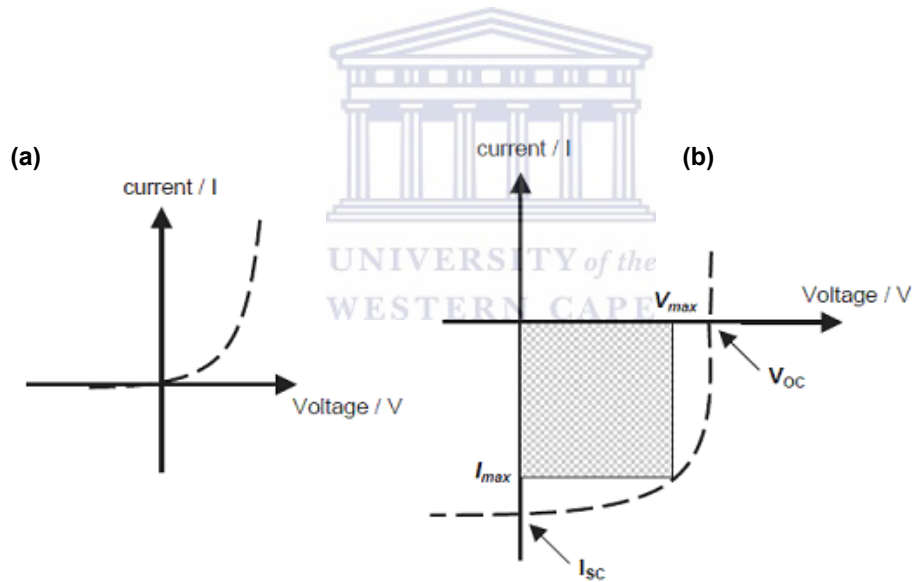


**Figure 3.2:** I–V curves of an organic solar cell under dark (a) and illuminated (b) conditions. The open circuit voltage ( $V_{oc}$ ) and the short-circuit current ( $I_{sc}$ ) are shown. The maximum output is given by the square  $I_{max} \times V_{max}$ .

### 3.2.2.1 Short circuit current

The maximum current the solar cell can put out under given illumination power without an external voltage source connected, is called short circuit current ( $I_{sc}$ ). In the I-V curve, short circuit current is the intersection of the curve with the y-axis (current). It can be measured by connecting both electrodes in an ammeter. In this case, exciton dissociation and charge transport is driven by the so-called built-in potential [4]. The built-in potential is the difference in work function of hole and electron-collecting electrode

### 3.2.2.2 Open Circuit Voltage

The intersection of the curve with the x-axis (voltage) is called open circuit voltage ( $V_{oc}$ ). It is the maximum voltage a solar cell can put up and it is measured by connecting illuminated solar cell to a voltmeter. The open circuit voltage is the influence of the overall organic solar performance; it is directly proportional to the efficiency [5, 6]. In thin film solar cells of the classical geometry metal-insulator-metal,  $V_{oc}$  is equal to work function difference between the two electrodes. In bulk organic solar cells this is not the case, so there still some work to be done to determine the exact origin of  $V_{oc}$  in bulk heterogeneous solar cells. In polymer/fullerene solar cells the  $V_{oc}$  is affected by morphology of the active layer [5].

### 3.2.2.3 Fill Factor

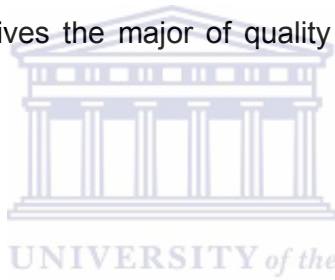
At maximum current ( $I_{sc}$ ) and voltage ( $V_{oc}$ ) the power from solar cell is zero, so the fill factor ( $FF$ ), in conjunction with  $V_{oc}$  and  $I_{sc}$ , determines the maximum power from a solar cell. The  $FF$  is more sensitive to bulk-material

properties, blend morphology, degradation and the physio-chemical morphology of the polymer–cathode interface [7].

The fill factor can be calculated by the following formula:

$$FF = \frac{P_{\max}}{I_{sc} \cdot V_{oc}} = \frac{I_{MP} \cdot V_{MP}}{I_{sc} \cdot V_{oc}} \quad (3.3)$$

where  $I_{MP}$  and  $V_{MP}$  are the current and voltage at the point of maximum power output of the solar cell.  $I_{MP}$  and  $V_{MP}$  can be determined by calculating the power output  $P$  of the solar cell ( $P=I \cdot V$ ) at each point between  $I_{sc}$  and  $V_{oc}$  and finding the maximum of  $P_{max}$ . The theoretical limit of a fill Factor ( $FF$ ) is between 0.25 and 1. It gives the major of quality of I-V characteristics of a solar cell.



#### 3.2.2.4 Air Mass

Air mass (AM) is a measure of how much atmosphere sunlight must travel through to reach the earth's surface. This is denoted as  $AM(x)$ , where  $x$  is the inverse of the cosine of the zenith angle of the sun. A typical value for solar cell measurements is AM 1.5, which means that the sun is at an angle of about  $48^\circ$ . Air mass describes the spectrum of radiation, but not its intensity. For solar cell purposes, the intensity is commonly fixed at  $100 \text{ W/cm}^2$  [3].

#### 3.2.2.5 Power Efficiency

The overall efficiency of a solar cell is called power efficiency ( $\eta$ ). It is defined as the ratio of the electric power output ( $P_{max}$ ) of the cell at the

maximum power point to the incident optical power ( $P_{in}$ ). It can also be expressed in terms of  $I_{sc}$ ,  $V_{oc}$  and  $FF$ .

$$\eta = \frac{P_{max}}{P_{in}} = \frac{I_{sc} V_{oc} FF}{P_{in}} \quad (3.4)$$

where 
$$P_{max} = IV = I_{sc} V_{oc} FF \quad (3.5)$$

In order to describe the power conversion efficiency of a solar cell the maximum output power  $P_{max}$  has to be related to the power of the incident light  $P_{light}$  as shown above in the equation. Power conversion efficiencies are only meaningful for a given spectral distribution and intensity. This can be the solar spectrum or the spectrum of the artificial illumination for indoor applications (for e.g. pocket calculators). In order to compare efficiencies of solar cells, solar radiation standards have been defined in the past. The most common standard at present is the AM1.5 spectrum which can be approached by commercial solar simulator to express  $P_{max}$ . The I-V curves in this study were recorded for the polymer blends and the solar devices using a Keithley Semiconductor Characterization System (SCS). The current was recorded as a function of the changing applied potential across the terminals.

### **3.3. ANALYTICAL TECHNIQUES**

#### **3.3.1. SCANNING ELECTRON MICROSCOPY (SEM)**

The SEM, model JEOL 7500 and LEO 1525 Field Emission was used to provide images of external morphology of the samples. The SEM utilizes a focused beam of high-energy electrons that systematically scans across the



surface of a specimen. The electron beam is generated within an electron gun, accelerated by a high voltage and formed into a fine probe by electromagnetic lenses. The electron-optical column through which the beam passes, is held under high vacuum to allow a free path for the electrons to pass through as well as to prevent high voltage discharge. The first lens that influences the beam is the condenser lens, which causes the beam to converge and pass through a focal point just above a condenser aperture. The intensity of the electron beam when it strikes the specimen, and hence the brightness of the image signal is primarily determined by the condenser lens, in conjunction with the chosen accelerating voltage [9, 10]. The beam diverges again below the condenser aperture and is brought into focus at the specimen through the demagnification of a final lens, the objective lens. This final lens demagnification determines the diameter of the spot size of the electron beam at the specimen, which in turn determines the specimen resolution.

#### **3.3.1.1. Instrumental set-up of a SEM**

The schematic diagram of a SEM instrument is shown in Figure 3.3 with all the important components labeled. All SEM instruments are built around an electron column, which produces a stable electron beam, controls beam current, beam size and beam shape.

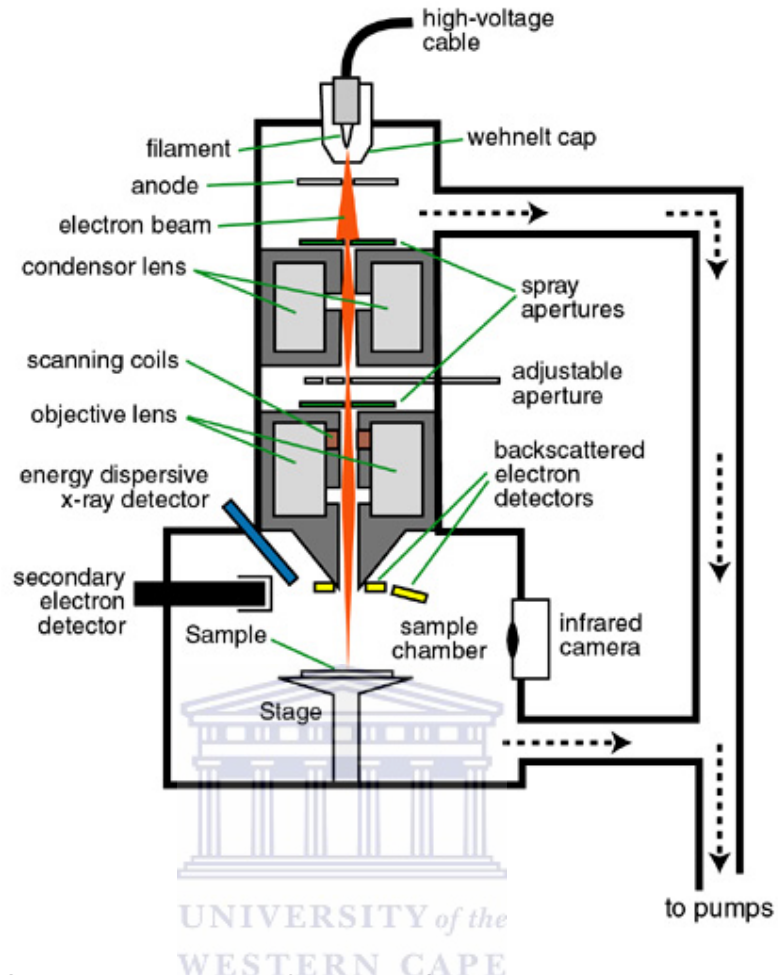


**Figure 3.3:** Schematic diagram of a typical SEM instrument [11].

### 3.3.1.2. Resolution

The degree to which a specimen can be magnified is not the only consideration in microscopy. A far more important factor to consider is its resolution. The limit of resolution is the smallest separation at which two points can be seen as distinct entities. As the resolution improves, the images of the objects tend to separate until they can be independently visualized. This ability of the instrument to resolve fine structure is limited by the diameter of the probe, and the number of electrons contained within the beam. The image is effectively made up of lines of image points, each point being the

size of the beam probe. If a structure is smaller than the probe, it is not resolved. If however, the probe is too small in relation to the area being imaged, it misses out on several smaller regions on the specimen thereby forming a poor quality image. There is a finite relationship between magnification and the optimum probe size to obtain the derived signal level, and it varies from specimen to specimen. Typical resolution levels in modern scanning electron microscopes are around 4 nm. The relationship between resolution and wavelength is given by Abbe's equation [9, 10]:

$$d = \frac{0.612\lambda}{n\sin\theta} \quad (3.6)$$

where  $d$  is the resolution,  $\lambda$  the wavelength of the energy source,  $n$  the refractive index of the medium through which the energy source travels, and  $\theta$  the aperture angle. Abbe's equation signifies the mathematical limit of resolution for an optical system.

When the high energy electron beam interacts with the specimen, a variety of signals may be detected in the scanning electron microscope (Figure 3.4). These signals include secondary electrons, backscattered electrons, transmitted electrons, X-rays (EDX), Cathodoluminescence and Auger electron. The first three types of electronic signals provide visual information about the specimen, while information regarding specimen composition can be determined using characteristic X-rays, Cathodoluminescence and Auger electron signals.

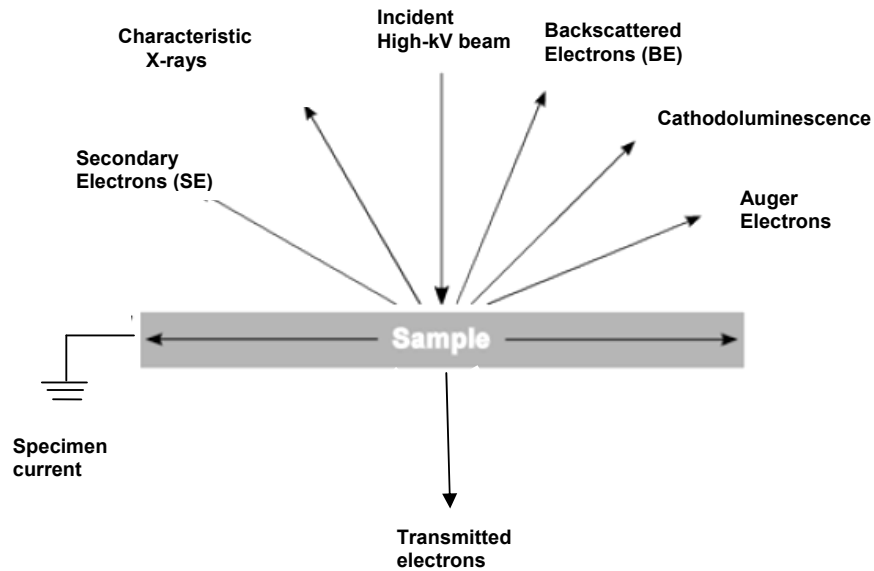


**Figure 3.4:** Illustration of possible signals generated when a high beam interacts with a thin specimen [9, 10].



### 3.3.2. RAMAN SPECTROSCOPY

Raman spectroscopy is a very useful technique for material identification. This molecular spectroscopic technique is used for both quantitative and, mainly, qualitative analysis because of its ease-of-use (e.g. minimal sample preparation) and its non-destructive character [12]. Raman spectroscopy is based on inelastic scattering of monochromatic light, usually from a laser source and it involves illuminating a sample with monochromatic light and using a spectrometer to examine light scattered by the sample. Inelastic scattering means that the frequency of photons in monochromatic light changes upon interaction with a sample. Photons of the laser light are absorbed by the sample and then re-emitted. Frequency of the reemitted

photons is shifted up or down in comparison with original monochromatic frequency, which is called the Raman Effect.

This shift provides information about vibrational, rotational and other low frequency transitions in molecules. The laser beam can be considered as an oscillating electromagnetic wave with electrical vector. Upon interaction with the sample it induces electric dipole moment which deforms molecules. Raman scattering occurs when the system exchanges energy with the photon and the system subsequently decays to vibrational energy levels above or below that of the initial state. The frequency shift corresponding to the energy difference between the incident and scattered photon is termed the Raman shift. Depending on whether the system has lost or gained vibrational energy, the Raman shift occurs either as an up- or down-shift of the scattered photon frequency relative to that of the incident photon.

Because of periodical deformation, molecules start vibrating with characteristic frequency  $\nu$ . Such oscillating dipoles emit light of three different frequencies shown in Figure 3.5. When a molecule with no Raman-active modes absorbs a photon with the frequency  $\nu$ , the excited molecule returns back to the same basic vibrational state and emits light with the same frequency  $\nu$  as an excitation source. This type of interaction is called an elastic Rayleigh scattering [12], Figure 3.5(a).

A photon with frequency  $\nu$  is absorbed by Raman-active molecule which at the time of interaction is in the basic vibrational state. Part of the photon's energy is transferred to the Raman-active mode with frequency  $\nu_1$  and the resulting frequency of scattered light is reduced to  $\nu - \nu_1$ . This Raman frequency is called Stokes frequency or just "Stokes" as shown in Figure

3.5(b). When a photon with frequency  $\nu$  is absorbed by a Raman-active molecule, which, at the time of interaction is already in the excited vibrational state, excessive energy of the excited Raman active mode is released, molecule returns to the basic vibrational state and the resulting frequency of scattered light goes up to  $\nu + \nu_1$ . This Raman frequency is called Anti-Stokes frequency, or just “Anti-Stokes”, Figure 3.5(c).

Most of all the incident photons in spontaneous Raman undergo elastic Rayleigh scattering and only about 0.001% of the incident light produces inelastic Raman signal with frequencies  $\nu \pm \nu_1$ . Spontaneous Raman scattering is very weak and special measures should be taken to distinguish it from the predominant Rayleigh scattering.

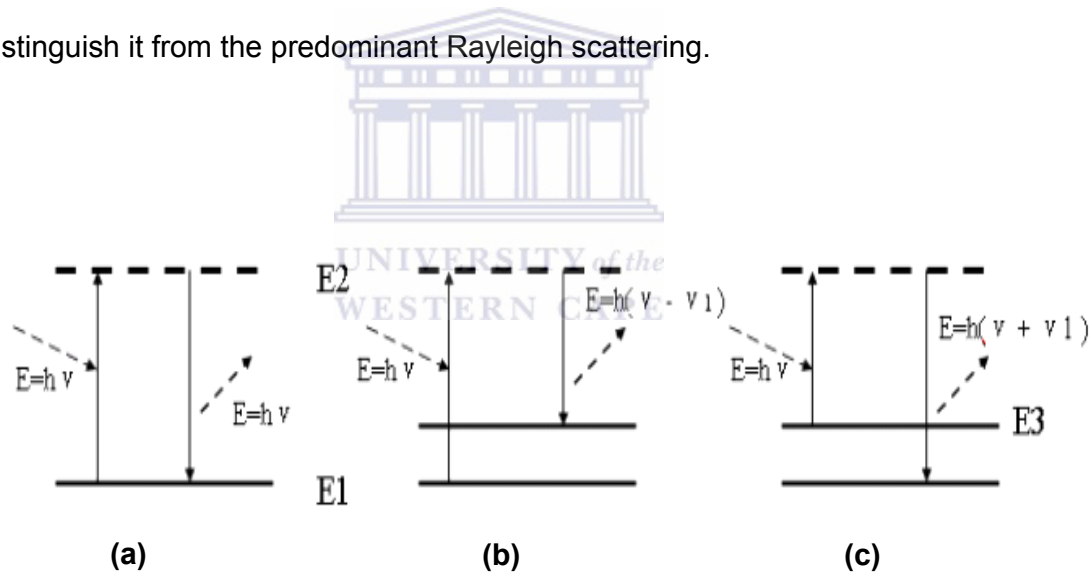


**Figure 3.5:** Three different possible scattering scenarios are shown here.  $E_1$  is the lowest vibrational energy level while  $E_3$  is a excited higher energy level.  $E_2$  is a metastable state.

### 3.3.2.1. Instrumental setup of a Raman spectrophotometer

A schematic diagram of a typical Raman Spectrometer is shown in Figure 3.6. Lasers are used as a photon source due to their highly monochromatic nature, and high beam fluxes because Stokes lines are very weak (~105 times weaker than Rayleigh scattered component). In the system used in this study, a laser is passed into the spectrometer and directed into the microscope by a series of mirrors. The laser is then focused onto the surface of the sample. Light reflects off the sample. This Rayleigh radiation is filtered out at the holographic notch filter. The light then passes through a lens and a slit to filter the light. The light is then passed through another lens, onto a mirror and then onto a grating. The resulting beam of light is then captured on a charge - coupled device (CCD) detector. A computer then interprets the CCD information and displays a spectrum. The laser Raman spectrometer used in this study was a Dilor XY-multi-channel Raman spectrometer, with a 514.5 nm Argon ion excitation laser. In order to reduce heating effects and degradation of the samples the laser power was set at 100 mW, thereby only probing at about 100 nm depth of the sample surface.

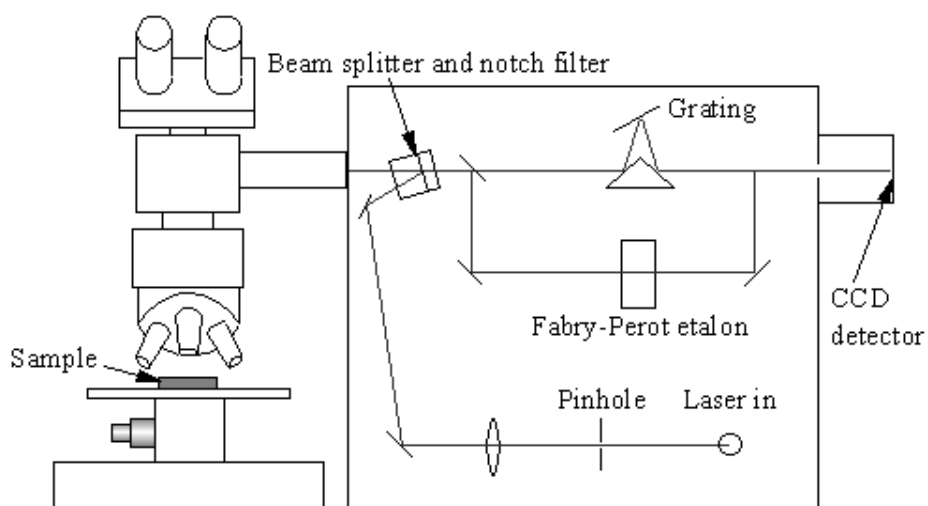


**Figure 3.6:** Schematic diagram of a Raman spectrometer.

### 3.3.3. X-RAY DIFFRACTION

X-ray diffraction was used to identify the crystallinity, crystal size and elemental composition in the samples. A diffractometer with a Cu tube was used with a wavelength  $\lambda = 1.5 \text{ nm}$ . The diffractometer operates in the  $(\theta - 2\theta)$  geometry. The detector rotates at twice the rate of the sample and is at an angle of  $2\theta$  with respect to the incoming X-ray beam. The X-rays reflected from the different planes in the crystal undergo interference with each other as illustrated in Figure 3.7.

The basis for X-ray diffraction is described by the Bragg's law, equation 3.7, which describes the condition of constructive interference of X-rays, scattered from atomic planes of a crystal by this equation:

$$n\lambda = 2d\sin\theta \quad (3.7)$$



where  $n$  is an integer,  $\lambda$  is the wavelength of the radiation,  $d$  is the spacing between atomic planes and  $\theta$  the angle between the radiation and atomic planes, known as the Bragg angle [13]. This relation demonstrates that interference effects are observable only when radiation interacts with physical dimensions that are approximately the same size as the wavelength of the radiation. During the first order reflection constructive and destructive interference takes place. Constructive interference occurs if the rays that are scattered by all atoms in all the planes are in phase and reinforce one another to form a diffracted beam. While in destructive interference all the scattered beams are out of phase and cancel one another leading to no scattering. For the first order diffraction,  $n = 1$ , the Bragg's law can be written as:

$$\lambda = 2d \sin \theta \quad (3.8)$$

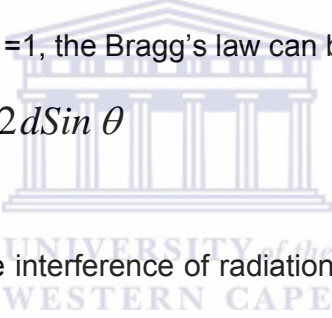
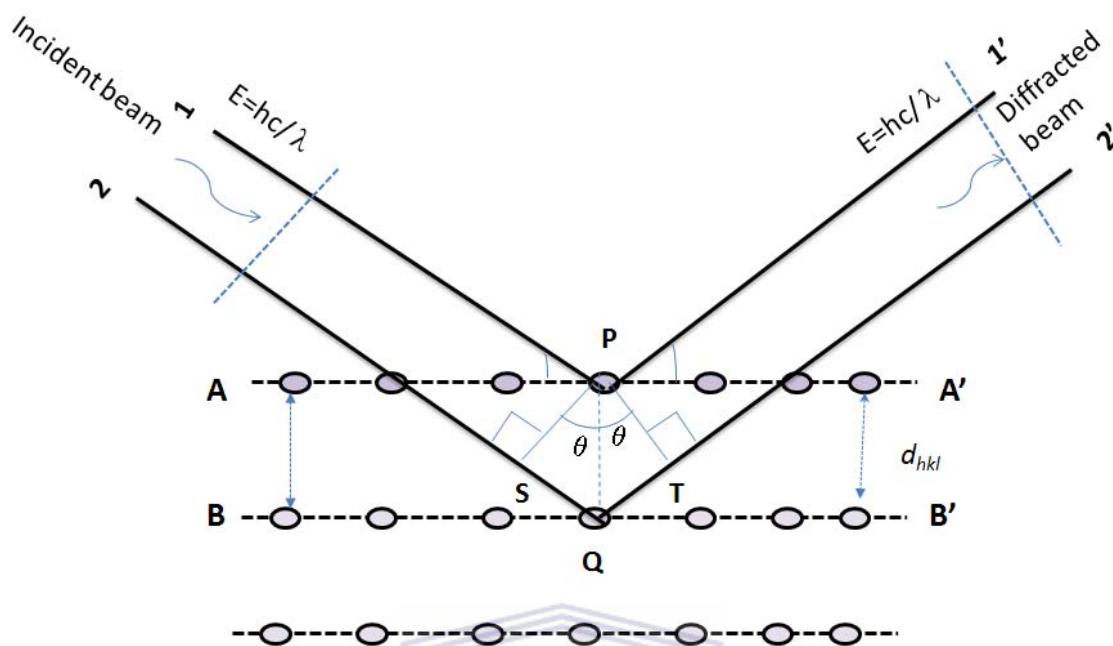
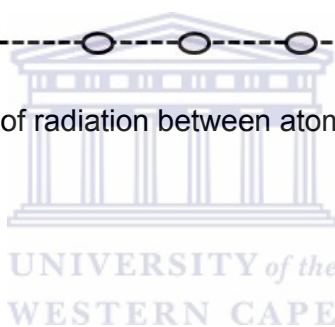


Figure 3.7 show the interference of radiation between atomic planes in a crystal. Two parallel planes of atoms A–A' and B–B' which have the same  $h$ ,  $k$ , and  $l$  Miller indices separated by the interplanar spacing  $d_{hkl}$  are shown in Figure 3.7. If we assume that a parallel, monochromatic, and coherent (in-phase) beam of X-rays of wavelength  $\lambda$  is incident on these two planes at an angle  $\theta$ . Two rays in this beam, labeled 1 and 2, are scattered by atoms P and Q. Constructive interference of the scattered rays 1' and 2' occurs also at an angle  $\theta$  to the planes, if the path length difference between 1–P–1' and 2–Q–2' is equal to a whole number,  $n$ , of wavelengths. That is the condition for Bragg's law.



**Figure 3.7:** Interference of radiation between atomic planes in a crystal



### 3.3.3.1. Instrumental setup of an X-ray diffractometer

When the incident beam strikes a powder sample, diffraction occurs in every possible orientation of  $2\theta$ , this is shown in the schematic diagram of XRD (Figure 3.8). The diffracted beam may be detected by using a moveable detector which is connected to a chart recorder. In normal use, the counter is set to scan over a range of  $2\theta$  values at a constant angular velocity.

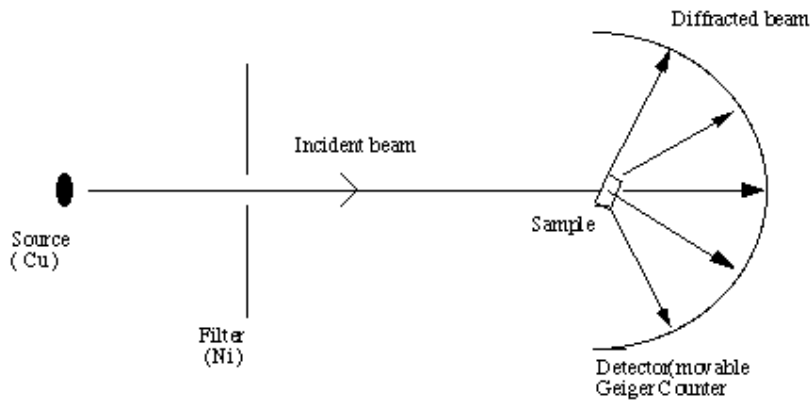


**Figure 3.8** Schematic representation of a typical X-ray diffraction Instrument.

There are two limiting angles  $2\theta_1$  and  $2\theta_2$  on both sides of the diffraction peak beyond which the diffracted intensity must drop to zero. It follows that the diffracted intensity at angles near  $2\theta_B$  ( $2\theta_2 \leq \theta \leq 2\theta_1$ ) is not zero but intermediate between zero and the maximum intensity of the beam diffracted at an angle  $2\theta_B$ . The curve of the diffraction intensity versus  $2\theta$  will have the form of Figure 3.9(a) in contrast to Figure 3.9(b), which illustrate the hypothetical case of diffraction occurring at the exact Bragg angle.

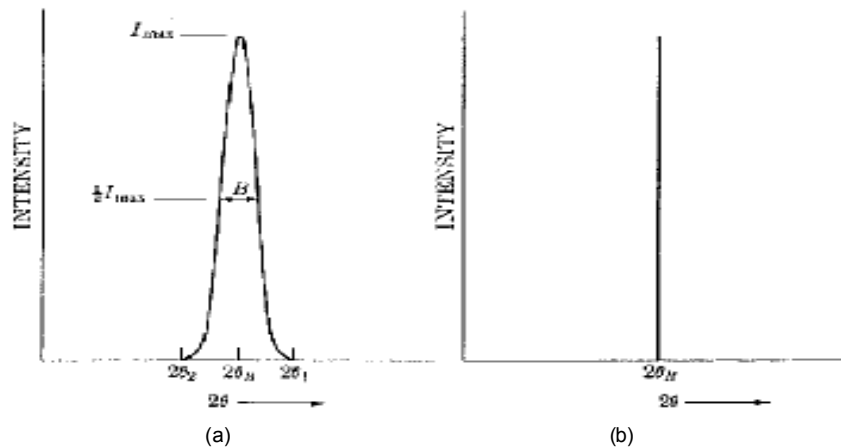


**Figure 3.9:** The effect of fine particle size on diffraction curves [14, 13].

### 3.3.4. CYCLIC VOLTAMMETRY (CV)

Cyclic voltammetry has become an important and widely used electroanalytical technique in many areas of chemistry. It is mostly used for the study of redox processes due to its simplicity, versatility and is also used for understanding reaction intermediates of reaction products. The electrode potential at which a polymer undergoes reduction or oxidation can be rapidly located by CV. Furthermore, CV reveals information regarding the stability of the product during multiple redox cycles. Since the rate of potential scan is variable, both fast and slow reactions can be followed. A very important aspect of this method is its ability to generate a new redox species during the first potential scan and then probe the fate of species on the second and subsequent scans. Therefore, CV allows the growth of a polymer film along with its further characterization during a single experiment. The cyclic

voltammetry process can be reversible, irreversible or quasi-reversible [15, 16].

In cyclic voltammetry (CV), the potential is increased linearly from an initial potential ( $E_i$ ) to a peak potential ( $E_p$ ) and back to the initial potential again, while the current response is measured. For freely diffusing species, as the potential is increased, easily oxidized species near the electrode surface react, and a current response is measured. When the direction of the scan is reversed, the oxidized species near the electrode surface are reduced, and again a current response is measured [16]. Figure 3.10 shows a typical cyclic voltammogram for a single scan (Figure 3.10(a)) and the one for different scan rates (Figure 3.10(b)). The reversible system is shown in the Figure 3.10(a). The Randles-Sevcik equation 3.10 [17] states that the peak current  $I_p$  is given by:


$$I_p = -2.6 \times 10^5 n^{3/2} C_o^\infty D^{1/2} \nu^{1/2} \quad (3.10)$$

where  $n$  is the number of electrons,  $C_o$  is the bulk concentration of the electroactive species ( $\text{mol cm}^{-3}$ ),  $D$  is the diffusion constant ( $\text{cm}^2 \text{s}^{-1}$ ) and  $\nu$  is the scan rate ( $\text{Vs}^{-1}$ ). Therefore, for diffusion controlled system, the peak current is proportional to the square root of the scan rate. Of course the rules change in electroactive polymer electrochemistry, because the polymer is adhered to the electrode surface. Therefore, the process is not diffusion controlled, and cannot be described by the Randles-Sevcik equation discussed above. Instead, the peak current for a surface bound species is given by the following equation [18, 19]:

$$I_p = \frac{n^2 F^2 \Gamma V}{4RT} \quad (3.11)$$

where  $\Gamma$  is the concentration of surface bound electroactive centers (mol/cm<sup>2</sup>) and  $F$  is Faradays constant (96,485 C/mol). Thus, if a species is surface bound, both the anodic and cathodic peak current will scale linearly with scan rate. In a scan rate dependence experiment, the electroactive polymer is washed and placed in monomer- free electrolyte solution, and the polymer is then cycled between its oxidized and reduced forms at various scan rates while the  $I_p$  of both oxidation and reduction is monitored. If the  $I_p$  scales linearly with scan rate, then the process is said to be non-diffusion controlled, and the electroactive centers of the polymer are adhered to the electrode surface.

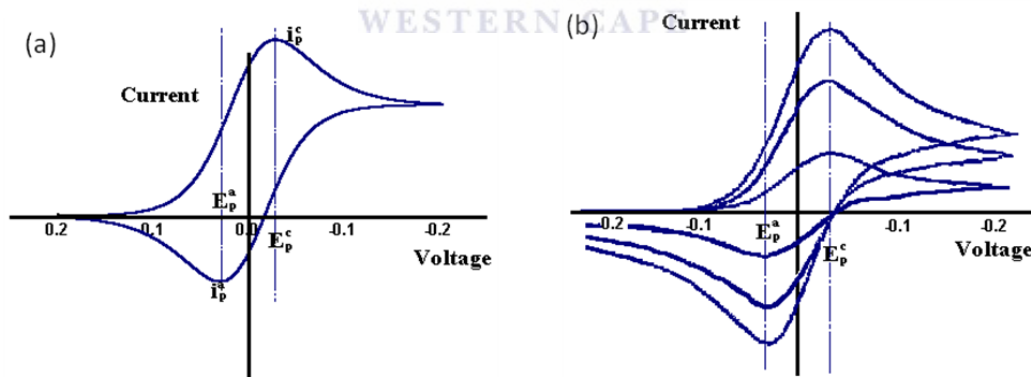


**Figure 3.10:** Reversible cyclic voltammogram (a) and cyclic voltammogram with different scan rates (b)

### 3.3.4.1. Instrumental set-up of a Cyclic Voltammetry

Figure 3.11 shows a schematic diagram of a cyclic voltammetry. The tip represents the working electrode which is and can be a platinum/glassy carbon. The reference electrode is silver in silver chloride (Ag/AgCl) and the auxiliary cab is a platinum wire/mash. These electrodes are connected to the potentiostat which feed the information to the computer.

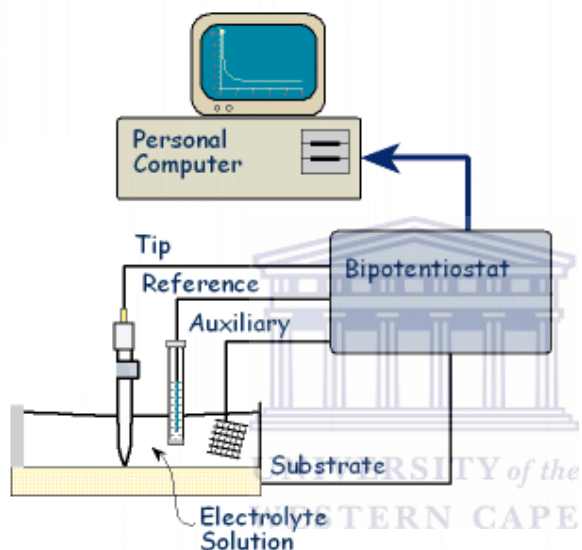


**Figure 3.11:** Schematic diagram showing a typical CV.

In this thesis the BAS/100W integrated automated electrochemical workstation (Bioanalytical Systems, Lafayette, IN, USA) was used for cyclic voltammetry analysis. A Pt disk ( $1.77 \times 10^{-2} \text{ cm}^2$ ) was used as the working electrode, Platinum wire was used as the counter electrode, and silver wire was used as the reference electrode. The cyclic voltammetry was performed in the 1 M HCl. A small amount of sample was mixed with 1 M HCl to make a paste. The paste was prepared in such a way as to create the electrolyte

environment (not too thick). The three electrodes were dipped into a paste. The CV was performed between 5 and 100 mVs<sup>-1</sup> scan rates.

### 3.3.5. ULTRAVIOLET AND VISIBLE SPECTROSCOPY (UV-VIS)

UV-Vis has become the most important analytical instruments for the last 40 years because of its simplicity, versatility, speed, accuracy and cost-effectiveness [16]. Different molecules absorb radiation of different wavelengths. An absorption spectrum will show a number of absorption bands corresponding to structural groups within the molecule. For example, the absorption that is observed in the UV region for the carbonyl group in acetone is of the same wavelength as the absorption from the carbonyl group in diethyl ketone. UV-Vis has three types of electronic transition, (1) transitions involving  $\pi$ ,  $\sigma$ , and  $n$  electrons (2) charge-transfer electrons (3) and  $d$  and  $f$  electrons (not covered in this thesis) [20]. When an atom or molecule absorbs energy, electrons are promoted from their ground state to an excited state. In a molecule, the atoms can rotate and vibrate with respect to each other. These vibrations and rotations also have discrete energy levels, which can be considered as being packed on top of each electronic level. Figure 3.12 show the example of different electronic transitions.



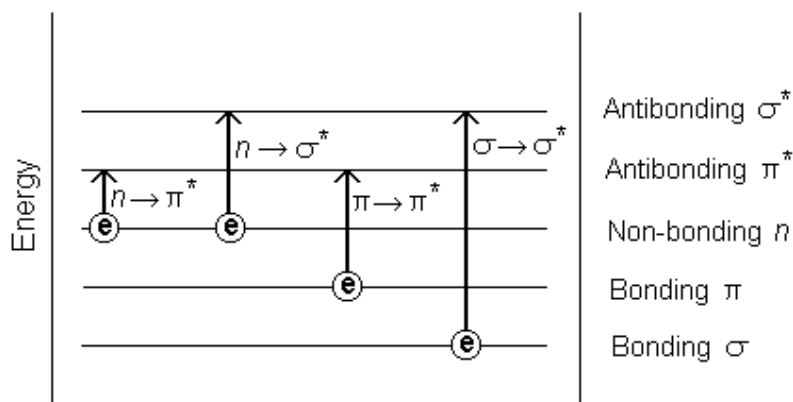


**Figure 3.12:** Possible electronic transitions of  $\pi$ ,  $\sigma$ , and  $n$

From Figure 3.12 it can be seen that when an electron  $\sigma$  bonding is excited to the anti-bonding ( $\sigma - \sigma^*$  transitions) a large energy is required. Most of these transitions show a maximum wavelength which is less than 200 nm. Saturated compounds containing atoms with lone pairs (non-bonding electrons) are capable of  $n - \sigma^*$  transitions. These transitions usually need less energy than  $\sigma - \sigma^*$  transitions. They can be initiated by light whose wavelength is in the range 150 - 250 nm. The number of organic functional groups with  $n - \sigma^*$  peaks in the UV region is small. Most absorption spectroscopy of organic compounds is based on transitions of  $n$  or  $\pi$  electrons to the  $\pi^*$  excited state. This is because the absorption peaks for these transitions fall in an experimentally convenient region of the spectrum (200 - 700 nm). These transitions need an unsaturated group in the molecule to provide the  $\pi$  electrons. The solvent in which the absorbing species is dissolved also has an effect on the spectrum of the species. With an increase in solvent polarity, peaks resulting from  $n - \pi^*$  transitions are shifted to shorter wavelengths (blue shift). This is due to increased solvation of the lone pair,

which lowers the energy of the  $n$  orbital. Most of the time, the reverse (i.e. red shift) is seen for  $\pi - \pi^*$  transitions. Many inorganic and some organic species show charge-transfer absorption and are called charge-transfer complexes. For a complex to demonstrate charge-transfer behavior one of its components must have electron donating properties and another component must be able to accept electrons. Absorption of radiation then involves the transfer of an electron from the donor to an orbital associated with the acceptor [20].

### 3.2.5.1. Instrumental set-up of a UV-Vis Spectrophotometer

UV-Visible (UV-Vis) absorption spectroscopy involves passing a monochromatic beam of light through a sample and measuring the absorption wavelength of the material, Figure 3.13. This absorption is measured as a function of frequency over a frequency range from infrared to ultraviolet. The absorption is usually measured in reference to a blank sample in a double beam arrangement, to eliminate variations caused by the differences in lamp intensities at different frequencies. Typically, measurement ranges here were 900 nm down to 200 nm.

As the photons pass through a material, it is possible that photons of a suitable energy can interact with the material, resulting in an electron being excited to a higher energy state, and the photon being absorbed. By measuring the amount of light absorbed for a particular wavelength, it is possible to deduce information about the electronic structure of the material. In conjugated polymers, UV-Vis absorption is primarily due to  $\pi - \pi^*$  transitions, as the energy gap between these levels ranges from near UV to

infrared. Excitations from  $\pi$  electrons are in the near to far ultraviolet, so these are correspondingly left unaffected by the measurements in this study. As ultraviolet light affects these  $\pi$  bonds, it tends also to alter the polymer's structure, resulting in photo-degradation of the polymer. Different parts of the polymer are excited at different frequencies. This is useful as it allows us to use UV-Vis spectroscopy as a probe to determine how the polymer is affected by changes in its environment due to such factors as solvent interaction, concentration changes leading to aggregation, and in this case, the introduction of nanotubes to a polymer solution.



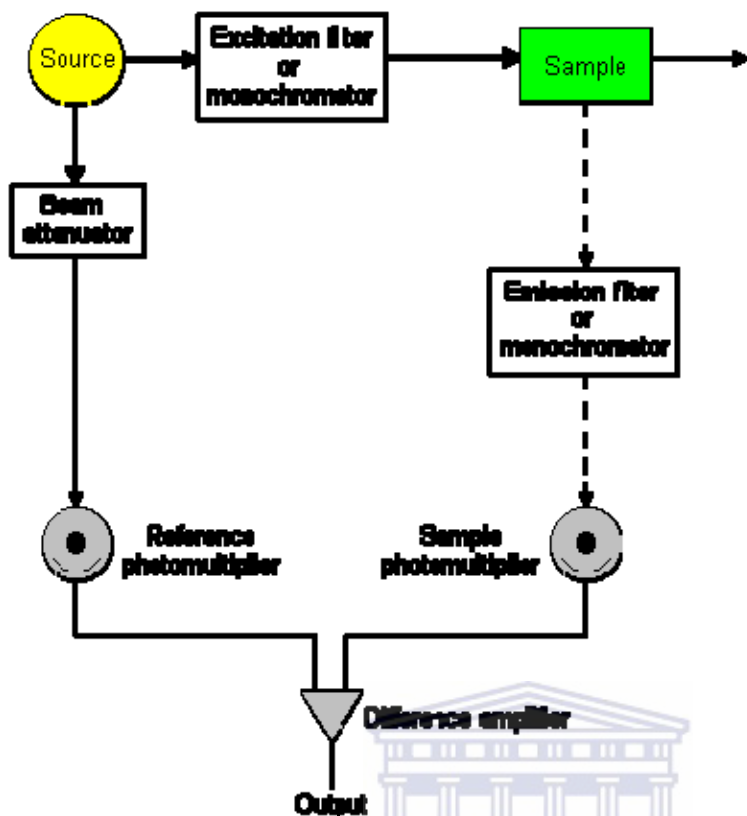


Figure 3.13: Schematic diagram of a UV-Vis instrument showing the important parameters and the direction of light from the light source.

### 3.3.6. PHOTOLUMINESCENCE

Photoluminescence spectroscopy is a versatile, non-destructive method of probing the electronic structure of a material. Photoluminescence requires the following components to operate: a sample, a light source, light filtering system and a detector. The light from the light source hits the sample causing production of excitons as well as electron interactions, Figure 3.14. Some of these interactions cause an emission of light, which is then filtered to its different energies and then recorded by the detector. Photoluminescence can be used to get the number of defects that are in a type of electronic

material. The less defects a substance has, the better efficiency it has when used in electronics and thus the more predictable it will behave during usage. This is very vital because if someone need to flow a large charge in one way in an electrical circuit these defects could get charge going to opposite way leading to anything from a short circuit to a potentially fatal shock [21]. Figure 3.14 shows a schematic diagram of a typical photoluminescence spectroscopy instrument.

Fluorescence spectroscopy is a useful companion technique to absorption spectroscopy, in that as absorption spectroscopy probes the energies of excitations to higher states, fluorescence spectroscopy probes the energies at which these excited electrons radiate as they decay back to the ground state. Usually a fixed wavelength is used to excite the polymer, and a range of wavelengths are examined for light emitted as the electron decays, giving information about the electronic transitions available to the electron as it decays.

When a pi-electron in a solid is excited by a photon, it is promoted into an unstable excited state. This excess energy may be lost in a number of ways, both radiative and non-radiative. This involves the loss of energy of photons and vibrational phonons respectively. On excitation, the electron finds itself in an excited vibronic state of the excited electronic state. Neglecting intersystem crossing and internal conversion, the electron falls very rapidly to the lowest energy state of the vibrational manifold. It is only now ready to undergo radiative decay. The electron can decay into any vibrational state of the ground electronic state with probability amplitude related to the overlap of

the wavefunctions of the initial and final state. Thus, the luminescence profile is indicative of the vibrational structure of the ground state.

### 3.3.6.1 Instrumental set-up of a PL spectrometer

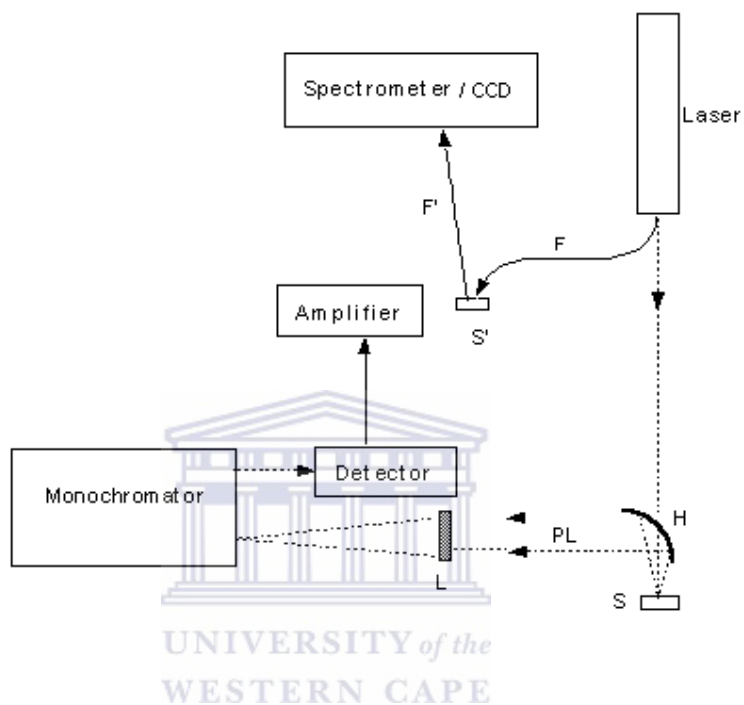


**Figure 3.14:** Schematic diagram of a typical photoluminescence spectroscopy instrument. The laser beam passes through the hole H of a parabolic mirror the PL emitted by the sample S is reflected by the mirror, focused by the lens L and sent to a high-resolution grating spectrometer

### 3.4. REFERENCES:

- [1]. Spanggaard, H.; Krebs, F. C., A brief history of the development of organic and polymeric photovoltaics. *Solar Energy Materials and Solar Cells* **2004**, 83, (2-3), 125-146.
- [2]. Nunzi, J.-M., Organic photovoltaic materials and devices. *Comptes Rendus Physique* **2002**, 3, (4), 523-542.
- [3]. Benanti, T.; Venkataraman, D., Organic Solar Cells: An Overview Focusing on Active Layer Morphology. *Photosynthesis Research* **2006**, 87, (1), 73-81.
- [4]. Atienzar, P.; Ishwara, T.; Illy, B. N.; Ryan, M. P.; Regan, B. C.; Durrant, J. R.; Nelson, J., Control of Photocurrent Generation in Polymer/ZnO Nanorod Solar Cells by Using a Solution-Processed TiO<sub>2</sub> Overlayer. *The Journal of Physical Chemistry Letters* **2010**, 1, (4), 708-713.
- [5]. Patyk, R. L.; Lomba, B. S.; Nogueira, A. F.; Furtado, C. A.; Santos, A. P.; Mello, R. M. Q.; Micaroni, L.; Hümmelgen, I. A., Carbon nanotube–polybithiophene photovoltaic devices with high open-circuit voltage. *physica status solidi (RRL) – Rapid Research Letters* **2007**, 1, (1), R43-R45.
- [6]. Goetzberger, A.; Hebling, C.; Schock, H.-W., Photovoltaic materials, history, status and outlook. *Materials Science and Engineering: R: Reports* **2003**, 40, (1), 1-46.
- [7]. Gupta, D.; Mukhopadhyay, S.; K. Narayan, S., Correlating reduced fill factor in polymer solar cells to contact effects. *Applied Physics Letters* **2008**, 92, (9), 93301-93303.

- [8]. Gunes, S.; Neugebauer, H.; Sariciftci, N., Conjugated Polymer-Based Organic Solar Cells. *Chemical Reviews* **2007**, 107, (4), 1324-1338.
- [9]. Postek Jr, M.T.; **1980**. Scanning Electron Microscopy-A Students Handbook. *Ladd Research Industries, Inc.*
- [10]. Goodhew J.; Humphreys, F.J., **1988**. Electron Microscopy and Analysis, 2<sup>nd</sup> Edition, *Taylor & Francis, London.*
- [11]. [www4.nau.edu/.../Images/SEM\\_schematic.jpg](http://www4.nau.edu/.../Images/SEM_schematic.jpg)
- [12]. [http://content.piaction.com//Raman\\_spectroscopy\\_basics.pdf](http://content.piaction.com//Raman_spectroscopy_basics.pdf)
- [13]. Skoog, D.A.; Holler, F.J.; Nieman, T. A.; **1998**. Principles of Instrumental Analysis 2<sup>nd</sup> Edition. *Harcourt Brace College Publishers.*
- [14]. Hall, H.S.,**1999**. The Design and Implementation of a Photoluminescence Experiment.  
[http://www.physics.ohiostate.edu/reu/99reu/final\\_reports/paper\\_hall](http://www.physics.ohiostate.edu/reu/99reu/final_reports/paper_hall).
- [15]. Bard, J.; Faulkner, L.R., **2001**. Electrochemical methods, Fundamentals and Applications 2<sup>nd</sup> Edition. *John Willey & Sons, INC.*
- [16]. Brett, C.M.A.; Brett, A.M.O., **1993**. Electrochemistry Principles, Methods, and Applications. *Oxford Science Publications.*
- [17]. Abruna, H. Tri-tert-butylazadiboriridine: a molecule with a basic boron-boron bond. *Coordination Chemistry Reviews* **1998**, 176, 135-155.
- [18]. Lane, R.F.; Hubbard, A.T., Electrochemistry of chemisorbed molecules. I. Reactants connected to electrodes through olefinic substituents. *The Journal of Physical Chemistry* **1973**, 77, (11), 1401-1410.
- [19]. Armstrong, R. D.; Henderson, M., Impedance plane display of a reaction with an adsorbed intermediate. *Journal of Electroanalytical Chemistry* **1972**, 39, (1), 81-90.



- [20]. Thermo Spectronic, *Basic UV-Vis Theory, Concepts and Applications*.  
<http://www.molecularinfo.com/MTM/UV.pdf>.
- [21]. Lemmer, U.; Gobel, E.O., *Photoluminescence Spectroscopy as Probe for Disorder and Excitonic Effects in Organic and Inorganic Semiconductors* Chapter 9. <http://www.ipc.unilinz.ac.at/publ/book/Chapter9.pdf>.



# CHAPTER FOUR

---

## SYNTHESIS AND CHARACTERIZATION OF NOVEL NANOPHASE HEXAGONAL POLY(2,5-DIMETHOXYANILINE)

### 4.1. INTRODUCTION

Since the discovery of carbon nanotubes in 1991 by Sumio Iijima [1], there has been an increased interest in one-dimensional nanostructures (nanorods, nanotubes, nanowires and nanobelts) of conjugated polymer materials because they combine the optoelectronic properties of semiconductors with the mechanical properties and processing advantages of plastics [2-4]. Previous studies have shown that the electron and ion transportation properties of conducting polymers are strongly dependent on its morphology [5]. These materials have potential applications in various fields including chemical sensors, gas-separation membranes, light emitting, electrochromic and electronic devices [6-10]. Among conducting polymers, polyaniline (PANI) has been one of the most studied owing to its high conductivity, environmental stability and low cost of production. PANI exists in three forms, e.g. fully reduced leucoemeraldine, half oxidized emeraldine and fully oxidized pernigraniline. Polyaniline can be synthesized chemically or electrochemically [3, 6].

PANI has many potential applications in various fields including anticorrosion, sensors, electrochromic devices and electronic devices. One drawback of PANI which continues to be a problem is its poor processability. PANI in itself is not soluble in common solvents and it decomposes before it melts. In order to improve its processability a few authors have reported on the complexation of polyanilines with sulphonic acids in order to improve the solubility of PANI [6-8]. Nanoparticles synthesised by the dispersion of PANI in polymeric stabilizers has also been reported [6]. Another method to improve the processability of PANI is to use polymers of substituted polyaniline e.g. poly(2,5-dimethoxyaniline), poly(2-methoxyaniline), poly(methylaniline) etc. [7, 9]. It is believed that the substituents in polymer chains decrease the stiffness of the polymers making it easier to dissolve [9, 10]. Unlike the mono-substituted polyanilines which has been reported to have low conductivity, di-substituted polyaniline like poly(2,5-dimethoxyaniline) has been reported to have conductivity similar to that of PANI and are soluble in most organic solvents [11].

One-dimensional nanostructures of PANI have been synthesized by chemical or electrochemical oxidative polymerization of the monomer with the aid of “hard templates” such as zeolite, track-etched polymeric membranes and porous alumina, seed nanofibres, and polymer fibres [12]. Although the electrochemical synthesis of PANI has the advantage of being more pure, the chemical synthesis is preferred because it can be synthesized in large quantities which are attractive from a practical point of view. Self-assembly or “soft template” methods have also been used to prepare one-dimensional

PANI nano-structured materials. Zhang has reported that PANI nanorods and nanotubes can be synthesized without the surfactant [13]. Iwuoha *et al.* [5] showed that nanorods and nanofibres of polyaniline can be synthesized in the present fly ash by in-situ polymerization of aniline. Bai *et al.* [14] reported the formation of cluster nanorods by binary oxidant system employing potassium dichromate and ammonium per sulphate (APS). It has been reported that one-dimensional nanostructures are good electron transport materials which are good for application in photovoltaic device. In this paper we report the chemical synthesis and electrochemistry of novel nanophase hexagonal poly(2,5-dimethoxyaniline) PDMA nanostructured by oxidative polymerization (APS) and ferric chloride( $\text{FeCl}_3$ ) as an oxidant.

## 4.2. EXPERIMENTAL DETAILS

### 4.2.1. MATERIALS

Aniline (99%), 2,5-dimethoxyaniline, ammonium per sulphate (APS),  $(\text{NH}_4)_2\text{S}_2\text{O}_8$ , 98%), dimethyl formamide (DMF, 99%) and ferric chloride ( $\text{FeCl}_3$ ) were purchased from Sigma Aldrich. All chemicals were used as received without further purification.

### 4.2.2. SYNTHESIS OF PANI AND POLY(2,5-DIMETHOXYANILINE) (PDMA)

PANI and PDMA were synthesized by chemical oxidation of their respective monomers. In a 50 mL flask a 0.2 g of 2,5-dimethoxyaniline was dissolved in a solution of 2 mL HCl in 20 mL distilled water. The solution was stirred for 30 min at 50 °C where after 0.48 g of APS and 0.375 g of  $\text{FeCl}_3$  was added respectively in the solution. The resultant mixture was stirred for

another 3 h at 50 °C. The contents of the reaction were put in the oven at 70 °C overnight to evaporate the solvents. The remaining contents were washed with ethanol and dried at 70 °C.

#### **4.2.3. CHARACTERIZATION**

The SEM samples were prepared by placing some of the synthesized material onto an aluminum stub. A carbon sticky tape was placed on the aluminum stub for adhesion of the material. The samples were sputter-coated with a thin layer of gold (Au) to prevent charging effects inside the microscope. The morphology of the prepared materials was examined on a LEO 1525 Field emission scanning electron microscope (SEM) with beam energy at 10 kV. UV–Vis spectra were recorded on a Nicolet Evolution E 100 spectrometer from 320 to 800 nm. The UV-Vis samples were prepared by dissolving about 0.005 g of a material in 10 mL DMF. Infrared spectra were recorded using an FTIR spectrometer (Perkin Elmer Spectrum 100) to identify the chemical structure of PANI and PDMA respectively. A small amount of material was placed on the diamond coated detector and pressed onto the electrode for FTIR measurements. Thermo-gravimetric analysis (TGA) was performed using a TGAQ500 thermogravimetry analyser. 5 mg of material were placed on a platinum (Pt) boat and inserted into the chamber for TGA analysis. Measurements were carried out in nitrogen (N<sub>2</sub>) atmosphere at a heating rate of 10 °C/min from room temperature to 800 °C. Cyclic voltammetry (CV) experiments were performed using a BAS 100W potentiostat (Bioanalytical Systems (BAS), Lafayette, IN, USA) in a cell system consisting of a 0.071 cm<sup>2</sup> Pt disk working, Ag/AgCl reference (3 M KCl

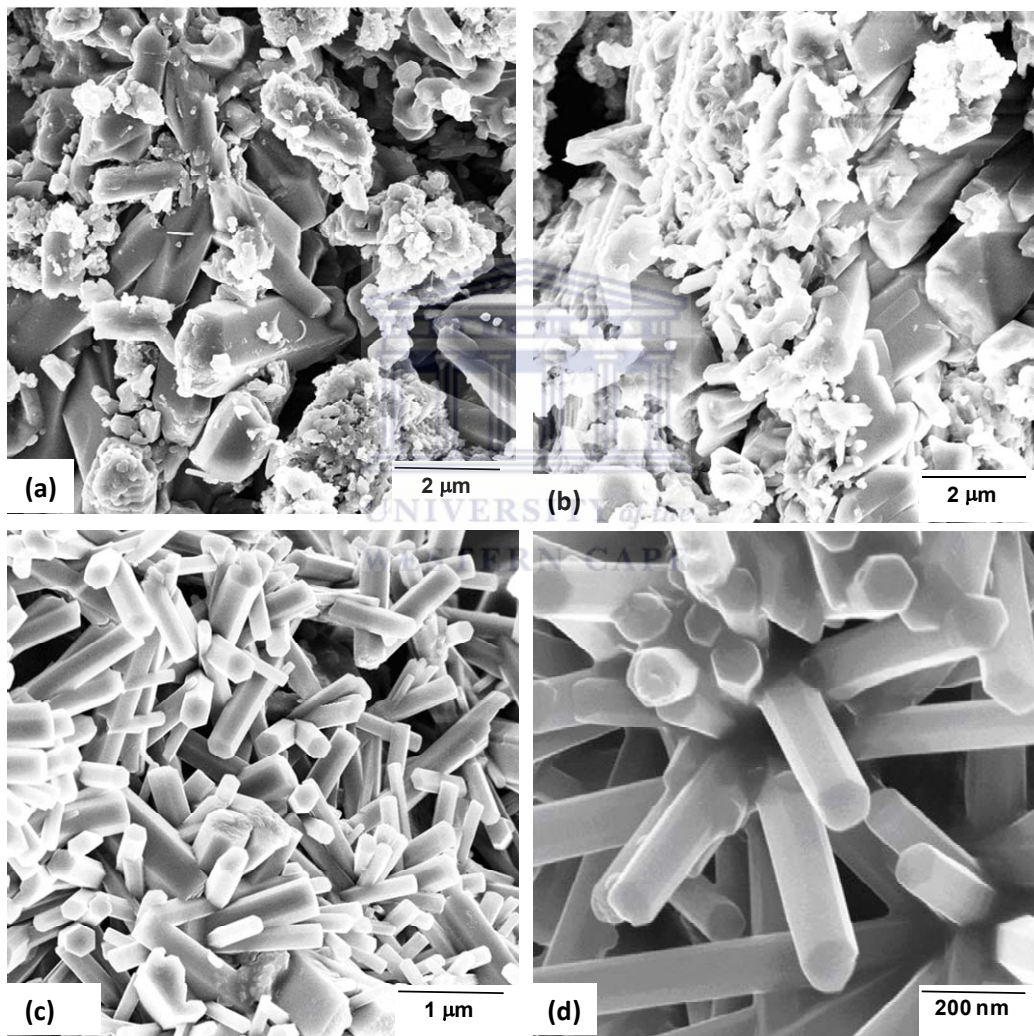
type) and a Pt wire counter electrodes laced in a paste of material prepared with 1 M HCl. The electrochemical paste cell system consisted of homogeneous slurries made with 0.05 g material and 5 mL 1 M HCl. The paste cell was de-aerated for fifteen min with argon, and a headspace argon atmosphere was maintained at very low flow rate during analysis. Voltammograms were recorded at room temperature, scanning anodically ( $E_i = 0$  mV and  $E_{\lambda} = +800$  mV) at potential scan rates of 5–25 mV/s.

### 4.3. RESULTS AND DISCUSSION

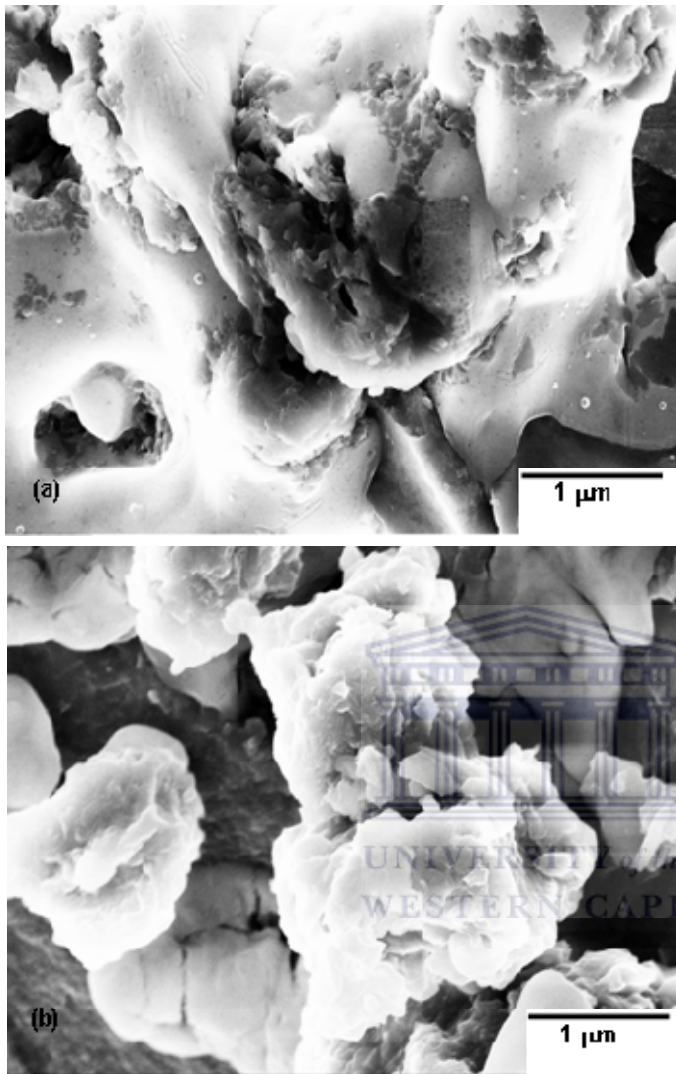
#### 4.3.1. MORPHOLOGY

Figure 4.1 shows the field-emission scanning electron microscopy (FE-SEM) images of the surface appearance of PANI and PDMA. The SEM micrographs of PANI (Figure 4.1(a) and (b)) show a mixture of fibrous and an aggregation of 6 x 20 nm polyaniline hexagonal rods to form 6 x 1 nm supra-hexagonal structures. The fibrous might be due to impurities since aniline was not distilled before use. Polyaniline images also showed the formation of “cone-like” structures and the dispersal of 15-200 nm size nanoparticles on the surface of the hexagonal PANI structures. The PDMA SEM images (Figure 4.1(c) and (d)) showed well defined homogeneous 6 x 50 nm hexagonal structures with smooth surfaces. No hexagonal structures were formed when APS or FeCl<sub>3</sub> alone was used as the oxidant as shown in Figure 4.2. It can thus be concluded that the hexagonal structures only forms when two oxidants are used at a temperature of 70 °C. The hexagonal close packing of the polymer is expected to increase the conductivity of the polymer. This is in good agreement with results reported by Dong *et al.* [15] which

showed that the diameter of polyaniline/multiwalled carbon nanotubes (MWNTs) composites became larger than that of pure MWNTs after *in situ* polymerization. They also showed that the composites have porous fibrous structure which may cause considerable increase of the conductive pathway resulting in high conductivity.



**Figure 4. 1:** Scanning electron micrographs of PANI (a) and (b); and PDMA (c) and (d).



**Figure 4.2:** Scanning electron micrographs of PDMA prepared with only one oxidant (a) APS and (b) FeCl<sub>3</sub>.

#### **4.3.1.1. MECHANISM FOR THE FORMATION OF THE HEXAGONAL NANOSTRUCTURES**

Although the mechanism for the formation of one-dimensional PANI morphologies is not fully understood, it is accepted that PANI



nanorods/nanotubes are formed by the propagation of micellar intermediates [4, 5]. The micelles are formed by complexation of aniline with HCl in the aqueous mixture. Micelles are said to grow in the presence of salts, from spherical rod-like to cylindrical aggregates or worm-like micelles. The polymerization normally takes place at the micelle/water interface because the oxidants used are water soluble.

As polymerization continues, the micelles become large spheres by accretion or rods/tubes by elongation [5]. Micelles, or soft rectangular tubules, or spherical balls (from aggregated micelles) formed during the polymerization process function as templates, and the PANI nanostructures formed may follow the outer shape of the template [16, 17]. In this study the formation of micelles are as a result of the  $\text{Cl}^-$  and  $\text{S}_2\text{O}_8^{2-}$  salts of the anilinium ions present in the polymerization solution. The clustering of the micelles produced independently by the two oxidants,  $(\text{NH}_4)_2\text{S}_2\text{O}_8$ , and  $\text{FeCl}_3$ , result in the formation of nanotubes. A schematic diagram of the mechanism for the formation of hexagonal PANI and PDMA nanostructures is shown in Figure 4.3.

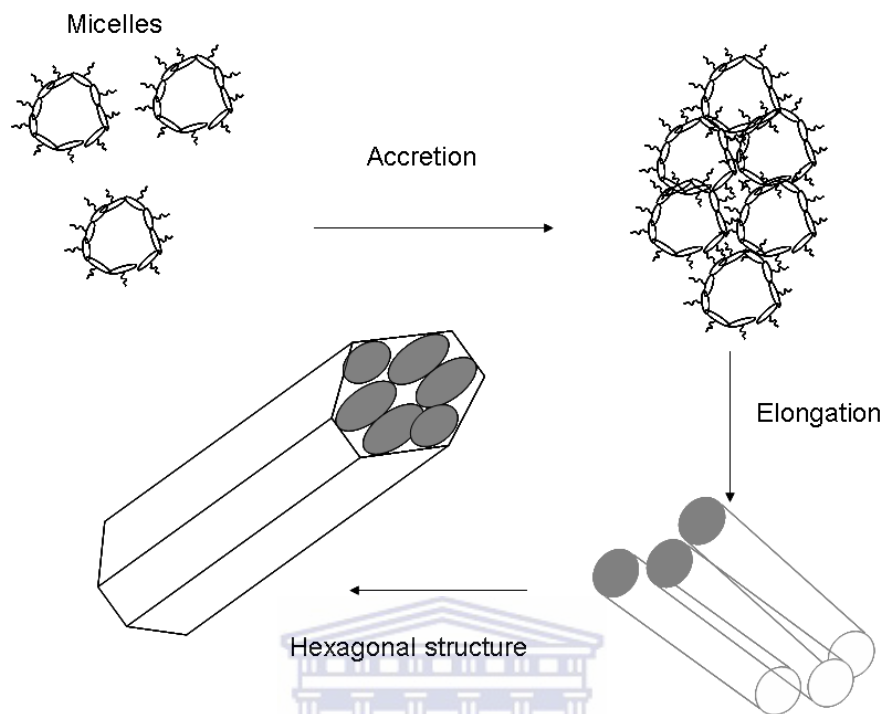


**Figure 4.3:** Schematic diagram of the formation of hexagonal nanostructures.

UNIVERSITY of the  
WESTERN CAPE

Figure 4.4 shows that the hexagonal nanostructures are made up of a cluster of spherical balls (as indicated by the arrows). As shown by the SEM images, hexagonal structures differ in size. This is attributed to the differences in the size of nanorods formed by  $\text{FeCl}_3$  and APS and the composition and number of nanorods that packed to produce the respective hexagonal structures. It is not clear at this stage what determines the degree of aggregation of the nanorods in the formation of the hexagonal structures. He *et al.* [18] reported that polyaniline nanostructures are formed by a competing process between the interfacial nucleation and the aqueous nucleation.

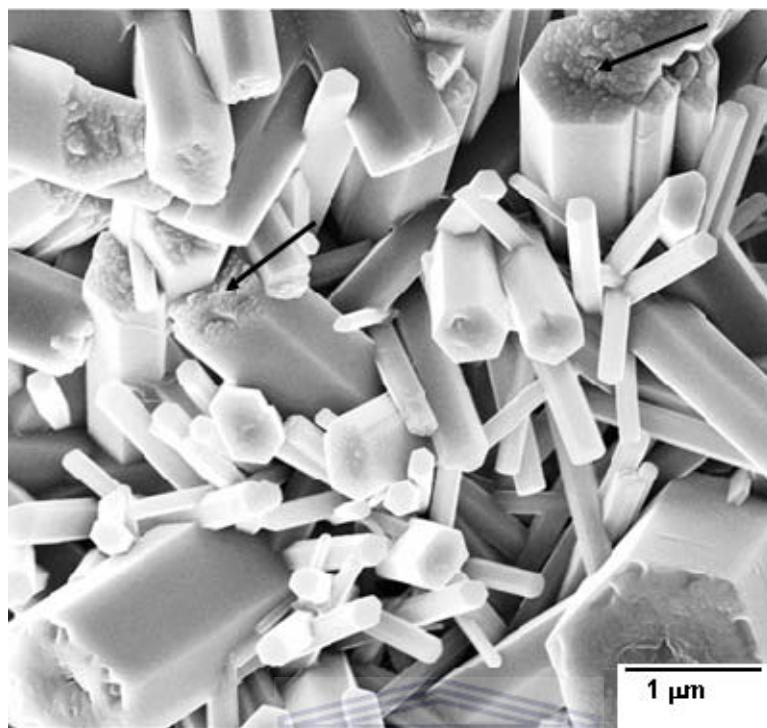


**Figure 4.4:** Field emission scanning electron micrographs of PDMA.

They showed that the polarity of the organic phase and the concentration of acetic acid influenced the concentration distribution of aniline in aqueous and organic phases, and in turn influenced the diffusion rate of aniline from organic phase to aqueous phase. They also demonstrated that the amount of APS influenced the polymerization rate both at oil–water interface and in aqueous phase. All these factors affected the relative rate of interfacial nucleation to aqueous nucleation and in turn the morphologies of the resulting polyaniline.

#### **4.3.2. FOURIER TRANSFORM INFRARED SPECTROSCOPY (FT-IR)**

The FTIR spectra of PANI compared with that of PDMA are shown in Figure 4.5. The band assignments of the FTIR absorption peaks for

polyaniline and PDMA are given in Table 4.1. The spectrum of pure PANI exhibits the characteristic bands in the 400 - 4000  $\text{cm}^{-1}$  range. The peak at 1558  $\text{cm}^{-1}$  can be attributed to the C=N and C=C stretching modes for the quinoid rings. The peaks at 1474  $\text{cm}^{-1}$  which correspond to the stretching vibration of benzoic in PANI are absent. The absence of the stretching vibration of benzoic group in PANI confirms the existence of fully oxidized PANI. The band at 1300  $\text{cm}^{-1}$  belongs to the C-N stretching of a secondary aromatic amine strengthened by protonation of PANI, and is also present in the spectra of PDMA [19, 20]. The band at 1157  $\text{cm}^{-1}$  is considered to be a measure of the degree of electron delocalization in PANI chains and thus is a characteristic peak related to PANI conductivity [21]. The FTIR spectrum of PDMA shows peaks at 1644, 1570 and 1499  $\text{cm}^{-1}$ , which are due to C=O, the stretching vibrations of quinodic (Q) and benzoic (B) groups, respectively. Both materials show peaks at 1414  $\text{cm}^{-1}$  and 1157  $\text{cm}^{-1}$  which are due to various C-N stretching vibration of QBQ, QBB, and BBQ, and N=Q=N stretching vibration, respectively. In both spectra the quinodic peaks at 1414 and 1157  $\text{cm}^{-1}$  are very sharp, suggesting the dominance of the quinodic ring structure. These FTIR results are in good agreement with those of Chandrakanthi *et al.* [19] and characteristic of PANI in its pernigraniline form.

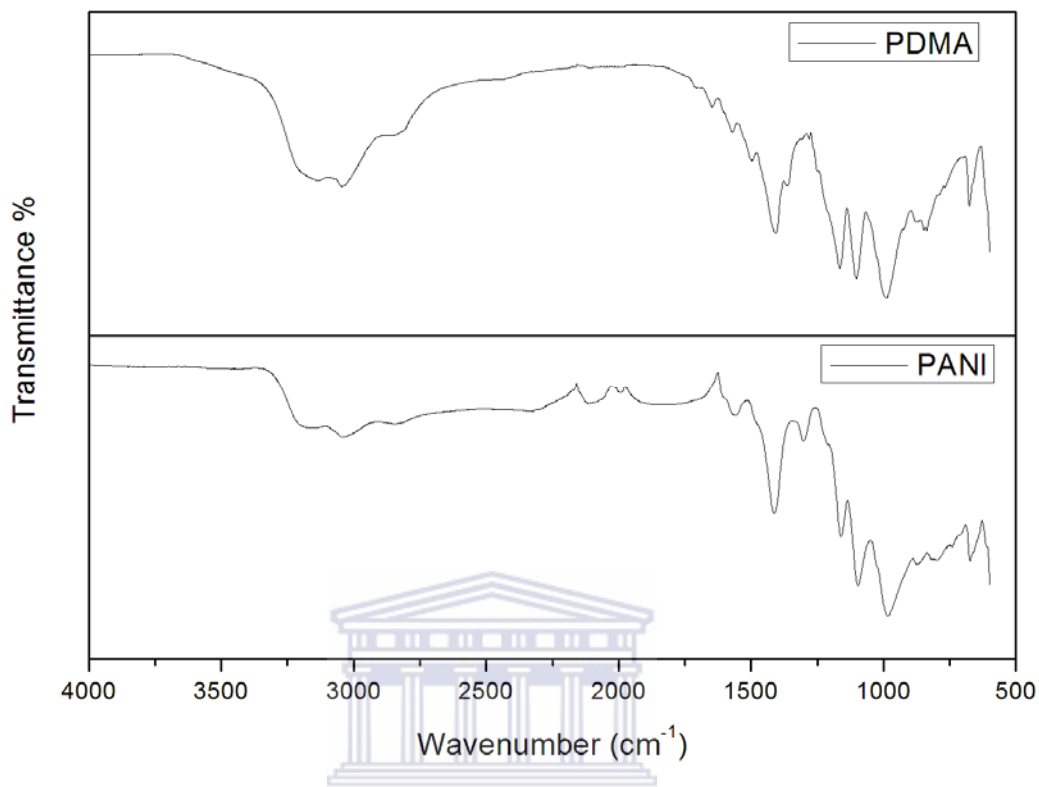


**Figure 4. 5:** FTIR spectra of PANI and PDMA.

**TABLE 4.1:** Assignments of FTIR absorption bands of PANI and PDMA.

<b>Polyaniline (wavenumber <math>\text{cm}^{-1}</math>)</b>	<b>Assignment</b>
1644	C=O
1570	C=C (B)
1499, 1558	C=C (Q)
1414	C-N stretch of QBQ QBB, and BBQ
1300	C-N stretching of secondary amines
1157	N=Q=N stretching vibration

### 4.3.3. ULTRAVIOLET VISIBLE. (UV-VIS)

The UV-Vis spectra of PANI and PDMA are shown in Figure 4.6. The UV-Vis spectra of both materials show a peak at around 360 nm and a broad peak starting from 450-650 nm. The band at around 360 nm is due to  $\pi - \pi^*$  transition of benzoic rings while the peak at around 450-650 nm is due to charge transfer excitons of quinoid structure [22, 23]. These bands are characteristics of pernigraniline form of PANI [15]. By comparing the UV-Vis spectra of polyaniline and PDMA it can be seen that the shapes of the peaks are similar, but in the PDMA the peaks for the  $\pi - \pi^*$  transitions are more enhanced and are shifted upwards. These shifts might enhance the conductivity and reactivity of the PDMA.

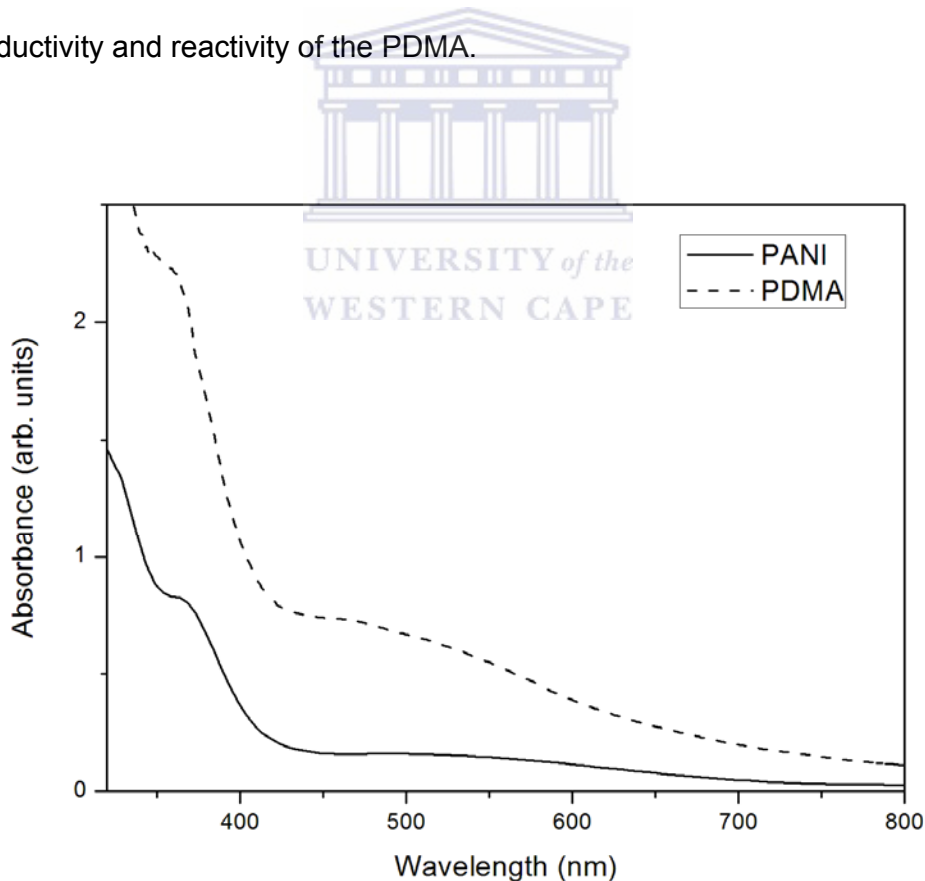


**Figure 4. 6:** UV-Vis absorption spectra of polyaniline and poly(2,5-dimethoxyaniline).

Athawale *et al.* [24] reported that the UV-visible, IR and redox characteristics of electrochemically deposited poly(2,5 dimethyl aniline) films are affected by varying the monomer concentration from 0.025 to 0.05 M in each protonic acid media. They also indicated that the intensity of the peak corresponding to the conducting phase increases with concentration while that of pernigraniline phase decreases. This could be due to the enhanced rate of reaction at higher concentration (i.e. polymerization reaction and reduction of pernigraniline to emeraldine salt phase). According to the authors [24] the optical spectra of the films deposited in different protonic acid media reveals significant differences which arise due to the variation in the basicity of the dopant anion. The basicity of the dopant anions affect the film properties in terms of its tendency to take up proton from the conjugated polymer chains. The greater the basicity the lower the onset potential for deprotonation of the polymer chain [25]. This would result in the oxidation of the polymer chain leading to the formation of pernigraniline.

#### **4.3.4. THERMO-GRAVIMETRIC ANALYSIS (TGA)**

The thermal stability of the PANI and PDMA samples was investigated by thermogravimetric analysis (TGA), as shown in Figure 4.7. The decomposition temperatures from the derivation of the TGA curves (not shown) indicate that both PANI and PDMA decompose in three weight loss steps [3]. For PANI, the initial weight loss at 50–130 °C is due to the loss of water bound molecules or moisture. The weight loss for PANI at temperatures around 300 °C, is about 10% which could be attributed to the removal of dopant anions [26]. The second weight loss at 400 °C indicates a structural

decomposition of the polymer chain. The total weight loss for PANI at 800 °C is 15%. Similar results were obtained by other authors [27, 28]. The TGA curves of PDMA show loss of moisture in the first step of decomposition, the removal of dopant anions and decomposition of the materials in the subsequent steps.

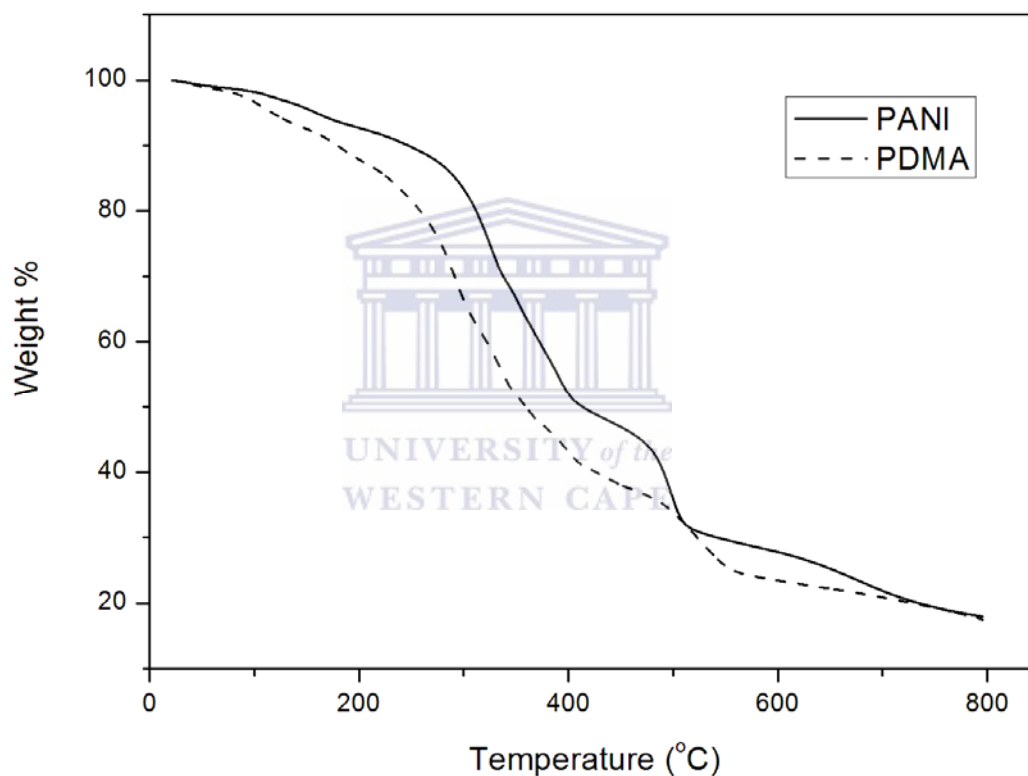


**Figure 4. 7:** Thermo-gravimetric analysis profile of PANI, PDMA in nitrogen at heating rate of 10 °C/min

The initial decomposition temperatures of PDMA in the second and third steps are lower than for pure PANI. This could be due to the presence of the methoxy group. The highest percentage weight loss is observed at



decomposition temperature between 260-400 °C, in the second decomposition step for PDMA. The percentage weight loss is about 40%. The complete decomposition of polymer backbone for both polymers took place around 500 °C.

#### 4.3.5. CYCLIC VOLTAMMETRY

Cyclic voltammograms (CV) of PANI and PDMA are shown in Figure 4.8. Both voltammograms shows one redox couple with average formal potentials,  $E^{0'}$ , values of 394 mV and 400 mV, for PANI and PDMA, respectively. Within limits of experimental error, the formal potentials were independent of scan rate and the averaged ratio of the anodic to cathodic peak currents,  $I_{p,A}/I_{p,C}$ , 0.83 and 0.82, for PANI and PDMA, respectively. The results indicate that a quasi-reversible electrochemistry of both the PANI and PDMA compounds. However, the peak separation ( $\Delta E_p = E_{p,A} - E_{p,C}$ ) values varied with scan rate (see Table 4.2) and were all more than 65 mV expected for the electrochemistry of a surface-bound species undergoing fast reversible electron transfer reaction. The paste cell system used in this study behaves in the same way as surface-bound species. Thus the large  $E_p$  values of both PANI and PDMA are indicative of the coalescing of normal multi-redox couples of polyanilines into one redox couple obtained for PANI and PDMA prepared with a combination of  $(\text{NH}_4)_2\text{S}_2\text{O}_8$ , and  $\text{FeCl}_3$  as oxidants. The  $E^{0'}$  values of both PANI and PDMA suggests that the redox couples in Fig. 4.8 are pernigraniline radical/pernigraniline [6] which is in good agreement with the results obtained by UV-Vis and FTIR spectroscopy. The voltammograms further show that the  $\Delta E_p$  and  $I_p$  values increase with an increase in the scan

rate. This is indicative that the peak current is diffusion controlled. A Randles-Sevcik analysis of the peak currents gave a charge transfer coefficient,  $D_e$ , values of  $0.93 \times 10^{-5} \text{ cm}^2/\text{s}$  and  $1.12 \times 10^{-5} \text{ cm}^2/\text{s}$  for PANI and PDMA, respectively. These  $D_e$  values show that charge transportation along the polymer chain will be more efficient in PDMA. If that is the case then the conductance of PDMA is expected to be higher than that of PANI.

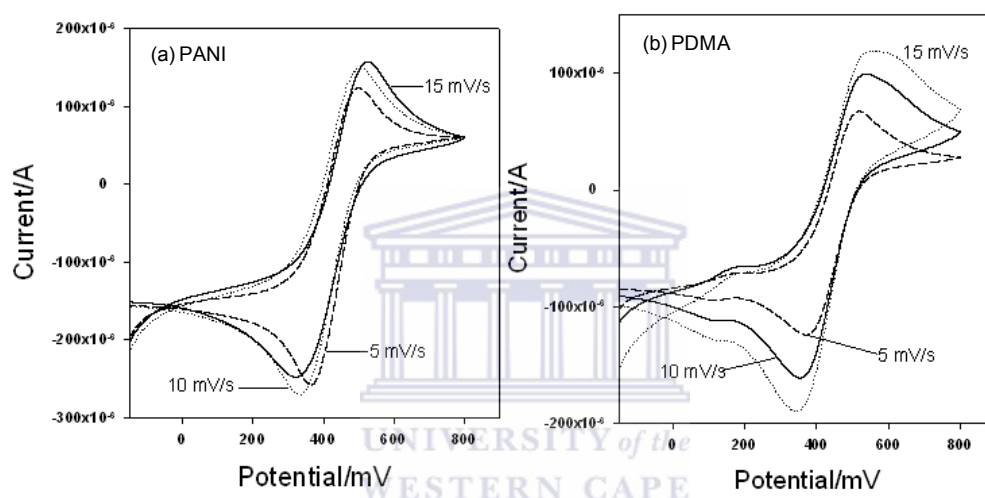


**Figure 4. 8:** Cyclic voltammograms of (a) PANI and (b) PDMA paste in 1 M HCl performed at 5, 10, 15 mV/s

**TABLE 4.2:** Electrochemical parameters of PANI and PDMA

Scan Rate mV/s	PANI			PDMA		
	$I_{p,A}/I_{p,C}$	$E_p$	$E^{0'}/mV$	$I_{p,A}/I_{p,C}$	$E_p$	$E^{0'}/mV$
5	0.3126	127	393	0.7484	174	406
10	0.6640	143	391	0.8079	215	399
15	0.8504	169	393	0.8395	253	397
20	0.8797	191	395	<u>0.8412</u>	289	396
25	0.9274	212	396	0.7962	331	400

Cyclic voltammetry was also used to calculate the conductance of different oxidation states of the materials by applying the Ohm's law relation to multiple scan rates cyclic voltammetry [6]. The following equation was used to calculate the conductance (C) of PANI and PDMA.

$$C = \frac{\Delta I_v}{\Delta E_v}, \quad (4.1)$$

where

$$I_v = I_{p(15\text{ mV/s})} - I_{p(5\text{ mV/s})} \text{ and } E_v = E_{p(15\text{ mV/s})} - E_{p(5\text{ mV/s})}$$

The conductance values of the whole material, calculated as the average of conductance of the oxidised and the reduced forms, were  $0.37 \times 10^{-3}$  S and  $2.02 \times 10^{-3}$  S for PANI and PDMA, respectively. Iwuoha *et. al.* [6] reported an averaged conductance of  $2.0 \times 10^{-2}$  S for pernigraniline radical/pernigraniline redox couple of polyaniline-polystyrene sulphonic acid

(PANI-PSSA) which is one order of magnitude greater than what is obtained in this study. The low conductance values stems from the facts that the most of the PANI chains are in the pernigraniline oxidation state. As the average oxidation level of the PANI chains decreases, more chains convert from the pernigraniline to emeraldine oxidation state increasing the conductivity. The results are in good agreement with that obtained by Dong *et al.* [30]. They reported that the conductance of PANI was maximum between pernigraniline and emeraldine states and the conductance will decrease further when PANI transforms to the leucoemeraldine state.



#### 4.4. CONCLUSION

The synthesis of polyanilines by combining the two oxidants  $(\text{NH}_4)_2\text{S}_2\text{O}_8$ , and  $\text{FeCl}_3$  give rise to polymers in the pernigraniline state that exhibit hexagonal morphologies as observed from the scanning electron microscopy analysis. The dominance of quinodic stretching vibrations detected by FTIR confirms the formation of fully oxidized form of PANI, this was also confirmed by UV-Vis absorption between 450 and 650 nm which are characteristic of pernigraniline. cyclic voltammetric analysis showed that the pernigraniline-like PANI and PDMA had average formal potentials values of 394 mV and 400 mV, respectively for PANI (conductance  $0.37 \times 10^{-3}$  S) and PDMA (conductance  $2.02 \times 10^{-3}$  S). It was found that diffusion was not the only means of transport in the cyclic voltammetry. The thermogravimetric analysis revealed an enhancement in the stability of the polymers. With an average formal potential of these hexagonal polymers being 400 mV, it means that they will be very useful as electron transfer mediators in sensor chips and photovoltaic cells. In the case of photovoltaic cells, they do not require large energy of activation. Due to their highly geometric morphology it will be possible to modify the hexagonal rod ends or sides with suitable functional groups as is currently done with carbon nanotubes.

#### 4.5. REFERENCES:

- [1]. Iijima, S., Helical microtubules of graphitic carbon. *Nature* **1991**, 354, (6348), 56-58.
- [2]. Albuquerque, J.E.; Mattoso, L.H. C.; Balogh, D.T.; Faria, R.M.; Masters, J.G.; MacDiarmid, A.G., A simple method to estimate the oxidation state of polyanilines. *Synthetic Metals* **2000**, 113, (1-2), 19-22.
- [3]. Roy, B.; Gupta, M.; Bhowmik, L.; Ray, J., Synthesis and characterization of poly(2,5-dimethoxyaniline) and poly(aniline-Co-2,5-dimethoxyaniline): The processable conducting polymers. *Bulletin of Materials Science* **2001**, 24, (4), 389-396.
- [4]. Jang, J.; Bae, J.; Lee, K., Synthesis and characterization of polyaniline nanorods as curing agent and nanofiller for epoxy matrix composite. *Polymer* **2005**, 46, (11), 3677-3684.
- [5]. Sun, Q.; Park, M.-C.; Deng, Y., Dendritic superstructure formation of polyaniline prepared using a water-soluble polyelectrolyte copolymer as the support matrix. *Materials Letters* **2007**, 61, (14-15), 3052-3055.
- [6]. Iwuoha, E.I.; Mavundla, S.E.; Somerset, V.S.; Petrik, L.F.; Klink, M.J.; Sekota, M.; Bakers, P., Electrochemical and Spectroscopic Properties of Fly Ash–Polyaniline Matrix Nanorod Composites. *Microchimica Acta* **2006**, 155, (3), 453-458.
- [7]. Bavastrello, V.; Stura, E.; Carrara, S.; Erokhin, V.; Nicolini, C., Poly(2,5-dimethylaniline)-MWNTs nanocomposite: a new material for conductometric acid vapours sensor. *Sensors and Actuators B: Chemical* **2004**, 98, (2-3), 247-253.

- [8]. Huang, J.; Kaner, R.B.; A General Chemical Route to Polyaniline Nanofibers. *Journal of American Chemical Society* **2004**, 126, (3), 851-855.
- [9]. Yin, P.; Kilmartin, P. A., Formation of poly-2,5-dimethoxyaniline on steels. *Current Applied Physics* **2004**, 4, (2-4), 141-143.
- [10]. Huang, L.-M.; Wen, T.-C.; Gopalan, A., Synthesis and characterization of soluble conducting poly(aniline-co-2, 5-dimethoxyaniline). *Materials Letters* **2003**, 57, (12), 1765-1774.
- [11]. Palys, B.; Kudelski, A.; Stankiewicz, A.; Jackowska, K., Influence of anions on formation and electroactivity of poly-2,5-dimethoxyaniline. *Synthetic Metals* **2000**, 108, (2), 111-119.
- [12]. Zhang, D.; Wang, Y., Synthesis and applications of one-dimensional nano-structured polyaniline: An overview. *Materials Science and Engineering: B* **2006**, 134, (1), 9-19.
- [13]. Zhang, Z.; Wei, Z.; Wan, M.; Nanostructures of Polyaniline Doped with Inorganic Acids. *Macromolecules* **2002**, 35, (15), 5937-5942.
- [14]. Bai, X.; Li, X.; Li, N.; Zuo, Y.; Wang, L.; Li, J.; Qiu, S., Synthesis of cluster polyaniline nanorod via a binary oxidant system. *Materials Science and Engineering: C* **2007**, 27, (4), 695-699.
- [15]. Dong, B.; He, B.-L.; Xu, C.-L.; Li, H.-L., Preparation and electrochemical characterization of polyaniline/multi-walled carbon nanotubes composites for supercapacitor. *Materials Science and Engineering: B* **2007**, 143, (1-3), 7-13.
- [16]. Li, W.; McCarthy, P. A.; Liu, D.; Huang, J.; Yang, S.-C.; Wang, H.-L., Toward Understanding and Optimizing the Template-Guided Synthesis

- of Chiral Polyaniline Nanocomposites. *Macromolecules* **2002**, 35, (27), 9975-9982.
- [17]. Kim, D.; Kim, J.-Y.; Kim, E.-R.; Sohn, D., Preparation of Polyaniline Nanoparticles by Polymer Surfactants. *Molecular crystals and liquid crystals* **2002**; 377, 345 - 348.
- [18]. He, Y.; Lu, J., Synthesis of polyaniline nanostructures with controlled morphology by a two-phase strategy. *Reactive and Functional Polymers* **2007**, 67, (5), 476-480.
- [19]. Chandrakanthi, N.; Careem, M. A., Preparation and characterization of fully oxidized form of polyaniline. *Polymer Bulletin* **2000**, 45, (2), 113-120.
- [20]. Li, G.; Zhang, Z., Synthesis of Dendritic Polyaniline Nanofibers in a Surfactant Gel. *Macromolecules* **2004**, 37, (8), 2683-2685.
- [21]. Lee, D.; Char, K.; Wook Lee, S.; Woo Park, Y., Structural changes of polyaniline/montmorillonite nanocomposites and their effects on physical properties. *Journal of Materials Chemistry* **2003**, 13, (12), 2942-2947.
- [22]. Kulkarni, M. V.; Viswanath, A. K., Comparative studies of chemically synthesized polyaniline and poly(o-toluidine) doped with p-toluene sulphonic acid. *European Polymer Journal* **2004**, 40, (2), 379-384.
- [23]. Kohut-Svelko, N.; Reynaud, S.; François, J., Synthesis and characterization of polyaniline prepared in the presence of nonionic surfactants in an aqueous dispersion. *Synthetic Metals* **2005**, 150, (2), 107-114.



- [24]. Athawale, A.A.; Deore, B.A.; Kulkarni, V.M., Spectroscopic and electrochemical properties of poly(2,5 dimethyl aniline) films. *Materials Chemistry and Physics* **1999**, 60, (3), 262-267.
- [25]. Saraswathi, R.; Kuwabata, S.; Yoneyama, H., Influence of basicity of dopant anions on the conductivity of polyaniline. *Journal of Electroanalytical Chemistry* **1992**, 335, (1-2), 223-231.
- [26]. Jeevananda, T.; Siddaramaiah; Seetharamu, S.; Saravanan, S.; D'Souza, L., Synthesis and characterization of poly (aniline-co-acrylonitrile) using organic benzoyl peroxide by inverted emulsion method. *Synthetic Metals* **2004**, 140, (2-3), 247-260.
- [27]. Al-Ahmed, A.; Mohammad, F.; Rahman, M. Z. A., Preparation, characterization, thermooxidative degradation, and stability of polyaniline/polyacrylonitrile composites in terms of direct-current electrical conductivity retention. *Journal of Applied Polymer Science* **2006**, 99, (2), 437-448.
- [28]. Bissessur, R.; MacDonald, J., Novel alkyl substituted polyanilines/VOPO<sub>4</sub> nanocomposites. *Solid State Sciences* **2006**, 8, (5), 531-536.
- [29]. Mathebe, N.G.R.; Morrin, A.; Iwuoha, E.I., Electrochemistry and scanning electron microscopy of polyaniline/peroxidase-based biosensor. *Talanta* **2004**, 64, (1), 115-120.
- [30]. Dong, B.; He, B.-L.; Xu, C.-L.; Li, H.-L., Preparation and electrochemical characterization of polyaniline/multi-walled carbon nanotubes composites for supercapacitor. *Materials Science and Engineering: B* **2007**, 143, (1-3), 7-13.

# CHAPTER FIVE

---

## PHYSICOCHEMICAL AND MORPHOLOGICAL PROPERTIES OF POLY (ANILINE-CO-PYRROLE)

### 5.1. INTRODUCTION

Electronically conducting polymers have been the subject of numerous investigations in the past two decades [1-5]. Among conducting polymers, polyaniline (PANI) and polypyrrole (PPy) are the most promising materials because of their high electrical conductivity, environmental stability, low cost of production and favourable physicochemical properties [6-8]. These properties provide favourable conditions for potential applications in light-emitting diodes, solar cells, sensors, batteries, and electrochemical supercapacitors [9]. PANI and (PPy) can be prepared by electrochemical [10-12] and chemical oxidative-polymerization methods [13-17] and can also be doped or undoped between their conducting and insulating states [18].

To date, most of the published research on electrochemical copolymerization of pyrrole and aniline or electrochemical deposition of PANI and PPy layers on different substrates has been to obtain PANI-PPy composite [19-23]. It has been reported that polyaniline-polypyrrole composite coatings on carbon fibers can be formed by using a one step electrochemical

synthesis process [21, 22]. They showed that the behaviour of the current-time ( $I - t$ ) transient could be used to understand the formation of polyaniline-polypyrrole composite coatings on carbon fibers. They also showed that the structure, yield and the morphology of the coatings were dependent on the feed ratio of the monomers (aniline and pyrrole) and the applied potential. On the other hand, Cakmak *et al.* [23] reported a two step electrochemical polymerization process to obtain conductive homopolymers, composites and copolymers of PANI, PPy and poly(dimethylsiloxane) (PDMS).

It has been reported that the molecular structure of polymer chains play a major role in the conductivity of polymers, while the effects of molecular weight and crystallinity are less pronounced [24]. The molecular structure of a conducting polymer chain can be controlled in three ways: (1) changing the degree of protonation and the sort of an acid, (2) by the chemical substitution of constitutional units in the PANI, (3) by copolymerization of aniline with suitable co-monomers. Recently, a great deal of attention has been paid to synthesize aniline-based copolymers. A possible reason is probably attributed to great difficulty to synthesize new conducting polymers with electric properties and stability better than polyaniline and polypyrrole. The copolymerization of aniline and other monomers offers a possibility to prepare a new PANI type of copolymer that not only retains the good properties of PANI itself but also possesses new properties. However, Fusalba *et al.* [25] reported that the main motivation for preparing copolymer composites lies in the possibility that these materials overcome the limitation of the rareness of new conjugated  $\pi$ -bond-containing monomers. It is believed that

copolymerization of a pair of monomers will lead to an increase in the number of conductive polymers that can be made from the same set of monomers [26]. In this article we report on the morphological evolution, optical and structural properties of poly(aniline-co-pyrrole) prepared by a chemical oxidative copolymerization process from monomer mixtures of aniline and pyrrole. The molar ratio of aniline and pyrrole monomers, in the feed were kept constant at 1:1.

## **5.2. EXPERIMENTAL DETAILS**

### **5.2.1. MATERIALS**

Aniline (99%), pyrrole (98%), 2,5-dimethoxyaniline, ammonium persulphate (APS,  $(\text{NH}_4)_2\text{S}_2\text{O}_8$ , 98%), dimethylformamide (DMF, 99%) and ferric chloride ( $\text{FeCl}_3$ ) were purchased from Sigma Aldrich. All chemicals were used as received without further purification.

### **5.2.2. SYNTHESIS OF PANI, PPy, POLY (ANILINE-CO-PYRROLE), PDMA, AND POLY (2,5 DIMETHOXYANILINE-CO-PYRROLE)**

PANI, PPy, and Poly(aniline-co-pyrrole) (PANI-PPy) were synthesized by chemical oxidation of their respective monomers. In a 50 mL flask a 0.2 mL aniline and 0.2 mL of pyrrole were dissolved in a solution of 2 mL HCl in 20 mL distilled water. The solution was stirred for 30 min at room temperature whereafter 0.48 g of APS and 0.375 g of  $\text{FeCl}_3$  was added respectively in the solution for polymerization initiation. The resultant mixture was stirred for another 3 h. The product was collected by filtration and washed with ethanol and dried at a temperature of 50 °C. The same procedure was followed for

PDMA, and poly((2,5 dimethoxyaniline-co-pyrrole) synthesis. It should be noted that a feed molar ratio of 1:1 (An:Py) was used since it was reported that by varying the ratios of aniline and pyrrole, copolymers with more PANI or PPy behave similar to those individual homopolymers of aniline or pyrrole, while the copolymers from equal molar ratios combined the characteristics of both homopolymers [9, 24, 27].

### 5.2.3. CHARACTERIZATION

Scanning electron microscopy (SEM) samples were prepared by placing some of the synthesized materials onto an aluminum stub using adhesive carbon tape. The samples were sputter-coated with gold to prevent charging effects inside the microscope. The morphology of powder samples was investigated by using JEOL 7500F high resolution field emission SEM. Ultraviolet-visible (UV-Vis) spectra were recorded on a PerkinElmer Lambda 750S spectrometer from 320 to 900 nm. Photoluminescence (PL) measurements were recorded on PerkinElmer LS 55 spectrometer by exciting the samples with a 320 nm line of deuterium lamp. The UV-Vis and PL samples were prepared by dissolving about 0.005 g of a material in 10 mL DMF. Infrared spectra were recorded using a Fourier transform infrared (FTIR) spectrometer (PerkinElmer Spectrum 100) to identify the chemical structure of PDMA respectively. A small amount of material was placed on the diamond coated detector and pressed onto the electrode for FTIR measurements. The X-ray diffraction patterns of powders were recorded on a Phillips (PANalytical) X-ray diffractometer using Cu K $\alpha$  ( $\lambda = 1.54 \text{ \AA}$ ) radiation source. The diffractogram was in terms of  $2\theta$  in the range 5–40°. Conductivity

and I-V characterization were performed on a Keithley 4200 Semiconductor Characterization System. The electrical conductivity of the powder pellets at room temperature was measured using a typical four-probe method.

## **5.3. RESULTS AND DISCUSSION**

### **5.3.1. ULTRAVIOLET VISIBLE SPECTRAL ANALYSIS**

Figure 5.1 shows the UV-Vis spectra of the chemically prepared homopolymers of PANI and PDMA and their respective copolymers. The spectral characteristics of the copolymers were found to be noticeably different from the individual homopolymers, PANI and PDMA. The UV-Vis spectrum of PANI shows absorption bands at around 340 and 600 nm. The band around 340 nm is due to  $\pi$ - $\pi^*$  transition of benzoid rings while the peak around 600 nm is attributed to the charge transfer excitons of the quinoid structure [28, 29]. When aniline is copolymerized with pyrrole, the absorption peak shifted to higher wavelengths.

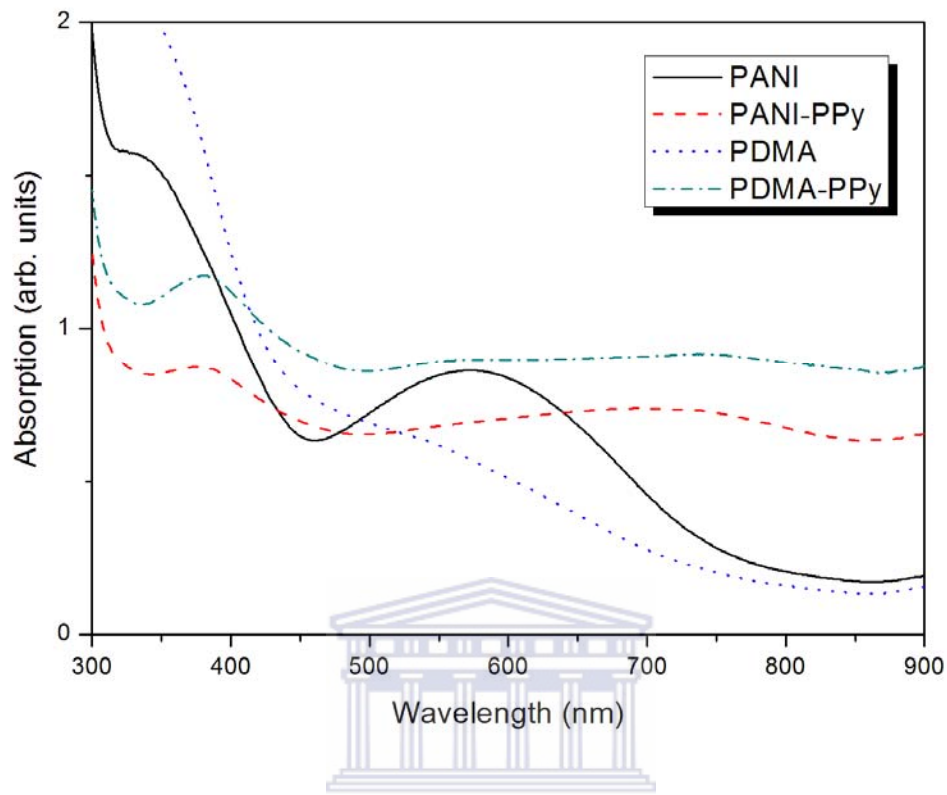


**Figure 5. 1:** UV-Vis spectra of PANI, PDMA and their copolymers.

A similar shift is observed in the UV-Vis spectra of the copolymerized poly(2,5-dimethoxy-co-pyrrole) (PDMA-PPy), (Figure 5.1). These shifts suggested that the inclusion of pyrrole in PANI and PDMA matrix reveals an increase in conjugation length for copolymers. The UV-Vis spectra of the copolymers also shows a broad band between 450-800 nm ( PANI-PPy) and 500-850 nm, indicating that it can possibly be used for electron harvest in photovoltaic applications, since the maximum absorption of the sun is at 750 nm. The coexistence of peaks around 340 nm for PANI and PDMA reveals that the polymers are having an emeraldine structure.

### 5.3.2. PHOTOLUMINESCENCE ANALYSIS

It has been reported that in most polymers the chromophore responsible for luminescence is the benzoic group and it was also found that quinodic groups are responsible for the quenching effect of photoluminescence [30]. Figure 5.2 depicts the photoluminescence spectra of the different polymer powders (PANI, PDMA, PPy and two copolymers) dissolved in DMF. The PL spectrum shows two peaks at around 390 and 420 nm. A broad peak is observed between 450 and 500 nm.

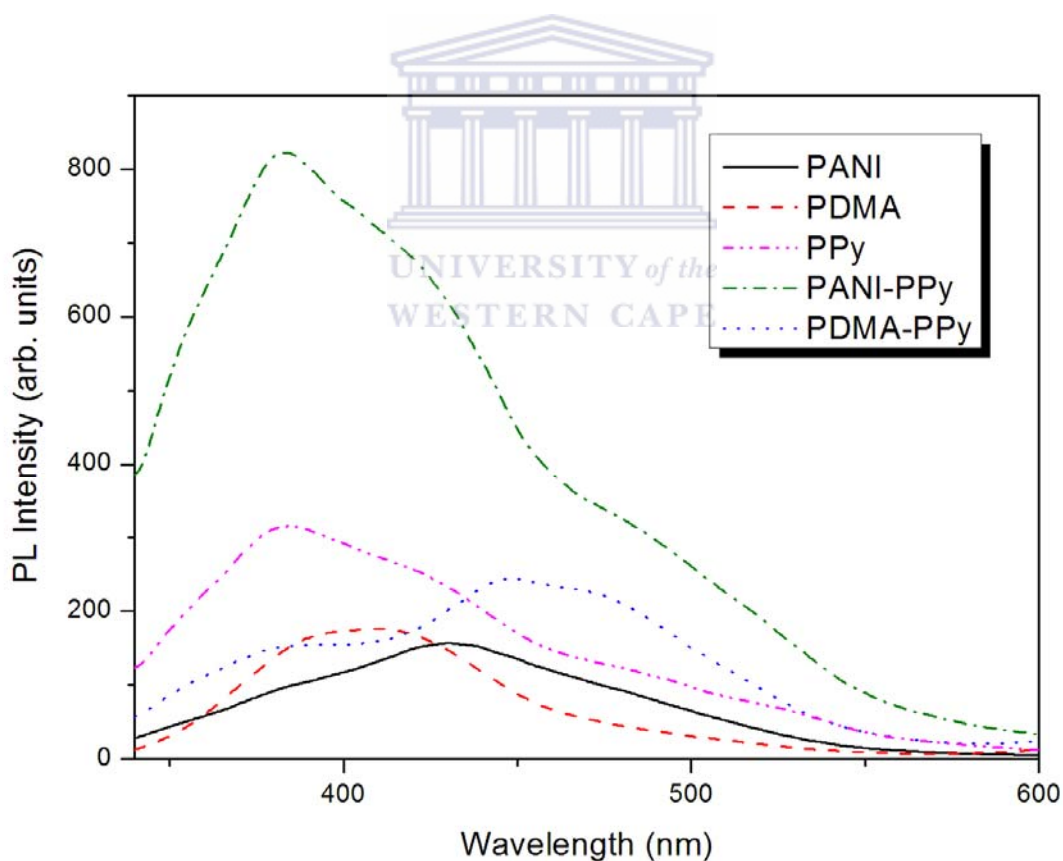
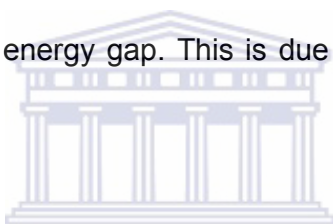


**Figure 5. 2:** Photoluminescence of PANI, PDMA and their copolymers.



The peak at ~ 390 and ~ 420 nm is attributed to the benzenoid groups causing the emission in the different polymers, whereas the broad peak at 500 nm is assigned to the protonating form or the dope state of the polymer [30, 31]. The PL spectrum confirms the semi-conducting behaviour of the different polymers because of the presence of a weak peak at ~420 nm. For a fully doped state, the peak at 420 nm disappears completely, while the peak at around 500 appears [28, 31]. Shimano *et al.* [30] demonstrated that when PANI is doped from emeraldine base to fully doped emeraldine salt, it exhibit a decrease in highest occupied molecular orbital (HOMO)/lowest un-occupied molecular orbital (LUMO) energy gap. This is due to a doping/protonation of leucoemeraldine base.



### 5.3.3. X-RAY DIFFRACTION ANALYSIS

X-ray diffraction was used to probe the structure of the homo and copolymer structures as shown in Figure 5.3. PANI shows a sharp peak at around  $2\theta = 25.4^\circ$ . Additionally peaks were also observed at  $15^\circ$  and  $20^\circ$ . This indicates that the PANI films are highly crystalline. Similar results were observed in the literature [26, 32]. The peak at  $20^\circ$  and  $25.4^\circ$  can be ascribed to the periodicity parallel and perpendicular to the polymer chains of PANI respectively [33, 34]. The peak at  $2\theta=15^\circ$  suggests the significant crystallization upon protonation [35]. The broader peaks observed around  $25^\circ$  (Fig. 5.3) for PANI-PPy copolymer and PPy are characteristic of amorphous PPy, as well as the scattering of PPy chains at the interplanar spacing [36].

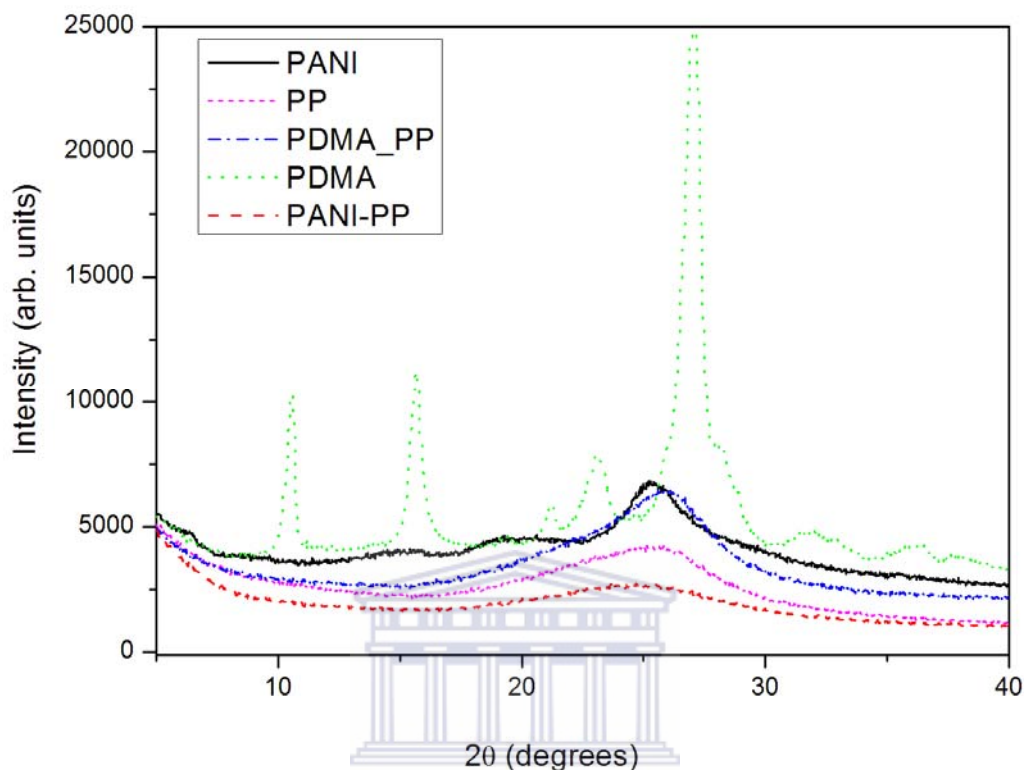


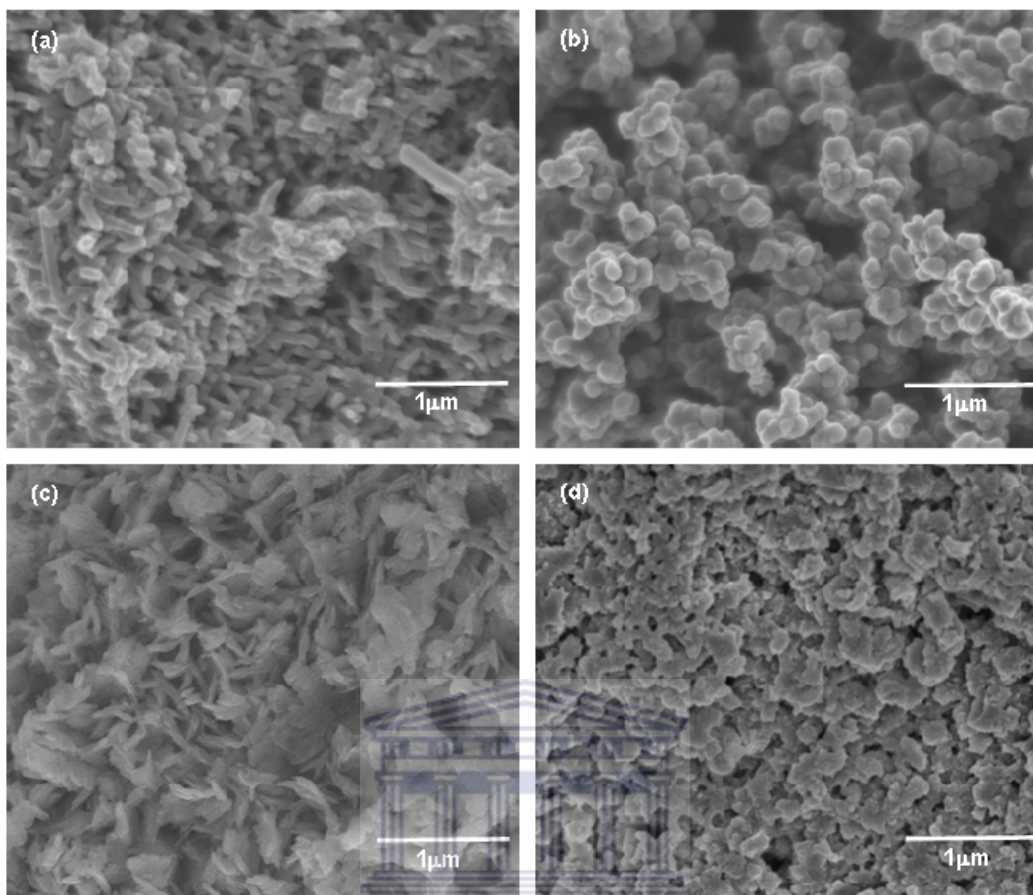
**Figure 5. 3:** X-Ray diffraction patterns of the homo and copolymers of PANI, PDMA and PPy.

Similar results were obtained by Partch *et al.* [37]. X-Ray diffraction studies show that the PDMA powders are more crystalline compare with PANI powders oxidized with two oxidants, as shown in Fig. 5.3. Very sharp peaks are observed around  $2\theta = 10^\circ, 15^\circ, 21^\circ, 23^\circ$  and  $26.4^\circ$ . Skotheim *et al.* [38] showed that by accommodating large sized dopant ions, such as  $\text{PO}_4^-$  demands greater rearrangement of bonds along the polymer backbone, can lead to better crystallinity. It has also been shown by Zhang *et al.* [39] that the graphite-like diffraction peak at around  $25^\circ$  is common to all the samples and is characteristic of the extent of pi conjugation in PANI. The broad peak at  $2\theta$

= 18°-30° in the copolymers are indicative of an amorphous behaviour. In both PDMA-PPy and PANI-PPy copolymer a complex behaviour are observed due to the broadness of the peaks. This behaviour is also observed from the SEM micrographs in Fig. 5.4.

#### 5.3.4. SCANNING ELECTRON MICROSCOPY ANALYSIS

SEM morphology of the homopolymers of PANI and PDMA and copolymers of PANI-PPy and PDMA-PPy are shown in Figure 5.4. The micrograph in Figure 4(a) shows either a “rod-like” or a fibrillar structure. It is known that a fibrillar growth is intrinsic to PANI. During the copolymerization process the poly(aniline-co-pyrrole) PANI-PPy SEM image (Figure 5.4(b)) showed that spherical structures formed by agglomerated particles. The size of the spherical structures varies between 10 and 50 nm in diameter of uniform shape. A flaky structure is observed for the PDMA (Fig. 5.4(c)). It can be seen that the pyrrole and dimethoxy aniline monomer in the feed affected the morphology of the obtained copolymer, Figure 5.4(d). The copolymer obtained shows a more compact surface of spherical agglomerates as seen in Fig. 5.4(d). It is known that the  $\pi^*$  interactions between the pyrrole main chain is very strong. Therefore it has a tendency to aggregate into the irregular morphology, which is commonly observed in the poly pyrrole obtained by the chemical oxidation polymerization [40]. Liu *et al.* [6] showed that the morphology of polypyrrole is dependent on the reaction time. They showed that granules formed during the initial stages of polymerization which then turned into short and straight fibers after 6.5 h of polymerization.



UNIVERSITY of the  
WESTERN CAPE

**Figure 5. 4:** SEM micrographs of (a) polyaniline, (b), PANI-PPy, (c) PDMA and (d) PDMA-PPy.

### 5.3.5. FOURIER TRANSFORM INFRARED SPECTROSCOPY (FT-IR)

The structure of the different polymers (polyaniline, polypyrrole and poly(aniline-co-pyrrole)) was further studied by FTIR spectroscopy as shown in Figure 5.5. It is apparent in Figure 5.5 that, PANI, PDMA and PPy show their characteristic peaks of their homopolymers. The bands at 1530 and 1441  $\text{cm}^{-1}$  in the PPy spectrum are due to C=C and C-C stretching vibrations in the polypyrrole ring structure, respectively [7]. C-N is represented by the band at 1280  $\text{cm}^{-1}$  while C-H and N-H in-plane deformation vibration are

situated at 1130 and 1000  $\text{cm}^{-1}$  [7, 8]. The strong bands in the region 900-1800  $\text{cm}^{-1}$  indicates that the conductive form of PPy is formed [41].

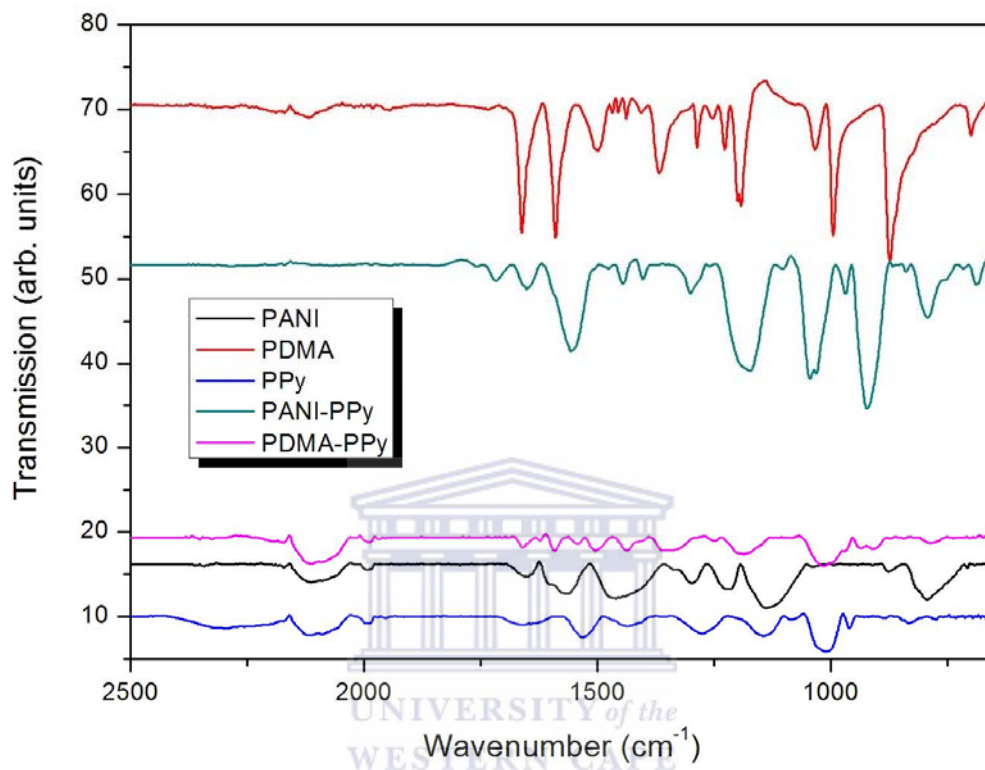


**Figure 5. 5:** FT-IR spectra of PANI, PANI-PP and PPY polymers.

The spectrum of PANI show bands at 1560 and 1480  $\text{cm}^{-1}$  which are attributed to the C=C stretching frequencies of quinodic and benzoic ring respectively [28]. The bands at 1287 and 1239  $\text{cm}^{-1}$  are due to several stretching forms of C-N bonds. PDMA spectrum shows peaks at 1660, 1540 and 1500  $\text{cm}^{-1}$ , which are due to C=O, the stretching vibrations of quinodic and benzoic groups, respectively. The peaks at 1363, 1283 and 1195  $\text{cm}^{-1}$  are due to various C-N stretching vibrations. It is observed that the peaks shifted to a lower wavenumbers for the copolymer (poly(aniline-co-pyrrole))

demonstrating the presence of neighbouring aniline and pyrrole constitutional units.

### 5.3.6. I-V MEASUREMENTS

The electrical conductivity measurements of chemically synthesized copolymers and homopolymers were performed on powder pellets by applying a DC voltage sweep from -5 to 5 V and are presented in Figure 5.6 and Table 5.1. As shown in Figure 5.6, the current–voltage characteristics of the copolymers are ohmic at room temperature. Current – voltage characteristics of the homopolymers show a non-linear (non-ohmic) behaviour. This behaviour can be explained by conduction mechanism of polyaniline and polypyrrole. In intrinsic semiconductors the charge conduction is only carried out by free electrons carriers but, in these polymers the formation of polarons and bipolarons also take part in charge conduction [42].

When the applied voltage is increased the formation of polarons and bipolarons also increases resulting in the higher current values through the sample. It can also be noted that during forward bias the PDMA-PPY has the highest current followed by PANI-PPy, PANI and then PPy.

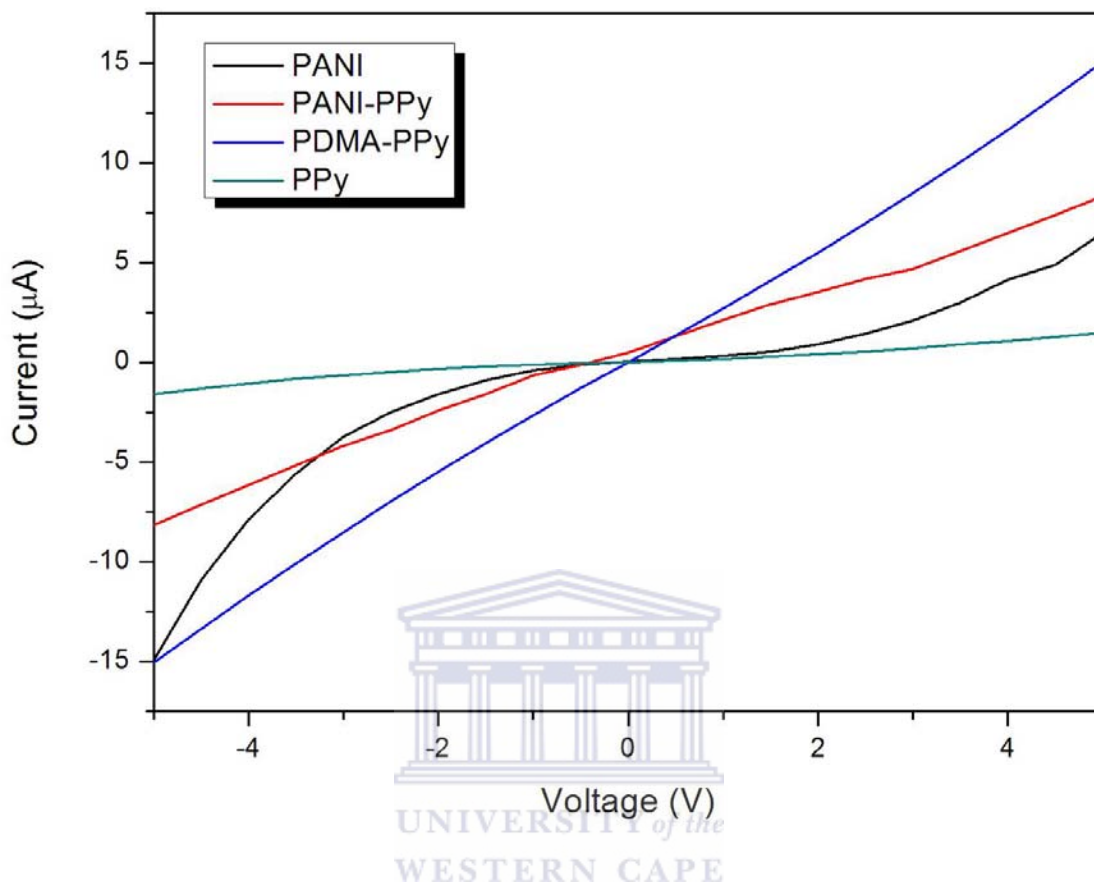


**Figure 5. 6:** I-V curves of PANI, PDMA-PPy, PANI-PPy and PPy.

**Table 5.1:** Conductivity of the different polymers

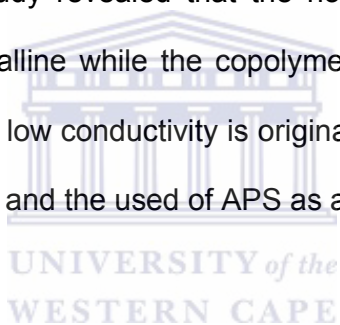
Sample	Conductivity (S/cm <sup>2</sup> )
PANI	$4.1 \times 10^{-2}$
PANI-PPy	$2.5 \times 10^{-5}$
PDMA-PPy	$5.2 \times 10^{-4}$
PPy	$4.8 \times 10^{-6}$

The conductivity of the samples relies on two aspects: microscopic and macroscopic conductivity. The former depends on the doping level, conjugation length, and chain length, etc., whereas the macroscopic conductivity is related to some external factors such as the compactness of the samples [43]. It is observed that the conductivity decreases from  $10^{-2}$  to  $10^{-5}$  when aniline is polymerized with pyrrole (Table 5.1). The lowering of the conductivity may be related to the formation of the complex between PANI and PPy, which could reduce the conjugation or chain length of the composites. It is also suggested that based on the results of SEM observation, one can find that the copolymers (Figure 5.4(a), (c), (d)) show poor ability to form good composites due to weak interactions at the interface between PANI and PPy. When APS has been used as the oxidant, the conductivity of PANI reported in the literature is generally higher than that of PPy [44, 45], as in the present case. However, if similar experiments are carried out with iron(III) salts, the situation is reversed; conductivities over  $200 \text{ S cm}^{-1}$  have recently been reported for PPy [46], typical values being in the range of tens of  $\text{S cm}^{-1}$  [47-49]. The conductivity of the PMDA-PPy copolymer is higher than that of PANI-PPy copolymer and is due to the compactness of the sample as shown by the SEM analysis. Therefore, we conclude that the lowering of the conductivity on the copolymers of PANI-PPy is due to the APS, when it is used as the oxidant, which hinder the carrier transport between different molecular chains of PANI and PPy [50].



## 5.4. CONCLUSION

Aniline and pyrrole copolymers were successfully synthesized using a conventional chemical oxidative polymerization process. The polymer displayed a strong optical absorption in the visible region and exhibited photoluminescence as determined by UV–Vis and fluorescence spectrum analysis. The SEM images showed the micro fiber and flaky morphology for PANI and PDM, respectively. Otherwise, the SEM results showed that the formed copolymer of poly(aniline-co-pyrrole) is spherical with diameters in the micro dimensions. An irregular structure is observed for the copolymer of PDMA-PPy. The XRD study revealed that the homopolymers of PANI and PDMA powders are crystalline while the copolymer of PANI and PDMA are amorphous in nature. The low conductivity is originated from the unsuccessful complex of PANI and PPy and the used of APS as an oxidant.



## 5.5. REFERENCES:

- [1]. Nalwa H.S., **1997**. Handbook of Organic Conductive Molecules and Polymers, Conductive Polymers: Transport, Photophysics and Applications. *New York: John Wiley & Sons*.
- [2]. Skotheim T.; Pomerantz M.; Elsenbaumer R.L.; Reynolds J.R., **1998**. Handbook of Conducting Polymers. 2<sup>nd</sup> edition.: *Marcel Dekker, New York*.
- [3]. Novak, P.; Muller, K.; Santhanam, K.S.V.; Haas, O., Electrochemically Active Polymers for Rechargeable Batteries. *Chemical Reviews* **1997**, 97, (1), 207-282.
- [4]. Miller, J.S., Conducting polymers-materials of commerce. *Advanced Materials* **1993**, 5, (7-8), 587-589.
- [5]. Miller, J.S., Conducting polymers-materials of commerce. *Advanced Materials* **1993**, 5, (9), 671-676.
- [6]. Liu, J.; Wan, M., Studies on formation mechanism of polypyrrole microtubule synthesized by template-free method. *Journal of Polymer Science Part A: Polymer Chemistry* **2001**, 39, (7), 997-1004.
- [7]. Saravanan, C.; Shekhar, R.C.; Palaniappan, S., Synthesis of Polypyrrole Using Benzoyl Peroxide as a Novel Oxidizing Agent. *Macromolecular Chemistry and Physics* **2006**, 207, (3), 342-348.
- [8]. Vishnuvardhan, T.; Kulkarni, V.; Basavaraja, C.; Raghavendra, S., Synthesis, characterization and a.c. conductivity of polypyrrole composites. *Bulletin of Materials Science* **2006**, 29, (1), 77-83.
- [9]. Xu, P.; Han, X.; Wang, C.; Zhang, B.; Wang, X.; Wang, H.-L., Facile Synthesis of Polyaniline-Polypyrrole Nanofibers for Application in

- Chemical Deposition of Metal Nanoparticles. *Macromolecular Rapid Communications* **2008**, 29, (16), 1392-1397.
- [10]. Diaz, A.F.; Kanazawa, K.K.; Gardini, G.P., Electrochemical polymerization of pyrrole. *Journal of the Chemical Society, Chemical Communications* **1979**, (14), 635-636.
- [11]. Diaz, A.F.; Bargon J.; Skotheim, T.A., **1986**. Handbook of Conducting Polymers. : *Marcel Dekker, New York*.
- [12]. Ouyang, J.; Li, Y., Great improvement of polypyrrole films prepared electrochemically from aqueous solutions by adding nonaphenol polyethyleneoxy (10) ether. *Polymer* **1997**, 38, (15), 3997-3999.
- [13]. Ouyang, J.; Li, Y., Great improvement of polypyrrole films prepared electrochemically from aqueous solutions by adding nonaphenol polyethyleneoxy (10) ether. *Polymer* **1997**, 38, (15), 3997-3999.
- [14]. Armes, S.P., Optimum reaction conditions for the polymerization of pyrrole by iron(III) chloride in aqueous solution. *Synthetic Metals* **1987**, 20, (3), 365-371.
- [15]. Kang, H.C.; Geckeler, K.E., Enhanced electrical conductivity of polypyrrole prepared by chemical oxidative polymerization: effect of the preparation technique and polymer additive. *Polymer* **2000**, 41, (18), 6931-6934.
- [16]. Calvo, P.A.; Rodriguez, J.; Grande, H.; Mecerreyes, D.; Pomposo, J. A., Chemical oxidative polymerization of pyrrole in the presence of m-hydroxybenzoic acid- and m-hydroxycinnamic acid-related compounds. *Synthetic Metals* **2002**, 126, (1), 111-116.

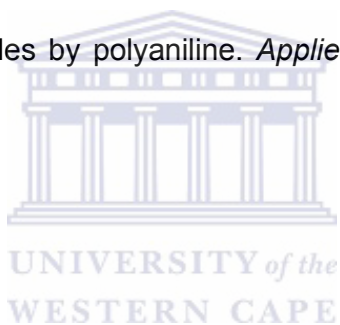
- [17]. Chakrabarti, S.; Banerjee, D.; Bhattacharyya, R., Enhancement of Room Temperature Electrical Conductivity of Polypyrrole by Chemical Modification. *The Journal of Physical Chemistry B* **2002**, 106, (12), 3061-3064.
- [18]. Kilmartin, P.A.; Wright, G A., Photoeffects to characterise polypyrrole electrodes and bilayers with polyaniline. *Electrochimica Acta* **2001**, 46, (18), 2787-2794.
- [19]. Sarl, B.; Talu, M., Electrochemical copolymerization of pyrrole and aniline. *Synthetic Metals* **1998**, 94, (2), 221-227.
- [20]. Akundy, G. S.; Rajagopalan, R.; Iroh, J. O., Electrochemical deposition of polyaniline–polypyrrole composite coatings on aluminum. *Journal of Applied Polymer Science* **2002**, 83, (9), 1970-1977.
- [21]. Rajagopalan, R.; Iroh, J.O., A one-step electrochemical synthesis of polyaniline-polypyrrole composite coatings on carbon fibers. *Electrochimica Acta* **2002**, 47, (12), 1847-1855.
- [22]. Rajagopalan, R.; Iroh, J.O., Characterization of polyaniline-polypyrrole composite coatings on low carbon steel: a XPS and infrared spectroscopy study. *Applied Surface Science* **2003**, 218, (1-4), 58-69.
- [23]. Cakmak, G.; Küçükyavuz, Z.; Küçükyavuz, S., Conductive copolymers of polyaniline, polypyrrole and poly(dimethylsiloxane). *Synthetic Metals* **2005**, 151, (1), 10-18.
- [24]. Stejskal, J.; Trchová, M.; Ananieva, I.A.; Janca, J.; Prokes, J.; Fedorova, S.; Sapurina, I., Poly(aniline-co-pyrrole): powders, films, and colloids. Thermophoretic mobility of colloidal particles. *Synthetic Metals* **2004**, 146, (1), 29-36.

- [25]. Fusalba, F.; Belanger, D., Electropolymerization of Polypyrrole and Polyaniline-Polypyrrole from Organic Acidic Medium. *The Journal of Physical Chemistry B* **1999**, 103, (42), 9044-9054.
- [26]. Lim, V.W.L.; Kang, E.T.; Neoh, K.G.; Ma, Z.H.; Tan, K.L., Determination of pyrrole-aniline copolymer compositions by X-ray photoelectron spectroscopy. *Applied Surface Science* **2001**, 181, (3-4), 317-326.
- [27]. Xu, P.; Han, X.; Wang, C.; Zhang, B.; Wang, X.; Wang, H.-L., Facile Synthesis of Polyaniline-Polypyrrole Nanofibers for Application in Chemical Deposition of Metal Nanoparticles. *Macromolecular Rapid Communications* **2008**, 29, (16), 1392-1397.
- [28]. Mavundla, S.E.; Malgas, G.F.; Baker, P.; Iwuoha, E.I., Synthesis and Characterization of Novel Nanophase Hexagonal Poly(2,5-dimethoxyaniline). *Electroanalysis* **2008**, 20, (21), 2347-2353.
- [29]. Iwuoha E.I, Mavundla S.E, Somers V.S, Petrik L.F, Klink M.J, Sekota M, Baker P., Electrochemical and Spectroscopic Properties of Fly Ash-Polyaniline Matrix Nanorod Composites. *Microchimica Acta* **2006**, 155:453.
- [30]. Shimano, J.Y.; MacDiarmid, A.G., Polyaniline, a dynamic block copolymer: key to attaining its intrinsic conductivity? *Synthetic Metals* **2001**, 123, (2), 251-262.
- [31]. Verma, D.; Dutta, V., Role of novel microstructure of polyaniline-CSA thin film in ammonia sensing at room temperature. *Sensors and Actuators B: Chemical* **2008**, 134, (2), 373-376.

- [32]. Rahy, A.; Yang, D.J., Synthesis of highly conductive polyaniline nanofibers. *Materials Letters* **2008**, 62, (28), 4311-4314.
- [33]. Wang, J.; Wang, J.; Yang, Z.; Wang, Z.; Zhang, F.; Wang, S., A novel strategy for the synthesis of polyaniline nanostructures with controlled morphology. *Reactive and Functional Polymers* **2008**, 68, (10), 1435-1440.
- [34]. Zhang, Z.; Wan, M.; Wei, Y., Highly Crystalline Polyaniline Nanostructures Doped with Dicarboxylic Acids. *Advanced Functional Materials* **2006**, 16, (8), 1100-1104.
- [35]. Amarnath, C.A.; Palaniappan, S., Polyaniline doped by a new class of dopants, benzoic acid and substituted benzoic acid: synthesis and characterization. *Polymers for Advanced Technologies* **2005**, 16, (5), 420-424.
- [36]. Babu, K.F.; Senthilkumar, R.; Noel, M.; Kulandainathan, M.A., Polypyrrole microstructure deposited by chemical and electrochemical methods on cotton fabrics. *Synthetic Metals* **2009**, 159, (13), 1353-1358.
- [37]. Partch, R.; Gangolli, S.G.; Matijevic, E.; Cal, W.; Araj, S., Conducting polymer composites: I. Surface-induced polymerization of pyrrole on iron(III) and cerium(IV) oxide particles. *Journal of Colloid and Interface Science* **1991**, 144, (1), 27-35.
- [38]. Skotheim, T.A.; Elsenbaumer, R.L.; Reynolds, J.R., **1998**. Handbook of conducting polymers. *M. Dekker*.

- [39]. Zhang, X.; Zhang, J.; Liu, Z., Tubular composite of doped polyaniline with multi-walled carbon nanotubes. *Applied Physics A: Materials Science & Processing* **2005**, 80, (8), 1813-1817.
- [40]. Mansouri, J.; Burford, R.P., Novel membranes from conducting polymers. *Journal of Membrane Science* **1994**, 87, (1-2), 23-34.
- [41]. Wong, P.H.; Dave, C.B.; Leroux, F.; Harreld, J.; Dunn, B.; Nazar, F.L., Synthesis and characterization of polypyrrole/vanadium pentoxide nanocomposite aerogels. *Journal of Materials Chemistry* **1998**, 8, (4), 1019-1027.
- [42]. Patidar, D.; Jain, N.; Saxena, N.S.; Sharma, K.; Sharma, T.P., Electrical properties of CdS/polyaniline heterojunction. *Brazilian Journal of Physics* **2006**, 36, (4A), 1210-1212 .
- [43]. Chen, A.; Wang, H.; Zhao, B.; Li, X., The preparation of polypyrrole-Fe<sub>3</sub>O<sub>4</sub> nanocomposites by the use of common ion effect. *Synthetic Metals* **2003**, 139, (2), 411-415.
- [44]. Rodriguez, J.; Grande, H-J.; T. Otero, F., Edited by H. Nalwa, S.; Handbook of organic conductive molecules and polymers. *John Wiley & Sons Ltd., Chichester* **1997**, 2,. 415-68.
- [45]. Trivedi, D.C., **1997**. Polyanilines. In: Nalwa H.S., editor. Handbook of organic conductive molecules and polymers. : *Wiley, Chichester*.
- [46]. Carrasco, P. M.; Grande, H. J.; Cortazar, M.; Alberdi, J. M.; Areizaga, J.; Pomposo, J. A., Structure-conductivity relationships in chemical polypyrroles of low, medium and high conductivity. *Synthetic Metals* **2006**, 156, (5-6), 420-425.

- [47]. Planche, M.F.; Thiéblemont, J.C.; Mazars, N.; Bidan, G., Kinetic study of pyrrole polymerization with iron (III) chloride in water. *Journal of Applied Polymer Science* **1994**, 52, (13), 1867-1877.
- [48]. Kudoh, Y., Properties of polypyrrole prepared by chemical polymerization using aqueous solution containing  $\text{Fe}_2(\text{SO}_4)_3$  and anionic surfactant. *Synthetic Metals* **1996**, 79, (1), 17-22.
- [49]. Omastová, M.; Pionteck, J.; Trchová, M., Properties and morphology of polypyrrole containing a surfactant. *Synthetic Metals* **2003**, 135-136, 437-438.
- [50]. Li, X.; Chen, W.; Bian, C.; He, J.; Xu, N.; Xue, G., Surface modification of  $\text{TiO}_2$  nanoparticles by polyaniline. *Applied Surface Science* **2003**, 217, (1-4), 16-22.





# CHAPTER SIX

---

## STRUCTURAL MODULATION OF POLYANILINE AND ZINC OXIDE NANOSYSTEMS FOR APPLICATION IN SOLAR CELL DEVICES

### 6.1. INTRODUCTION

In recent years, the development of metal-polymer or metal oxide-polymer hybrid materials on nanometer scale have been receiving significant attention due to a wide range of potential applications in optoelectronic devices and in field effect transistors [1, 2]. It has also been shown that ultra-fast photo induced charge transfer can also occur between a conjugated polymer and a metal oxide semiconductor such as TiO<sub>2</sub>, ZnO, or SnO<sub>2</sub> [3]. One of the advantages of hybrid solar cells is that inorganic materials have high electron mobility and high physical and chemical stability relative to that of organic materials [4].

Among metal oxides, ZnO is most studied owing to its possible application in solar cells, chemical sensors, photocatalysis, optoelectronics, and field emission [5-11]. The large exciton binding energy (60 meV) of ZnO has made it the suitable candidate for the exciton-related device applications compared to other wide band gap materials (e.g. ZnSe, GaN, SnO<sub>2</sub>, and ZnS)

[12]. The designing of ZnO nanostructures with different morphologies and sizes is of significant importance from the standpoint of both basic fundamental research and the development of novel devices [13]. It is well known that ZnO exhibits the richest range of morphologies among the wide band gap semiconductors. Zinc oxide nanostructures such as wires, rods and tubes, and two-dimensional structures including sheets and ribbons have been synthesized [14, 15]. Among various morphologies of ZnO one-dimensional morphology is the most studied because of its possible application in solar cells.

One-dimensional nanostructures of ZnO (e.g. nanorods, nanowires and nanotubes) have been used in solar cells device to improve the electron transport by providing a direct conduction pathway for the rapid collection of photo-generated, however most of these 1D-nanostructured ZnO-based in solar cells have a low current density due to small photo-anode surface area with low dye loading so that they exhibit low light harvesting [16]. Recently Jian *et al.* [17] used flower-like structured ZnO materials on solar cells to improve the efficiency; the efficiency was improved by 90% compared with one-dimensional structures. Nanoflower morphology with random branches offers good electron transport, higher internal surface area and higher dye loading for dye solar cells [18]. Polyaniline (PANI) is the most promising polymer among polymers because of its high conductivity, environmental stability and the ease to prepare [19-22]. Polyaniline has been used as a hole injecting layer in Organic Light Emitting Diodes and it can also act as a barrier to oxygen and as a planarizing layer to inhibit electrical shorts and improve device lifetime, resulting in an improvement of the brightness and the

efficiency of the Organic Light Emitting Diodes [4]. The incorporation of one-dimensional structure polyaniline as an interfacial layer in organic photovoltaics has been found to increase the power conventional efficiency by 26% [23]. Rahy *et al.* [8] reported the new synthesis method of highly conductive polyaniline using potassium biiodate ( $\text{KH}(\text{IO}_3)_2$ ). The advantage of using potassium biiodate is that it is more stable than APS and the PANI produced is more conductive. In this work we synthesize and characterize PANI nanoworm and ZnO nanoflowers and apply them in solar cell devices.

## 6.2. EXPERIMENTAL

### 6.2.1. MATERIALS

Aniline, zinc nitrate, sodium hydroxide (NaOH), potassium biiodate ( $\text{KH}(\text{IO}_3)_2$ ), 1-methyl-2 pyrrolidinone (NMP), ammonium peroxydisulfate (APS), hydrochloric acid (HCl) Indium tin oxide (ITO) coated on a 1 mm glass substrate with a sheet resistance of  $8\text{-}12 \ \Omega/\text{sq}^{-1}$ , poly(3,4-ethylenedioxythiophene):poly(styrenesulfonate) (PEDOT:PSS) were purchased from Sigma-Aldrich. All chemicals were used as received without further purification.

### 6.2.2. SYNTHESIS OF ZINC OXIDE

Zinc oxide nanostructures were prepared by dissolving 15.60 g Zinc nitrate in 50 mL of deionised water. 4 g of NaOH was added with continuous stirring to make a colloidal solution. The resulting solution was then transferred to a 100 mL Teflon liner and put in a vessel. The solution was treated at 180 °C for 20 min under temperature controlled mode. The reaction

was then terminated and cooled at room temperature and the product was dried at 80 °C.

### **6.2.3. SYNTHESIS OF PANI AND IN-SITU SYNTHESIS OF PANI- ZnO COMPOSITES**

Polyaniline was synthesized by dissolving 1 mol of aniline in 100 mL of 1 M HCl at room temperature and stirred for 15 min. Potassium biiodate ( $\text{KH}(\text{IO}_3)_2$ ) (0.0013 mol) was then added to the reaction and stirred continuously for 1 h. The solution was left at room temperature for 12 h. The product was collected by filtration and washed with deionised water and dried in the oven at 80 °C. The PANI-ZnO composites were prepared by *in-situ* polymerizing aniline in the presence of ZnO. Aniline was dissolved in 100 mL of 1 M HCl at room temperature and subsequently (0, 1, and 2 g) ZnO synthesized by microwave was also added in the solution and stirred for 15 min. The same procedure as above was followed.

### **6.2.4 FABRICATION OF DEVICES**

The ITO glass substrate was cleaned with methanol. Poly(3,4-ethylenedioxythiophene) poly(styrenesulfonate) (PEDOT:PSS) was spin coated on the cleaned ITO glass and dried on the hot plate at 100 °C for 20 min. The donor (PANI) was spin coated on the PEDOT:PSS/ITO substrate and dried at 100 °C for 30 min. The acceptor layer (ZnO) was spin coated onto the PANI/PEDOT/ITO substrate and also dried at 100 °C for 1 h. On the other glass about 200 nm of the aluminum film deposited. This Al/Glass was

placed on top of ZnO/PANI/PEDOT:PSS/ITO layer and laminated together by pressing the substrates against each other and adding a small amount of adhesive to seal.

### **6. 2.5. CHARACTERIZATION**

Microwave synthesis was performed on a Perkin Elmer/Anton Paar Multiwave 3000. The scanning electron microscopy (SEM) samples were prepared by placing some of the synthesized material onto an aluminum stub. A carbon sticky tape was placed on the aluminum stub for adhesion of the material. The samples were sputter-coated with a thin layer of carbon to prevent charging effects inside the microscope. The morphology of the prepared materials was examined using a Neon 40 (Zeiss) FIB-SEM operated at 2 kV. Ultraviolet-visible (UV-Vis) spectra were recorded on a PerkinElmer Lambda 750S spectrometer from 320 to 900 nm. The UV-Vis samples were prepared by dissolving a small amount of material in NMP. The Raman spectroscopy measurements were conducted at room temperature with a 514 nm excitation laser Raman spectroscopy using a Horiba Jobin Yvon HR800 micro-Raman spectrometer. The X-ray diffraction patterns of powders were recorded on a Phillips (PANalytical) X-ray diffractometer using Cu K $\alpha$  ( $\lambda = 1.54 \text{ \AA}$ ) radiation source. The diffractogram was in terms of  $2\theta$  in the range 5–40°. The current-voltage (I–V) measurements were performed using a Keithly 4200 Semiconductor Characterization System. The electrical conductivity of the pellets was measured at room temperature using a four-probe method.

## 6.3. RESULTS

### 6.3.1. SCANNING ELECTRON MICROSCOPY AND TRANSMITTANCE ELECTRON MICROSCOPY

Transmittance electron microscopy images of individual flower-like and worm-like morphologies of PANI were put along their respective SEM for easy comparison. Figure 6.1(a) and (b) present the SEM and TEM image of ZnO with flower-like morphology respectively. From the SEM image (Figure 6.1(a)) it can be seen that the flower-like morphology of ZnO has petals and plates which are positioned vertical to resemble flower-like morphology. The plates were 30-50nm thick and about 230 nm in length. The petals had a diameter of 300-400 nm with thickness ranging from 10-30 nm. Figure 6.1(b) show TEM image of an individual flower-like morphology of ZnO with plates inside the petals. Flower-like morphology was also reported by other researchers [18, 24, 25].

The formation mechanism of these flower-like structures can be explained according to Phuruangrat *et al.* [18]. When Zinc nitrate and NaOH are mixed they result in the milky precipitate of Zn(OH)<sub>2</sub>. This precipitate is decomposed by microwave vibration to form ZnO nuclei. ZnO nuclei grew into nanorods as time goes by, due to surface energy difference of crystallographic planes and simultaneously clustered into flower shaped structures [18]. Figure 6.1((c) and (d)) show the SEM and TEM images of PANI. PANI shows the worm-like morphology with a diameter of 163 nm. TEM image show rough edges with some fibrous structures in Figure 6.1(d). PANI-ZnO composites (Figure 6.1 (e) and (f)) also show a worm-like morphology.

The diameter of the ZnO-PANI (232 nm) composites was slightly more than that of PANI.

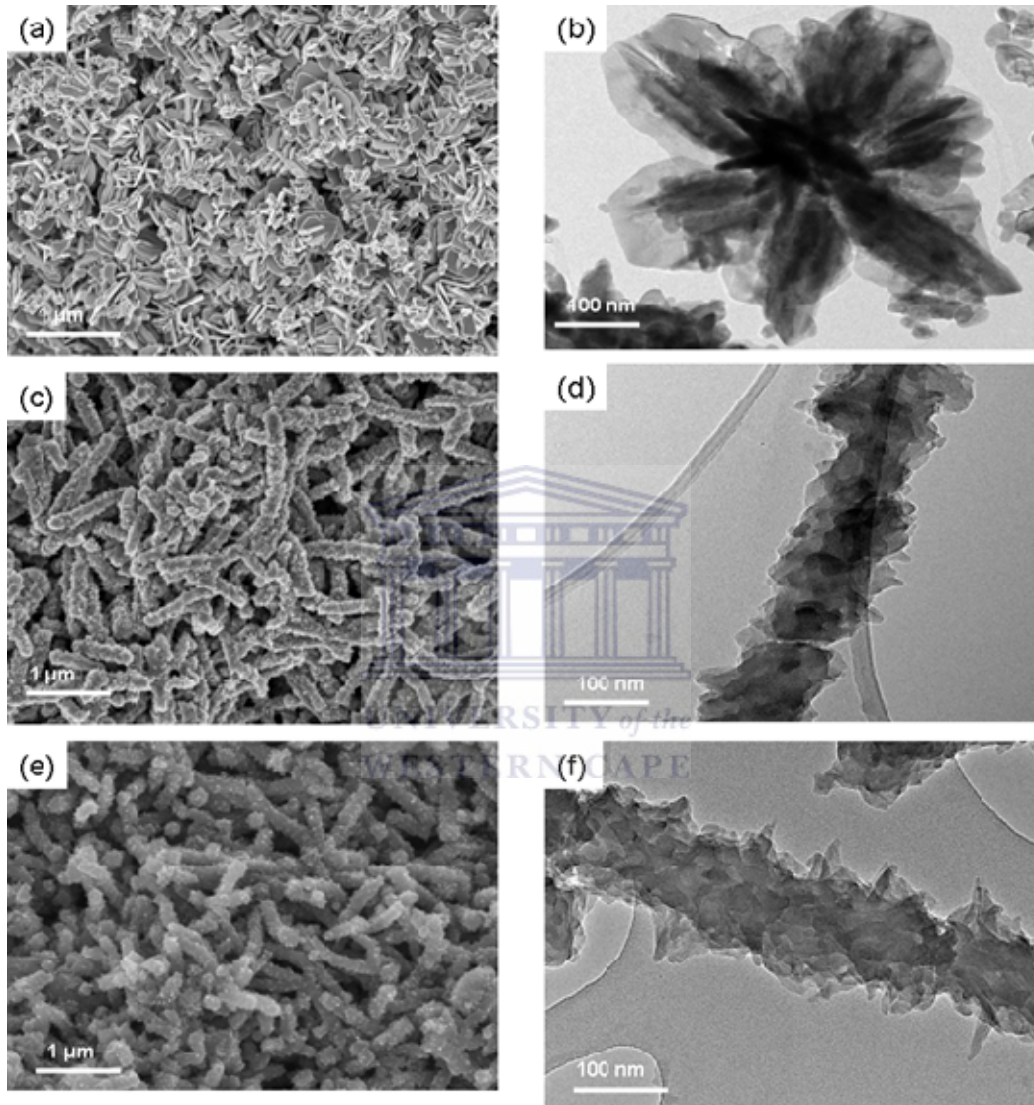


**Figure 6.1:** SEM and TEM images of ZnO ((a) and (b)), PANI ((c) and (d)) and PANI-ZnO composite ((e) and (f)).

On a separate experiment PANI was synthesized for 1 and 5 h to understand the effect of time in the worm-like morphology formation. It was found that after 1 h PANI (Figure 6.2(a)) had smooth fibres and had a diameter of about 90 nm. After 5 h PANI (Figure 6.2(b)) had a worm-like morphology with diameter 230 nm were formed. This gave an indication that the worm-like morphology form gradually as the reaction progresses. When APS was used instead of  $\text{KH}(\text{IO}_3)_2$  as an oxidant(Figure 6.2(c)), no worm-like morphology was observed. It can thus be concluded that the  $\text{KH}(\text{IO}_3)_2$  is responsible for the worm-like morphology formation.

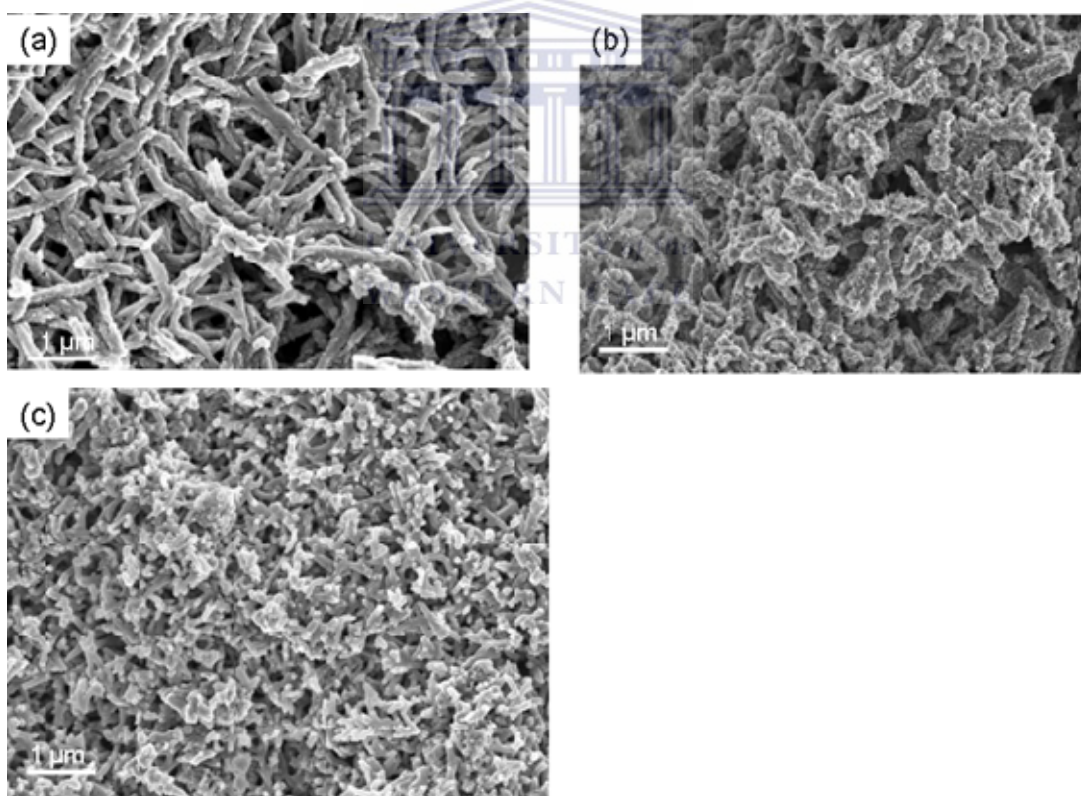


**Figure 6.2:** SEM images of PANI after 1 h (a) and after 5 h (b). PANI oxidised with ammonium persulphate(c).



### 6.3.2 UV-VIS CHARECTERISATION

The UV-Vis is of PANI, PANI-ZnO 1:1 and PANI-ZnO 1:2 is shown in Figure 6.3(a). PANI and PANI-ZnO 1:1 show three peaks around 360, 450, and 800 nm which are characteristics of highly doped PANI in its emeraldine salt. The band around 360 nm is due to  $\pi$ - $\pi^*$  transition of benzoic rings, the peak at 450 nm is attributed to polarons and the peak around 800 nm is due to doping level [21]. The 450 nm peak is an indication that PANI is in salt form (doped). The presences of the band at 800 nm make PANI and PANI-ZnO 1:1 composites good candidate for solar cells applications because of higher wavelength which will lead to improved light harvest. When more ZnO is put on the PANI backbone the PANI changed to emeraldine base. This is indicated by the two absorption bands observed at 330 and 650 nm in PANI-ZnO 1:2 composites. The band around 330 nm is due to benzoic rings transition and band at 650 nm is attributed to excitons-type transition between HOMO of benzoic ring and LUMO of quinoid ring. The ZnO shown in Figure 6.3(b) has the absorption at 375 nm which is a typical ZnO absorption [24].

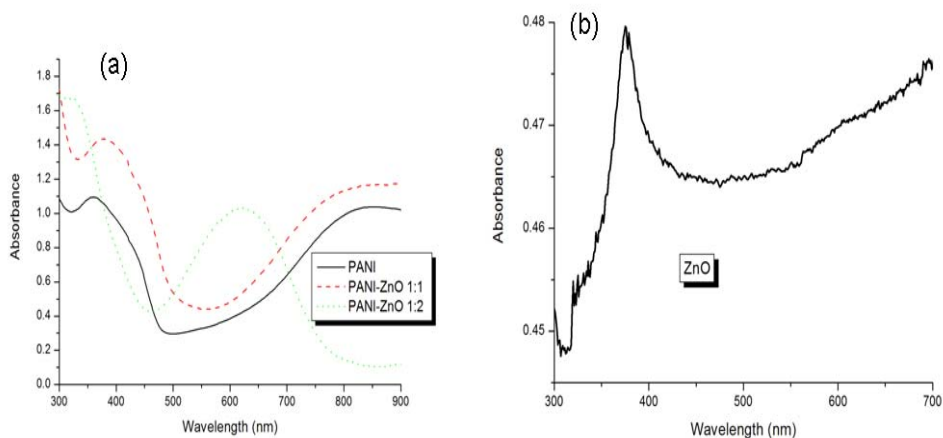


**Figure 6.3:** UV-Vis spectra of PANI, PANI-ZnO composites dissolved in NMP solution. The ZnO UV-Vis is shown in the insert.

### 6.3.3. RAMAN SPECTROSCOPY

Raman is the non-destructive technique which is sensitive to the electronic structural changes of a material. The spectra of ZnO and PANI and PANI-ZnO composites are shown in Figure 6.4. ZnO nanoflowers show peaks at 330, 383, 436 and 585  $\text{cm}^{-1}$  Raman shift. Raman shift of 380  $\text{cm}^{-1}$  was assigned to  $A_1(\text{TO})$  mode and 330 and 540  $\text{cm}^{-1}$  are due to the vibration modes as a result of the multiple-phonon scattering processes [26]. The observed  $E_1(\text{LO}) = 585 \text{ cm}^{-1}$  peak is associated with presence of oxygen vacancies and interstitial zinc and their complexes [27]. The  $E_2(\text{high}) = 436 \text{ cm}^{-1}$  peak is characteristic of the wurtzite lattice. The strong and sharp peak at 436  $\text{cm}^{-1}$  is an indication that ZnO was highly crystalline and of hexagonal wurtzite structure. The Raman spectra of the polymers show the characteristic of polyaniline in its protonated state. There are usually three regions in Raman spectra of polyaniline that are sensitive both to the level of oxidation, and the

protonation degree: (1) 1100–1210  $\text{cm}^{-1}$  region, where C-H bending vibrations of benzene or quinone type rings are most prominent and due to the degree of protonation; (2) 1210–1520  $\text{cm}^{-1}$  region with characteristic C–N and C=N stretching vibrations; (3) 1520–1650  $\text{cm}^{-1}$  region with the dominating C–C and C=C stretching vibration of benzene and quinone type rings, respectively [28, 29]. The presence of ZnO in the PANI backbone is confirmed by the appearance of peak at 436  $\text{cm}^{-1}$  in PANI-ZnO composites, this peak is the main peak observed in the ZnO.

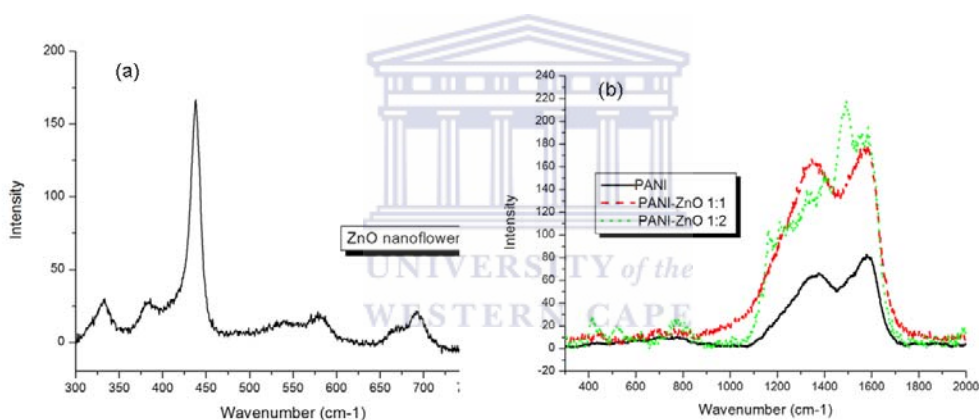


**Figure 6.4:** Raman Shift of ZnO nanoflowers (a) and PANI and PANI-ZnO composites (b).

### 6.3.4 X-RAY DIFFRACTION

X-ray diffraction was used to probe the structure of the ZnO (Figure 6.5(a)) and PANI and PANI-ZnO composites (Figure 6.5(a)) structures. X-Ray patterns of ZnO shown in Figure 6.5(a) are consistent with the peaks of wurtzite ZnO (JCPDS card No. 36-1451,  $a = 3.249 \text{ \AA}$   $c = 5.206 \text{ \AA}$ ) with high

crystallinity [11]. Both PANI and ZnO-PANI composites show three peaks around  $2\theta = 15^\circ$ ,  $20^\circ$  and  $25.4^\circ$  which are indicative of highly crystalline PANI [30]. The peak at  $20^\circ$  and  $25.4^\circ$  can be ascribed to the periodicity parallel and perpendicular to the polymer chains of PANI respectively. The peak at  $2\theta=15^\circ$  suggests the significant crystallization upon protonation [31].

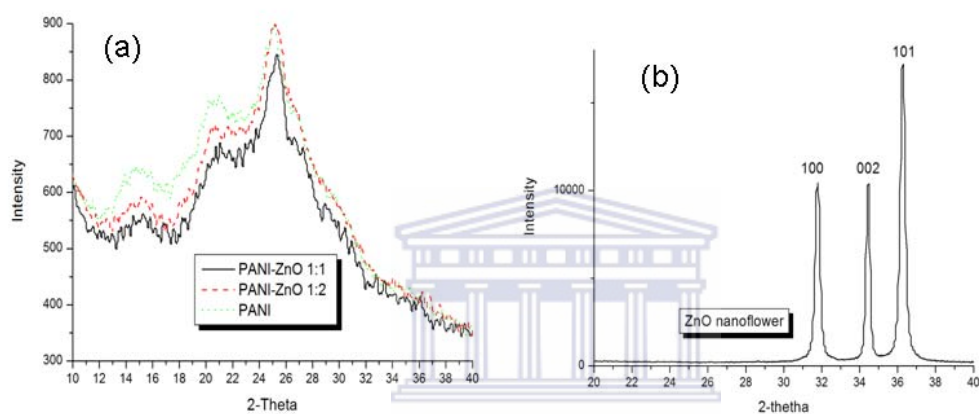


**Figure 6.5:** XRD micrographs of PANI and PANI-ZnO composites (Figure 5(a)) and ZnO (Figure 5(b))

### 6.3.5 SOLAR CELL PERFORMANCE AND CONDUCTIVITY

Four-point probe was used to calculate conductivity using the formula:

$$\sigma = \frac{(I/V)}{10.7S} \quad (6.1)$$

where  $\sigma$  is the conductivity,  $I$  is the current,  $V$  is the voltage and  $S$  is the distance between the probes, [32]. Table 6.1 presents the conductivity of PANI (oxidised with,  $\text{KH}(\text{IO}_3)_2$ ), PANI-ZnO composites and PANI oxidised with APS. For comparison, another PANI was prepared where APS was used as an oxidant. PANI oxidized with  $\text{KH}(\text{IO}_3)_2$  was found to be 10 times more

conductive than PANI oxidized with APS. The high conductivity might be due to high crystallinity and long fibres. It is well known that the crystallinity of PANI plays an important role in the electrical conductivity, because the crystallinity contributes to delocalization of charges within three-dimensional regions [33]. The longer fibres have less contact points than the shorter ones in the same unit distance, which will result in a high conductivity [8]. It can be seen from Table 6.1 that as more ZnO was added on PANI backbone the conductivity decreases. This decrease in conductivity might be due to fact that when ZnO is added on the PANI backbone it decreases the conjugation which will result in decrease in conductivity.

**Table 6.1:** Conductivity measurements

Sample	Conductivity S/cm
PANI	$2.1 \times 10^{-1}$
PANI-ZnO 2:1	$1.29 \times 10^{-1}$
PANI-ZnO 1:1	$9.1 \times 10^{-2}$
PANI**	$4.1 \times 10^{-2}$

\*\* oxidised with APS

The photovoltaic performance of different device active layers were characterized under simulated AM 1.5 illumination and is shown in Figure 6.6. The summary of the results is shown in Table 6.2. PANI/ZnO active layer exhibited a short circuit current ( $I_{sc}$ ) of  $0.03 \mu\text{A}/\text{cm}^2$ , open circuit voltage ( $V_{oc}$ ) of  $0.000175 \text{ V}$ , a fill factor (FF) of 22.8% and the power convection efficiency (PCE) of 0.00157%. It can be seen that the open circuit voltage is too low than

expected, the possible reason might be that electron mobility ZnO could be too high, resulting in increased carrier recombination at the ZnO/PANI interface and in a reduced  $V_{oc}$  or the presence of mid-gap states on the surface of the ZnO that pin the Fermi level [3]. The low short circuit current can also be due to poor contacts. This resulted in a poor fill factor. To improve the device performance the device architecture was changed from bilayer to bulk heterogeneous with PANI-ZnO blend or PANI:ZnO composites as an active layer. The blends were prepared by mixing 10 mg of PANI and ZnO in 1 mL of NMP. It was observed that the  $V_{oc}$  increased to 0.000963 and 0.012 V for PANI-ZnO composites and PANI-ZnO blends respectively. The fill factor was also enhanced to 24 and 25.6% for PANI-ZnO blends and PANI-ZnO composites respectively. The power conversion efficiency (PCE) also increased to 0.00012 and 0.00175% for ZnO-PANI blends and PANI-ZnO composites, respectively. The reason for the device improvement might be due to the reduced recombination caused by the increased interface by changing the device architecture to bulk heterogeneous junction. In bulk hetero-junction devices the donor and acceptor phases form an interpenetrating and continuous network in order for the separated charges to have a percolation path to the electrode. The highest FF of 26.4% was observed when PANI-ZnO composite layer was inserted between PANI and ZnO layer to build PANI/PANI-ZnO/ZnO diffused bilayer. Although this device had improved  $V_{oc}$  to 0.0034 V and FF to 26.4% the  $I_{sc}$  was lower and resulted in a lower efficiency of 0.00018%, this might be due to poor contacts.

**Table 6.2:** Device performance of polymer solar cell devices with various active layers.

Active layer	$I_{sc}$ ( $\mu A/cm^2$ )	$V_{oc}$ (V)	FF (%)	PCE (%)
PANI:ZnO (1:1) (blend)	0.035	0.0012	24	0.00012
PANI/ZnO	0.032	$1.75 \times 10^{-4}$	22.8	0.000157
PANI:ZnO (1:1) (composite)	0.57	$9.63 \times 10^{-4}$	25.6	0.00175
PANI/PANI:ZnO(composite)/ZnO	0.016	0.0034	26.4	0.00018

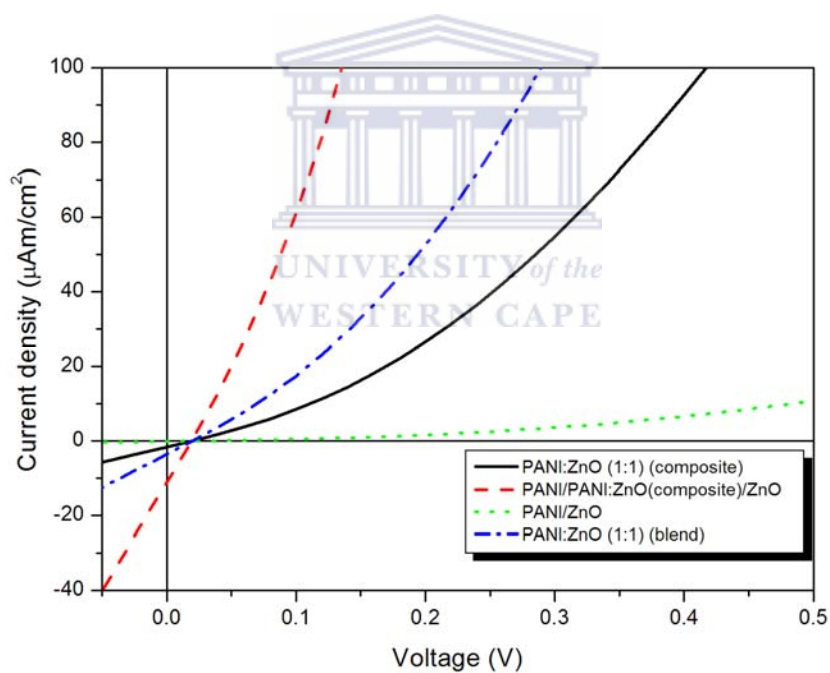


**Figure 6.6:** I-V characteristics of different active layers.

## 6.4. CONCLUSION

PANI with worm-like morphology and ZnO with flower-like morphology were successfully synthesized. It was found that  $\text{KH}(\text{IO}_3)_2$  was responsible for worm-like morphology formation. Solar cell devices that were fabricated using PANI as an donor and ZnO as an acceptor showed low performance which was improved by using PANI:ZnO composites instead of PANI:ZnO blends or PANI/ZnO bilayer.





## 6.5. REFERENCES:

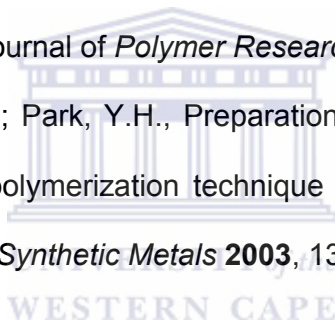
- [1]. Sharma, B.K.; Gupta, A.K.; Khare, N.; Dhawan, S.K.; Gupta, H.C., Synthesis and characterization of polyaniline-ZnO composite and its dielectric behavior. *Synthetic Metals* **2009**, 159, (5-6), 391-395.
- [2]. Khan, A.A.; Khalid, M., Synthesis of nano-sized ZnO and polyaniline-zinc oxide composite: Characterization, stability in terms of DC electrical conductivity retention and application in ammonia vapor detection. *Journal of Applied Polymer Science* **2010**, 117, (3), 1601-1607.
- [3]. Olson, D.C.; Piris, J.; Collins, R.T.; Shaheen, S.E.; Ginley, D.S., Hybrid photovoltaic devices of polymer and ZnO nanofiber composites. *Thin Solid Films* **2006**, 496, (1), 26-29.
- [4]. Chang, M.; Cao, X.L.; Zeng, H.; Zhang, L., Enhancement of the ultraviolet emission of ZnO nanostructures by polyaniline modification. *Chemical Physics Letters* **2007**, 446, (4-6), 370-373.
- [5]. Beek, W.J.E.; Wienk, M. M.; Janssen, R.A.J., Efficient Hybrid Solar Cells from Zinc Oxide Nanoparticles and a Conjugated Polymer. *Advanced Materials* **2004**, 16, (12), 1009-1013.
- [6]. Gunes, S.; Neugebauer, H.; Sariciftci, N., Conjugated Polymer-Based Organic Solar Cells. *Chemical Reviews* **2007**, 107, (4), 1324-1338.
- [7]. Zeng, T.W.; Lin, Y.T; Chen, C.W.; Su, W.F., Charge separation and transport properties of photovoltaic devices based on MEHPPV/TiO<sub>2</sub> nanorods hybrid materials. *Proceedings of SPIE* **2006**, 6334, 6334R-1 - 6334R-6.

- [8]. Rahy, A.; Yang, D. J., Synthesis of highly conductive polyaniline nanofibers. *Materials Letters* **2008**, 62, (28), 4311-4314.
- [9]. Huang, J.; Xia, C.; Cao, L.; Zeng, X., Facile microwave hydrothermal synthesis of zinc oxide one-dimensional nanostructure with three-dimensional morphology. *Materials Science and Engineering: B* **2008**, 150, (3), 187-193.
- [10]. Mohajerani, M.S.; Mazloumi, M.; Lak, A.; Kajbafvala, A.; Zanganeh, S.; Sadrnezhad, S.K., Self-assembled zinc oxide nanostructures via a rapid microwave-assisted route. *Journal of Crystal Growth* **2008**, 310, (15), 3621-3625.
- [11]. Xu, F.; Lu, Y.; Xie, Y.; Liu, Y., Synthesis and Photoluminescence of Assembly-Controlled ZnO Architectures by Aqueous Chemical Growth. *The Journal of Physical Chemistry C* **2008**, 113, (3), 1052-1059.
- [12]. Pan, A.L.; Liu, R.B.; Wang, S.Q.; Wu, Z.Y.; Cao, L.; Xie, S.S.; Zou, B.S., Controllable growth and optical properties of large scale ZnO arrays. *Journal of Crystal Growth* **2005**, 282, (1-2), 125-130.
- [13]. Wen, B.; Huang, Y.; Boland, J.J., Controllable Growth of ZnO Nanostructures by a Simple Solvothermal Process. *The Journal of Physical Chemistry C* **2007**, 112, (1), 106-111.
- [14]. Wang, Y.; Li, X.; Wang, N.; Quan, X.; Chen, Y., Controllable synthesis of ZnO nanoflowers and their morphology-dependent photocatalytic activities. *Separation and Purification Technology* **2008**, 62, (3), 727-732.
- [15]. Atienzar, P.; Ishwara, T.; Illy, B. N.; Ryan, M. P.; Regan, B. C.; Durrant, J.R.; Nelson, J., Control of Photocurrent Generation in Polymer/ZnO

- Nanorod Solar Cells by Using a Solution-Processed TiO<sub>2</sub> Overlayer. *The Journal of Physical Chemistry Letters* **2010**, 1, (4), 708-713.
- [16]. Chiu, W.-H.; Lee, C.-H.; Cheng, H.-M.; Lin, H.-F.; Liao, S.-C.; Wu, J.-M.; Hsieh, W.-F., Efficient electron transport in tetrapod-like ZnO metal-free dye-sensitized solar cells. *Energy & Environmental Science* **2009**, 2, (6), 694-698.
- [17]. Jiang, C.Y.; Sun, X.W.; Lo, G.Q.; Kwong, D.L., Improved dye-sensitized solar cells with a ZnO-nanoflower photoanode. *Applied Physics Letters* **2007**, 90, (26) 263501-263503.
- [18]. Phuruangrat, A.; Thongtem, T.; Thongtem, S., Microwave-assisted synthesis of ZnO nanostructure flowers. *Materials Letters* **2009**, 63, (13-14), 1224-1226.
- [19]. Sun, Q.; Park, M.-C.; Deng, Y., Studies on one-dimensional polyaniline (PANI) nanostructures and the morphological evolution. *Materials Chemistry and Physics* **2008**, 110, (2-3), 276-279.
- [20]. Sun, Q.; Park, M.-C.; Deng, Y., Dendritic superstructure formation of polyaniline prepared using a water-soluble polyelectrolyte copolymer as the support matrix. *Materials Letters* **2007**, 61, (14-15), 3052-3055.
- [21]. Mavundla, S.E.; Malgas, G.F.; Baker, P.; Iwuoha, E.I., Synthesis and Characterization of Novel Nanophase Hexagonal Poly(2,5-dimethoxyaniline). *Electroanalysis* **2008**, 20, (21), 2347-2353.
- [22]. Zhao, G.-Y.; Li, H.-L., Preparation of polyaniline nanowire arrayed electrodes for electrochemical supercapacitors. *Microporous and Mesoporous Materials* **2008**, 110, (2-3), 590-594.

- [23]. Bejbouji, H.; Vignau, L.; Miane, J.L.; Dang, M.-T.; Oualim, E.M.; Harmouchi, M.; Mouhsen, A., Polyaniline as a hole injection layer on organic photovoltaic cells. *Solar Energy Materials and Solar Cells* **2010**, 94, (2), 176-181.
- [24]. Liu, Y.-L.; Yang, Y.-H.; Yang, H.-F.; Liu, Z.-M.; Shen, G.-L.; Yu, R.-Q., Nanosized flower-like ZnO synthesized by a simple hydrothermal method and applied as matrix for horseradish peroxidase immobilization for electro-biosensing. *Journal of Inorganic Biochemistry* **2005**, 99, (10), 2046-2053.
- [25]. Ahsanulhaq, Q.; Kim, S.H.; Kim, J.H.; Hahn, Y.B., Structural properties and growth mechanism of flower-like ZnO structures obtained by simple solution method. *Materials Research Bulletin* **2008**, 43, (12), 3483-3489.
- [26]. Lv, Y.Z.; Zhang, Y.H.; Li, C.P.; Ren, L.R.; Guo, L.; Xu, H.B.; Ding, L.; Yang, C.L.; Ge, W.K.; Yang, S.H., Temperature-dependent photoluminescence of ZnO nanorods prepared by a simple solution route. *Journal of Luminescence* **2007**, 122-123, 816-818.
- [27]. Lo, S.-S.; Huang, D., Morphological Variation and Raman Spectroscopy of ZnO Hollow Microspheres Prepared by a Chemical Colloidal Process. *Langmuir* **2010**, 26, (9), 6762-6766.
- [28]. Mishra, A.K.; Tandon, P.; Gupta, V.D., Vibrational Dynamics of Polyaniline Pernigraniline Base Form: A Conducting Polymer. *Macromolecular Symposia* **2008**, 265, (1), 111-123.
- [29]. Mazeikiene, R.; Tomkute, V.; Kuodis, Z.; Niaura, G.; Malinauskas, A., Raman spectroelectrochemical study of polyaniline and sulfonated

- polyaniline in solutions of different pH. *Vibrational Spectroscopy* **2007**, 44, (2), 201-208.
- [30]. Mavundla, S.; Malgas, G.; Motaung, D.; Iwuoha, E., Physicochemical and morphological properties of poly(aniline-pyrrole) . *Journal of Materials Science* **2010**, 45, (12), 3325-3330.
- [31]. Chang, M.; Cao, X.L.; Zeng, H.; Zhang, L., Enhancement of the ultraviolet emission of ZnO nanostructures by polyaniline modification. *Chemical Physics Letters* **2007**, 446, (4-6), 370-373.
- [32]. Ebrahim, S.M., Fabrication of Schottky diode based on Zn electrode and polyaniline doped with 2-acrylamido-2-methyl-1-propanesulfonic acid sodium salt. *Journal of Polymer Research* **2009**, 16, (5), 481–487.
- [33]. Bae, W.; Jo, W.H.; Park, Y.H., Preparation of polystyrene/polyaniline blends by in situ polymerization technique and their morphology and electrical property. *Synthetic Metals* **2003**, 132, (3), 239-244.

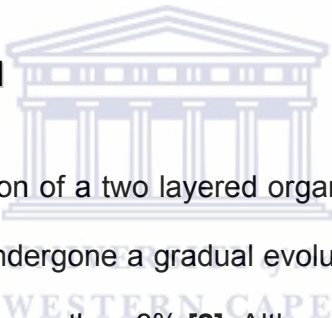


# CHAPTER SEVEN

---

## HYBRID SOLAR CELLS FROM POLY(2,5 DIMETHOXYANILINE) HEXAGONAL STRUCTURES AND ZINC OXIDE

### 7.1. INTRODUCTION



Since the introduction of a two layered organic solar cells by Tang [1], organic solar cells have undergone a gradual evolution that has led to energy conversion efficiencies of more than 6% [2]. Although organic solar cells show low efficiencies, the simplicity of devices and the potential to increase efficiency makes them worthwhile prospect for research and development [3]. The weak absorption in the visible long wavelength, poor charge transport and low stability are some of the reasons for the poor performance of organic solar cells. The transport of the charges after their separation simply relies on the percolation network of the components of the mixture films, which is not easy to control precisely through dynamic coating or simple thermal annealing [3].

One way to improve charge transport is to replace one of the organic components with an inorganic material. These types of devices are called hybrid solar cells. The advantages of hybrid solar cells over purely organic

counterparts are environmental stability, high electron transport, and the ability to optimize interfacial properties [4]. The control of morphology of inorganic semiconductors from spherical to one dimensional structure is attractive for solar cell application because of their ability to provide direct path for charge transport [5, 6]. It has been previously shown that photo-induced charge transfer can also occur between a conjugated polymer and a metal oxide semiconductor such as SnO<sub>2</sub>, TiO<sub>2</sub>, and ZnO [7]. Among metal oxides ZnO is one of the most studied because of its tunable morphology, wide band gap, cheap, high mobility and easy to synthesize. Various morphology of ZnO has been reported including nanowires, flowers, rods and tubes, and two-dimensional structures including sheets and ribbons have been synthesized [8-10]. On the other hand polyaniline is one of the most studied polymers due to its high conductivity, environmental stability and low cost of production [11]. PANI can also act as a barrier to oxygen and as a planarizing layer to inhibit electrical shorts and improve device lifetime, resulting in an improvement of the brightness and the efficiency of the Organic Light Emitting Diodes [12]. It has been shown that by incorporating one dimensional structure polyaniline as interfacial layer in organic solar cell, the efficiency can improve by up to 26% [13].

In this work the photovoltaic performance of devices made from polymers with different morphology is studied. The ZnO and C<sub>60</sub> are used as electron acceptors. The use C<sub>60</sub> was for comparison as it is one of the commonly used electron acceptors. All the electron donors were synthesized as reported in chapter 4 and 5 or as in reference [11, 14].

## **7.2. EXPERIMENTAL**

### **7.2.1. MATERIALS**

Zinc nitrate, Potassium Hydroxide (KOH), buckminsterfullerene- C<sub>60</sub> with a purity of 99.5%, Indium tin oxide (ITO) coated on a 1 mm glass substrate with a sheet resistance of 8-12  $\Omega/\text{sq}^{-1}$ , poly(3,4-ethylenedioxythiophene):poly(styrenesulfonate) (PEDOT:PSS) and hydrochloric acid (HCl) were purchased from Sigma-Aldrich. All chemicals were used as received without further purification. ITO was purchased from

### **7.2.2. SYNTHESIS OF ZnO NANOSTRUCTURES**

ZnO nanostructures were prepared by dissolving 4.8 g of Zinc nitrate in 50 mL of deionised water. 4 g of the KOH was added with continuous stirring to make a colloidal solution. The resulting solution was transferred to 100 mL Teflon liner and put in a vessel. The solution was then put on microwave and treated at 180 °C for 20 min under temperature controlled mode. The reaction was then terminated and cooled at room temperature and the product was dried at 80 °C.

### **7.2.3. FABRICATION OF DEVICES**

The ITO glass substrate was cleaned with methanol. Poly(3,4-ethylenedioxythiophene) poly(styrenesulfonate) (PEDOT:PSS) was spin coated on the cleaned ITO glass and dried on the hot plate at 100 °C for 20 min. The blend with a ratio of 1:1 (w/w) of donor and acceptor was prepared by dissolving 5 g of and 5 g of acceptor in 2 mL of NMP. The blend was spin



coated on the PEDOT:PSS/ITO substrate and dried at 100 °C for 30 min. On the other glass about 150 nm of the aluminum film was deposited. This Al/Glass substrate was placed on top of Blend/PEDOT:PSS/ITO layer and laminated together by pressing the substrates against each other and adding a small amount of adhesive to seal.

#### **7.2.4. CHARACTERIZATION**

Microwave synthesis was performed on a Perkin Elmer/Anton Paar Multiwave 3000. The scanning electron microscopy (SEM) samples were prepared by placing some of the synthesized material onto an aluminum stub. A carbon sticky tape was placed on the aluminum stub for adhesion of the material. The samples were sputter-coated with a thin layer of carbon to prevent charging effects inside the microscope. The morphology of the prepared materials was examined on Neon 40 (Zeiss) FIB-SEM. Ultraviolet-visible (UV-Vis) spectra were recorded on a PerkinElmer Lambda 750S spectrometer from 320 to 900 nm. Photoluminescence (PL) measurements were recorded on PerkinElmer LS 55 spectrometer by exciting the samples with a 320 nm line of deuterium lamp. The UV-Vis and PL samples were prepared by dissolving small amount of a material in DMF. The X-ray diffraction patterns of powders were recorded on a Phillips (PANalytical) X-ray diffractometer using Cu K $\alpha$  ( $\lambda = 1.54\text{\AA}$ ) radiation source. The diffractogram was in terms of  $2\theta$  in the range 5–40°. Conductivity and current-voltage(I-V) characterization were performed on a Keithly 4200 Semiconductor Characterization System.

## 7.3. RESULTS AND DISCUSSION

### 7.3.1. SCANNING ELECTRON MICROSCOPY

Figure 7.1 shows the SEM images of ZnO (a), PANI with worm-like morphology (b), PDMA (c), PANI (d), PANI-PPy (e), and PDMA-PPy (f) morphologies. The morphology of the polymers ((c), (d), (e) and (f)) was reported elsewhere [11, 14]. The images were put in order to be able to compare easily. The formation mechanism for PDMA and PANI hexagonal structures was also discussed in Chapter 4 or reference [14]. Figure 7.1(b) shows PANI with worm-like morphology, which are 163 nm in diameter and about 2  $\mu\text{m}$  long. ZnO with nanopencils morphology is shown in Figure 7.1(a). The nanopencils show hexagonal structures with sharp ends. They are about 400 nm in diameter and  $\sim 1.6 \mu\text{m}$  long. From the SEM images it appears that nanopencils are grown out of a base bulk material.

Their formation can be ascribed to the fact that ZnO is a polar hexagonal, highly anisotropic crystal that grows along the c axis, (0001) because of the lowest surface energy of the (0002) facet [15]. The zinc and oxygen atoms in the ZnO crystal are arranged alternately along the c-axis, and the top surfaces are Zn terminated (0001) and are catalytically active, while the bottom surfaces are O-terminated (000 $\bar{1}$ ) and are chemically inert [16]. Under hydrothermal conditions the polar (0001) faces are the most rapid-growth rate planes as compared to other growth facets [15, 16] and hence the nanopencil morphology is preferred.

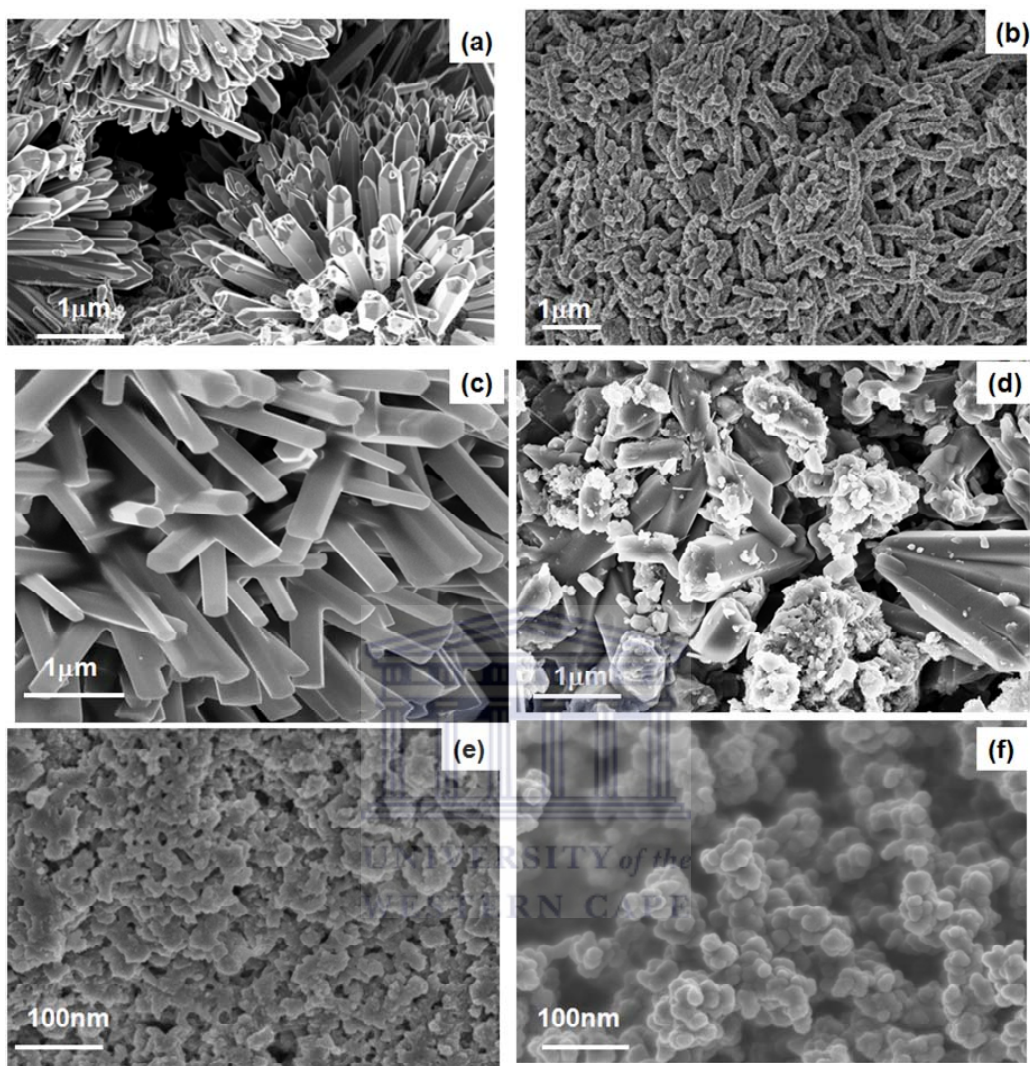


**Figure 7.1:** Scanning Electron microscope images of ZnO nanopencils (a), PANI with worm-like morphology (b), PDMA(c), PANI (d), PDMA-PPy(e) and PANI-PPy (f).

### 7.3.2. X-RAY DIFFRACTION

Poly(2,5-dimethoxyaniline) and PANI with hexagonal morphology are shown in Figure 7.2(a), and PDMA-PPy and PANI-PPy copolymers are shown in Figure (b). Very sharp and strong peaks are observed for PDMA and PANI hexagonal structures at  $2\theta = 11.8^\circ$ ,  $20.5^\circ$ ,  $26.5^\circ$  and  $27^\circ$ . These peaks are a strong indication that the polymers are highly crystalline. The peaks at ( $26.5$  and  $27$ ) and  $20.5^\circ$  can be ascribed to the periodicity parallel and perpendicular to the polymer chains of PANI, respectively [14]. The peak  $2\theta = 11.8^\circ$  is indication of a significant crystallization upon protonation [17]. The reason for such a high crystalline PDMA and PANI is due to the synthetic process that was explained somewhere [14]. PDMA-PPy and PANI-PPy show broad peaks around  $2\theta = 18^\circ$ - $30^\circ$  which is due to amorphous behaviour of copolymers. X-Ray patterns of ZnO nanostructures are shown in Figure 7.2(c). All the diffraction peaks are consistent with the peaks of wurtzite ZnO (JCPDS card No. 36-1451,  $a = 3.249 \text{ \AA}$ ,  $c = 5.206 \text{ \AA}$ ) [18]. The sharp and strong peaks are the indication of a highly crystalline material.

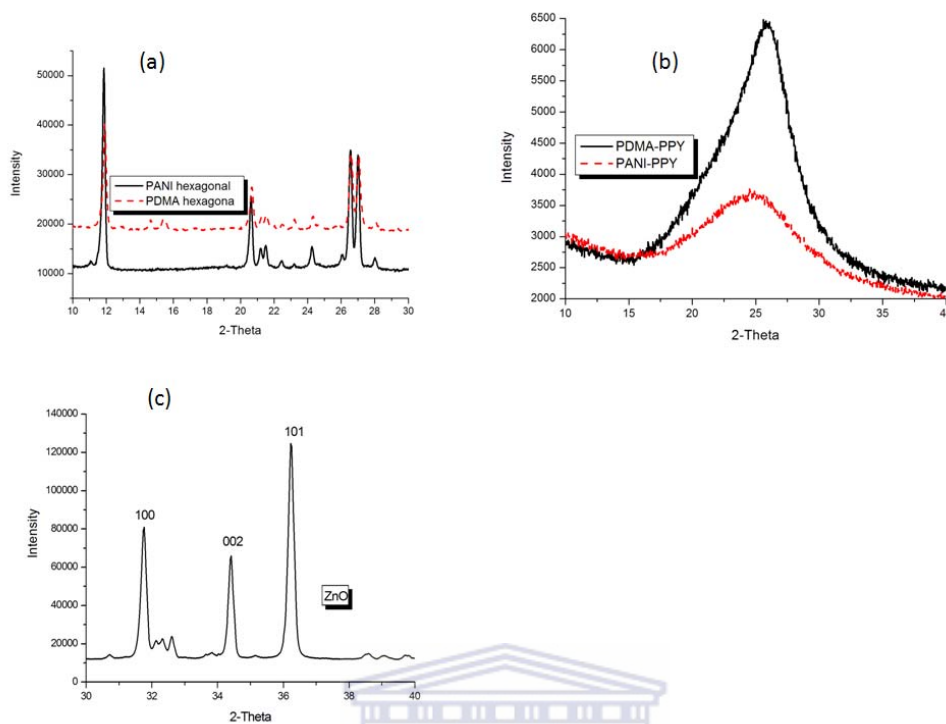


**Figure 7.2:** X-Ray Diffraction of PANI and PDMA hexagonal (a), PANI-PPY and PDMA-PPY copolymers (b) and ZnO (c)..

### 7.3.3. PHOTOLUMINESCENCE

The photoluminescence of nanostructures was measured using an excitation wavelength of 320 nm in solution form, with ZnO dissolved in ethanol and polymers in NMP. The photoluminescence spectra of ZnO nanostructures are shown in Figure 7.3(a). Zinc oxide nanopencils show a strong peak around 390 nm. This peak is attributed to the Ultraviolet (UV) emission of ZnO which is due to band edge emission or radiative annihilation of excitons [19, 20]. The ZnO also show blue band at 430 and 460 nm, a blue-green band situated around 480 and a green band 529 nm. The blue -green band emission correspond to the singly occupied oxygen vacancy in ZnO and

also results from recombination of photo-generated hole with single ionized charged state of this defect [19,21]. Figure 7.3(b) show PL spectra of PANI, PDMA, PDMA-PPy and PANI-PPy copolymers. All the spectra showed peaks at 390, 440 and 480 nm except PANI which showed a strong peak at 420 nm. The peak at 390 and 440 nm are due to the benzoic groups causing the emission in the different polymers and the small shoulder at 480 nm is due to the protonation form or the dope state of the polymer [14, 22]. Poly(2,5-dimethoxyaniline) and PDMA-PPy showed a strong peak at 480 and 520 nm respectively which indicates that these materials were more protonated and more doped than the others which showed a shoulder. These materials can be good candidates for solar cells because of a broader spectrum absorption than others which can improve light harvest.

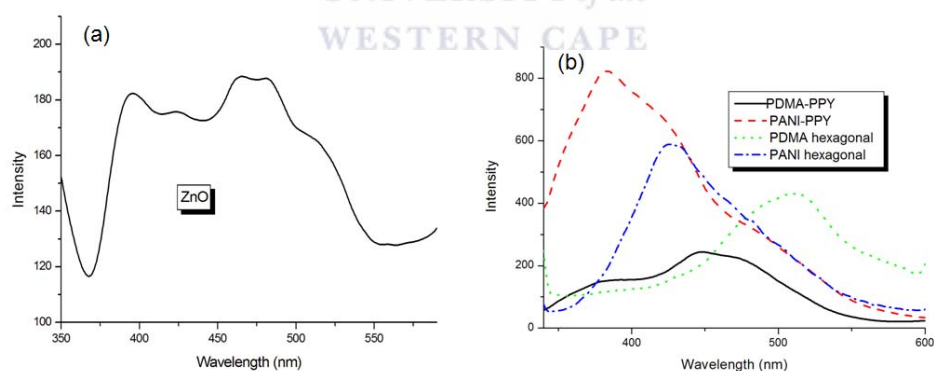


**Figure 7.3:** Photoluminescence spectra of ZnO (a) and PANI, PDMA, PANI-PPy and PDMA-PPy (b).

### 7.3.4. SOLAR CELL CHARACTERIZATION

Figure 7.4(a) show the current-voltage (I-V) characteristics of ITO/PDMA:ZnO/Al, ITO/PDMA:C<sub>60</sub>/Al, and ITO/PDMA-PPy:C<sub>60</sub>/Al devices with 1:1(w/w) ratio of donor: acceptor measured under simulated AM 1.5 illumination. The photovoltaics parameters ( $V_{oc}$ ,  $I_{sc}$ , FF, and PCE) of these devices are listed in Table 7.1. When we compare the performance of PDMA as a donor when used with either ZnO or C<sub>60</sub> as an acceptor, it was found that when ZnO was used as an acceptor the device performed better with  $V_{oc} = 0.58$  V,  $I_{sc} = 0.93$   $\mu$ A, FF = 24.1 and PCE = 0.162% where as ZnO:C<sub>60</sub> had  $V_{oc} = 0.182$  V,  $I_{sc} = 1.39$   $\mu$ A, FF = 24.5 and PCE = 0.051%. It can be seen that although the PCE of PDMA:C<sub>60</sub> is low compared to the PDMA:ZnO, it had higher short circuit current and fill factor. It is known that C<sub>60</sub> is a stronger electron acceptor than ZnO and is more efficient in charge separation which may lead to enhancement of photocurrent [23, 24].

On the other hand the higher current might be due to the higher absorption of C<sub>60</sub> (ZnO absorb around 380 nm and C<sub>60</sub> absorb around 500 nm). It has been previously shown that the increased photon harvesting from the solar spectrum result in higher photocurrent [4, 7]. The  $V_{oc}$  was higher when ZnO was used as the acceptor with PDMA as donor. The origin of the  $V_{oc}$  in organic solar cells is not fully understood, it is widely believed to have a maximum value given by the difference in energy between donor HOMO and acceptor LUMO [4], and for us this was not the case. The higher  $V_{oc}$  for the PDMA:ZnO was attributed to the fact that both ZnO and PDMA had one-dimensional morphology which enhances the charge transport.

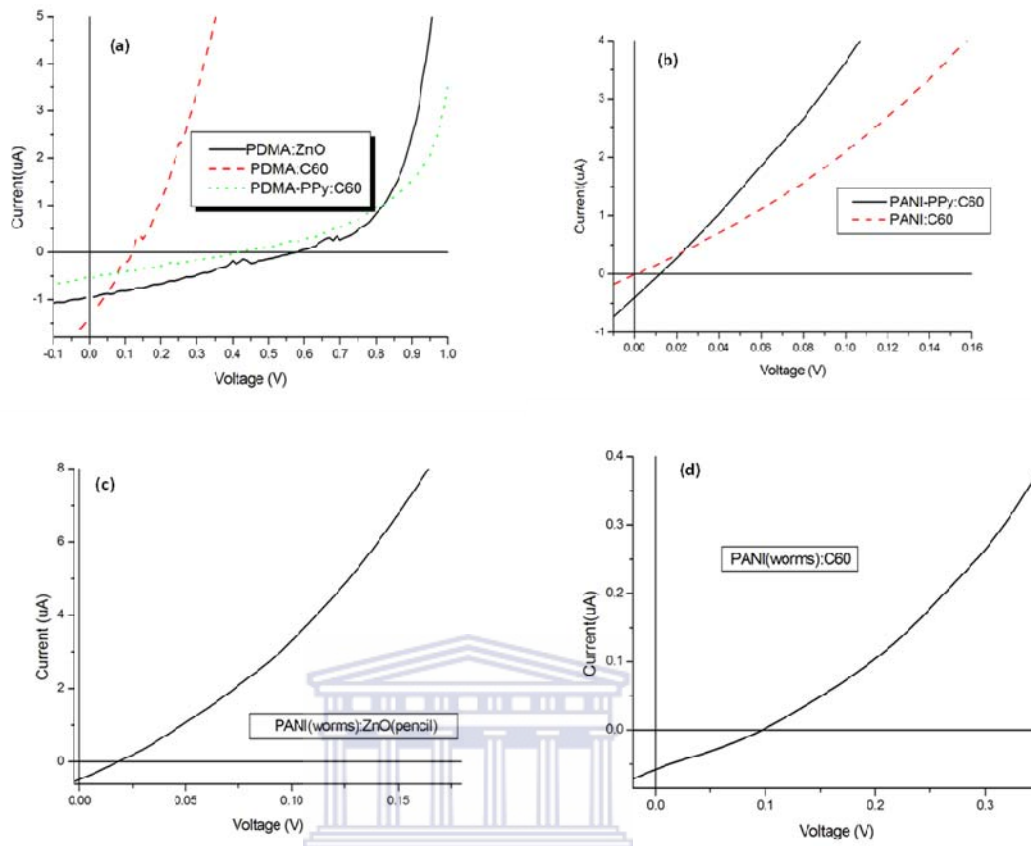


**Figure 7.4:** Current-voltage (I-V) characteristic of different of PDMA:C<sub>60</sub>, PDMA:ZnO and PDMA-PPy:C<sub>60</sub> (a) and PANI:C<sub>60</sub> and PANI-PPy:C<sub>60</sub> (b) , PANI(worm-like):ZnO(c) and PANI(worms):C<sub>60</sub> (d)

Higher crystallinity as depicted by XRD may also be responsible for the high  $V_{oc}$  compared to ZnO:C<sub>60</sub>. When PDMA-PPy copolymer is used as a donor with ZnO as an acceptor, it is found that although the efficiency is very low (0.000214%), the short circuit current (0.83  $\mu$ A) was greater than the 0.53  $\mu$ A obtained for PDMA-PPy:C<sub>60</sub>. The efficiency was improved by 100 times when C<sub>60</sub> was used as an acceptor instead of ZnO. The  $V_{oc}$  was also improved from  $4.4 \times 10^{-4}$  to 0.42 V. This improvement can be attributed to the



fact that spherical  $C_{60}$  molecules with larger surface to volume ratio are more efficient in separating the photogenerated charge carriers than one-dimensional structures when distributed in a polymer matrix [23]. Figure 7.4(b) show the current-voltage characteristics of PANI: $C_{60}$  and PANI-PPy: $C_{60}$ . PANI-PPy: $C_{60}$  device had low short current at  $0.011 \mu\text{A}$ , very low  $V_{oc} = 8.58 \times 10^{-4} \text{ V}$  and  $1.45 \times 10^{-6}\%$  efficiency where as PANI: $C_{60}$  had  $V_{oc} = 0.012 \text{ V}$ ,  $I_{sc} = 0.41 \mu\text{A}$  and  $\text{PCE} = 1.47 \times 10^{-3}\%$ .

Although PANI is crystalline and one dimensional, its performance was poor compared to PDMA. This behavior was attributed to its morphology: it exhibits fibrous properties that could have hindered charge transport. Polyaniline with worm-like morphology was also used as a donor with ZnO as acceptor and compared with device where  $C_{60}$  was used instead of ZnO. Their Current-voltage characteristics are shown in Figure 67.4(a) and (b). When ZnO is used instead of  $C_{60}$  the  $I_{sc}$  improved from  $0.058$  to  $0.49 \mu\text{A}$ ,  $V_{oc}$  decrease from  $0.097$  to  $0.018 \text{ V}$ , the FF also decrease from  $26.1$  to  $25.5\%$  and the PCE was improved from  $0.0019$  to  $0.0028\%$ . When ZnO with flowers-like morphology was used as an acceptor with PDMA as a donor, the PCE decreased to  $1.4 \times 10^{-6}\%$  which is almost 100 000 less. This shows that one-dimensional structures are crucial in solar cells applications.

**Table 7.1:** Photovoltaic parameters of different active layers under 800 mWcm<sup>-2</sup> simulated solar irradiation.

Active layer	I <sub>sc</sub> (μA)	V <sub>oc</sub> (V)	FF %	CPE %
PDMA:ZnO	0.93	0.58	0.241	0.162
PDMA:C <sub>60</sub>	1.39	0.12	0.245	0.051
PD-PPy:C <sub>60</sub>	0.53	0.42	0.200	0.055
PD-PPy:ZnO	0.822	8.58 x10 <sup>-4</sup>	0.243	2.14x10 <sup>-4</sup>
PANI:C <sub>60</sub>	0.401	0.012	0.244	1.47 x10 <sup>-3</sup>
PA-PPy:C <sub>60</sub>	0.011	4.4 x10 <sup>-4</sup>	0.239	1.45 x10 <sup>-6</sup>
PANI*:ZnO	0.49	0.018	0.255	0.0028
PDMA:ZnO**	0.0039	0.0011	0.261	1.4 x10 <sup>-6</sup>
PANI*:C <sub>60</sub>	0.058	0.097	0.264	0.0019

\*PANI with nanoworm morphology

\*\*ZnO with flower-like morphology

## 7.4. CONCLUSION

This study showed that the combination of one-dimensional morphology and crystallinity of the organic polymer is crucial for improvement of solar cells performance. Poly(2,5-dimethoxyaniline) with hexagonal structures showed high efficiency due to its highly crystalline structure as depicted by XRD and smooth one-dimensional morphology. It can be noticed that when one-dimensional acceptor is used with one-dimensional donor the performance improved due to the efficient charge transport. When C<sub>60</sub> is used with PDMA as an electron acceptor it was out performed by ZnO oxide because it had spherical morphology.



## 7.5. REFERENCES:

- [1]. Tang, C. W., Two layered organic photovoltaic cell. *Applied Physics Letters* **1986**, 48, (2), 183-185.
- [2]. Kim, S.-S.; Jo, J.; Chun, C.; Hong, J.-C.; Kim, D.-Y., Hybrid solar cells with ordered TiO<sub>2</sub> nanostructures and MEH-PPV. *Journal of Photochemistry and Photobiology A: Chemistry* **2007**, 188, (2-3), 364-370.
- [3]. Das, N. C.; Sokol, P. E., Hybrid photovoltaic devices from regioregular polythiophene and ZnO nanoparticles composites. *Renewable Energy* **2010**, 35, (12), 2683-2688.
- [4]. Dissanayake, D.M.N.M; Hatton, R.A.; Lutz, T.; Giusca, E.C.; Curry, R.J.; Silva, S.R.P., A PbS nanocrystal-C60 Photovoltaic Device for Infrared Light Harvesting. *Applied Physics Letters* **2007**, 91 (13) 133506-133508.
- [5]. Briseno, A.L.; Holcombe, T. W.; Boukai, A.I.; Garnett, E.C.; Shelton, S. W.; Frechet, J. J. M.; Yang, P., Oligo- and Polythiophene/ZnO Hybrid Nanowire Solar Cells. *Nano Letters* **2009**, 10, (1), 334-340.
- [6]. Huynh, W.U.; Dittmer, J.J.; Libby, W.C.; Whiting, G.L.; Alivisatos, A.P., Controlling the Morphology of Nanocrystal–Polymer Composites for Solar Cells. *Advanced Functional Materials* **2003**, 13, (1), 73-79.
- [7]. Kumar, H.; Kumar, P.; Bhardwaj, R.; Sharma, G.D.; Chand, S.; Jain, S.C.; Kumar, V., Broad spectral sensitivity and improved efficiency in CuPc/Sub-Pc organic photovoltaic devices. *Journal of Physics D: Applied Physics* **2009**, 42, (1), 015103.

- [8]. Wang, J.; Wang, J.; Yang, Z.; Wang, Z.; Zhang, F.; Wang, S., A novel strategy for the synthesis of polyaniline nanostructures with controlled morphology. *Reactive and Functional Polymers* **2008**, 68, (10), 1435-1440.
- [9]. Jiang, C.Y.; Sun, X.W.; Lo G.Q.; Kwong, D.L, Improved dye-sensitized solar cells with a ZnO-nanoflower photoanode. *Applied Physics Letters* **2007**, 90, (26), 263501-263503.
- [10]. Atienzar, P.; Ishwara, T.; Illy, B. N.; Ryan, M.P.; Regan, B.C.; Durrant, J.R.; Nelson, J., Control of Photocurrent Generation in Polymer/ZnO Nanorod Solar Cells by Using a Solution-Processed TiO<sub>2</sub> Overlayer. *The Journal of Physical Chemistry Letters* **2010**, 1, (4), 708-713.
- [11]. Mavundla, S.E.; Malgas, G.F.; Baker, P.; Iwuoha, E.I., Synthesis and Characterization of Novel Nanophase Hexagonal Poly(2,5-dimethoxyaniline). *Electroanalysis* **2008**, 20, (21), 2347-2353.
- [12]. Chang, M.-Y.; Wu, C.-S.; Chen, Y.-F.; Hsieh, B.-Z.; Huang, W.-Y.; Ho, K.-S.; Hsieh, T.-H.; Han, Y.-K., Polymer solar cells incorporating one-dimensional polyaniline nanotubes. *Organic Electronics* **2008**, 9, (6), 1136-1139.
- [13]. Bejbouji, H.; Vignau, L.; Miane, J. L.; Dang, M.-T.; Oualim, E.M.; Harmouchi, M.; Mouhsen, A., Polyaniline as a hole injection layer on organic photovoltaic cells. *Solar Energy Materials and Solar Cells* **2010**, (2), 176-181.
- [14]. Mavundla, S.; Malgas, G.; Motaung, D.; Iwuoha, E., Physicochemical and morphological properties of poly(aniline-pyrrole). *Journal of Materials Science* **2010**, 45, (12), 3325-3330.

- [15]. Pol, V.G.; Calderon-Moreno, J.M.; Thiyagarajan, P., Facile Synthesis of Novel Photoluminescent ZnO Micro- and Nanopencils. *Langmuir* **2008**, 24, (23), 13640-13645.
- [16]. Ahsanulhaq, Q.; Kim, S.H.; Kim, J.H.; Hahn, Y.B., Structural properties and growth mechanism of flower-like ZnO structures obtained by simple solution method. *Materials Research Bulletin* **2008**, 43, (12), 3483-3489.
- [17]. Amarnath, C. A.; Palaniappan, S., Polyaniline doped by a new class of dopants, benzoic acid and substituted benzoic acid: synthesis and characterization. *Polymers for Advanced Technologies* **2005**, 16, (5), 420-424.
- [18]. Xu, F.; Lu, Y.; Xie, Y.; Liu, Y., Synthesis and Photoluminescence of Assembly-Controlled ZnO Architectures by Aqueous Chemical Growth. *The Journal of Physical Chemistry C* **2008**, 113, (3), 1052-1059.
- [19]. Chang, M.; Cao, X. L.; Zeng, H.; Zhang, L., Enhancement of the ultraviolet emission of ZnO nanostructures by polyaniline modification. *Chemical Physics Letters* **2007**, 446, (4-6), 370-373.
- [20]. Zheng, X.Z.; Xi, Y.Y.; Dong, P.; Huang, G.H.; Zhou, Z.J.; Wu, L.L.; Lin, H.Z., The enhanced photoluminescence of zinc oxide and polyaniline coaxial nanowire arrays in anodic oxide aluminium membranes. *PhysChemComm* **2002**, 5, (9), 63-65.
- [21]. Phuruangrat, A.; Thongtem, T.; Thongtem, S., Microwave-assisted synthesis of ZnO nanostructure flowers. *Materials Letters* **2009**, 63, (13-14), 1224-1226.

- [22]. Shimano, J.Y.; MacDiarmid, A.G., Polyaniline, a dynamic block copolymer: key to attaining its intrinsic conductivity? *Synthetic Metals* **2001**, 123, (2), 251-262.
- [23]. Sun, J.; Zhu, Y.; Yang, X.; Li, C., Photoelectrochemical glucose biosensor incorporating CdS nanoparticles. *Particuology* **2009**, 7, (5), 347-352.
- [24]. Yildiz, H.B.; Tel-Vered, R.; Willner, I., Solar Cells with Enhanced Photocurrent Efficiencies Using Oligoaniline-Crosslinked Au/CdS Nanoparticles Arrays on Electrodes. *Advanced Functional Materials* **2008**, 18, (21), 3497-3505.



# CHAPTER EIGHT

---

## 8.1. OVERALL CONCLUSIONS

Novel nano-phase poly(2,5-dimethoxyaniline) and polyaniline with one-dimensional hexagonal morphology were synthesized for the first time in this thesis by using two oxidants( $(\text{NH}_4)_2\text{S}_2\text{O}_8$ , and  $\text{FeCl}_3$ ). These materials were highly crystalline, electroactive and have improved thermal stability, and were used as electron donors in organic solar cells for their one-dimensional morphology. Another novel morphology of polyaniline, the “worm-like” nanostructures was also prepared for the first time in this work, by chemical oxidation of aniline using  $\text{KH}(\text{IO}_3)_2$  as an oxidant. This polyaniline with worm-like morphology was highly conductive and had long fibres which were attractive for solar cells applications.

Zinc oxide with one-dimensional morphology and flower-like morphology were also synthesized and used as electron acceptors for solar cells. It was found that if both acceptor and donor were one-dimensional the solar cell performance was improved, as it was the case with one-dimensional ZnO and PANI with worm-like morphology. When one-dimensional ZnO was used instead of flower-like, the efficiency was improved from  $1.4 \times 10^{-6}$  to 0.16% which is more 100 000 times. It was found that devices performance of PANI-ZnO blends was increased 10 times when PANI-ZnO composites were used, this was due to the reduced recombinations caused by the increased



interface in composites. Poly(2,5-dimethoxyaniline) with hexagonal structures was used as a donor and ZnO with one-dimensional structure as an acceptor and it gave the highest efficiency compared to other morphologies. The reason for the superb performance was attributed to the fact that both ZnO and PDMA are one-dimensional structures and they were also highly crystalline. So, it was concluded that combining one-dimensional morphology with crystallinity can improve the efficiency immensely due to efficient charge transport. Composites of PANI-PPy and PDMA-PPy were also prepared and used as electron donors. It was found that the devices with PDMA-PPy performed better than PANI-PPy due to the high electron harvest as it depicted by UV-Vis. The device preparation for organic solar cells is one of the challenging tasks due to the fragile ITO glass and the fact that the materials are deposited in thin films create problems when connected to contacts because in some cases contacts can go through the sample to glass which can give a straight line. This problem was solved by using the method presented in this thesis where sandwich-like devices were fabricated where the contacts are made on the glass not on the sample.

These one-dimensional polyanilines synthesized in this study can be used as sensor mediators due to their formal potential of 400 mV. Their one-dimensional morphology can enhance significantly the diffusion due to its greater exposure area and penetration depth for gas molecules than the conventional PANI, this can improve the sensitivity of PANI-based sensors. The highly geometric morphology of PDMA hexagonal can also open possibilities of the rods ends or sides being modified with suitable functional groups as it is done with nanotubes. The method presented in this thesis for

hexagonal PDMA synthesis can be used to synthesize co-polymers of polythiophenes and PDMA with one-dimensional and high crystallinity which will enhance its performance since it is one of the best donors. We have also learnt that the composites performs better than blends, hexagonal PDMA can be *in situ* synthesize in the present of C<sub>60</sub> or PCBM to yield a composites with one-dimensional morphology and high crystallinity which will be expected to perform better than blends, as it was observed in this study.

